



**DISTRIBUTION STATEMENT A**  
Approved for public release;  
Distribution Unlimited

Neutron Damage in Distributed Bragg  
Reflectors and Microcavity Lasers

THESIS

Mark A. Suriano  
Captain

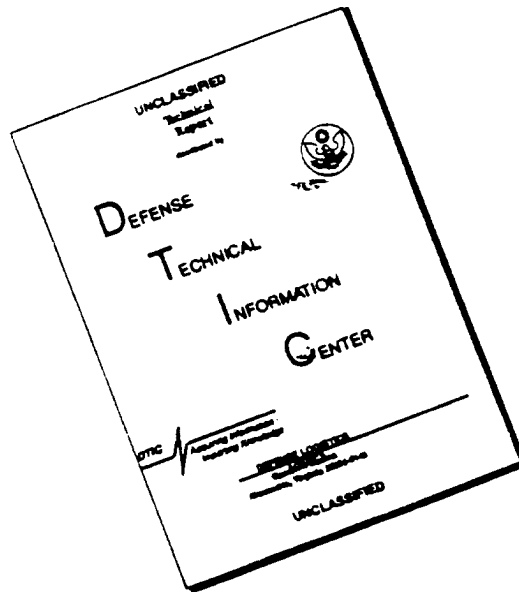
AFIT/GA/ENP/95D-15

DEPARTMENT OF THE AIR FORCE  
AIR UNIVERSITY  
**AIR FORCE INSTITUTE OF TECHNOLOGY**

Wright-Patterson Air Force Base, Ohio

DTIC QUALITY INSPECTED 1

# DISCLAIMER NOTICE



THIS DOCUMENT IS BEST QUALITY AVAILABLE. THE COPY FURNISHED TO DTIC CONTAINED A SIGNIFICANT NUMBER OF PAGES WHICH DO NOT REPRODUCE LEGIBLY.

AFIT/GAP/ENP/95D-15

Neutron Damage in Distributed Bragg  
Reflectors and Microcavity Lasers

THESIS

Mark A. Suriano  
Captain

AFIT/GA/ENP/95D-15

Approved for public release; distribution unlimited

19960315 077

The views expressed in this thesis are those of the author and do not reflect the official policy or position of the Department of Defense of the U.S. Government

**Neutron Damage in Distributed Bragg Reflectors and Microcavity Lasers**

**THESIS**

**Presented to the Faculty of the School of Engineering Physics**

**of the Air Force Institute of Technology**

**Air University**

**In Partial Fulfillment of the**

**Requirements for the Degree of**

**Master of Science in Nuclear Engineering**

**Mark A. Suriano, B.N.E.**

**Captain**

**October, 1995**

**Approved for public release; distribution unlimited**

Neutron Effects on Distributed Bragg Reflectors and Microcavity Lasers

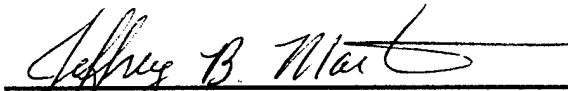
Mark A. Suriano, B.N.E.  
Captain, USAF

Approved:




Paul H. Ostdiek, Lt Col, USAF  
Chairman, Advisory Committee

7 Dec 95



Jeffrey B. Martin, Capt, USAF  
Member, Advisory Committee

22 Nov 95



Jeffrey W. Grantham, Capt, USAF  
Member, Advisory Committee

20 Nov 95



Charles P. Brothers, Jr, Capt, USAF  
Member, Advisory Committee

5 Dec 95

## Preface

The goal of this research was to determine a damage constant for Distributed Bragg Reflectors (DBRs) after being exposed to a neutron fluence. This irradiation study constitutes the first one of its kind in looking at displacement damage to DBRs.

I would like to express sincere thanks to a host of people and organizations that helped in this research. I would like to thank my thesis advisor Lt Col Paul Ostdiek for sparking my interest in radiation effects and helping me whenever I needed a little shove. His background in experimental research proved to be a valuable tool that I was able to draw from. Thanks to Capt Grantham for the use of his Optics laboratory. Maj Richard Bagnell and Maj Greg Vansuch, you provided countless hours of insightful tips, as well as helped me whenever I needed to change equipment around saving countless hours.

Thanks to Capt Charlie Brothers at PL/VTE for sponsoring the project, and allowed me to explore a new and interesting field within the nuclear community. Capt Jim Lott and Dr Kevin Malloy provided the samples that actually allowed the project to proceed. Thanks to the Department of Energy for their Reactor Sharing Program, through which use of the Ohio State's Research Reactor (OSURR) was possible. The staff at OSURR were exceptional to work with, and I am indebted to all of the time and effort that they put forth to irradiate my samples. Especially Dr Joe Talnagi and Kevin Herminghuysen, thanks.

Finally, I would like to express my deepest appreciation to my wife Briar, who provided love and support to help me carry out this effort. She kept me sane along with the support of my parents Ronald and Marilyn Suriano. Thanks.

Mark A. Suriano

## Table of Contents

	Page
Preface . . . . .	iii
Table of Contents . . . . .	iv
List of Figures . . . . .	vi
List of Tables . . . . .	ix
Abstract . . . . .	x
I. Introduction . . . . .	1-1
1.1 Background . . . . .	1-3
1.1.1. Nature of Radiation Effects . . . . .	1-3
1.1.2. Damage Constant . . . . .	1-8
1.1.3. Distributed Bragg Reflectors (DBR) . . . . .	1-11
1.2 Goal . . . . .	1-13
1.3 Scope . . . . .	1-14
1.4 Approach/Methodology . . . . .	1-15
1.5 Sequence of Presentation . . . . .	1-15
II. Theory . . . . .	2-1
2.1 Distributed Bragg Reflectors . . . . .	2-1
2.2 Band Theory . . . . .	2-5
2.3 Displacement Damage . . . . .	2-7
2.4 Messenger-Spratt Equation . . . . .	2-11



	Page
2.5 Annealing .....	2-14
III. Experimental Procedures .....	3-1
3.1 Sample Growth .....	3-1
3.2 Laboratory Configuration .....	3-4
3.3 Test Matrix .....	3-10
3.4 Ohio State University's 500 kW Research Reactor .....	3-13
3.5 Dosimetry .....	3-16
IV. Data and Analysis .....	4-1
4.1 Theoretical Change in Reflectance .....	4-1
4.2 Relative Reflectivity Response .....	4-5
4.3 Absolute Reflectivity Response .....	4-10
4.4 Damage Constants .....	4-13
4.5 Electrically Pumped VCSELs .....	4-20
V. Conclusions .....	5-1
Bibliography .....	BIB-1
Appendix A: Mathcad Program to Estimate Activity of Irradiated Samples ...	A-1
Appendix B: Wafer Diagrams for Reflectivity Study .....	B-1
Appendix C: Equipment List .....	C-1
Appendix D: Radioactive Material Handling Procedure .....	D-1
Appendix E: Mathcad Program to Determine the Reflectivity Damage Constant .....	E-1
Vita .....	VITA-1

## List of Figures

Figure	Page
1.1. Displacement Damage Kinetics of Frenkel Defects from an Initial Neutron Interaction with a Semiconductor Lattice . . . . .	1-5
1.2. Monte Carlo Result of PKA Tracks Through a Material . . . . .	1-7
1.3 Knee Curve Illustrating Messenger-Spratt Type of Equation . . . . .	1-9
1.4 Damage Constants Ratio for Protons, Electrons, and Gamma Rays Versus Nonionizing Energy Deposition . . . . .	1-11
1.5 DBR Reflection and Transmission for Incident Light . . . . .	1-12
1.6 Relative Reflectance Spectrum of a DBR mirror from 530-880 nm Using a Quartz Halogen Lamp, and a Silver Near Infrared Reference Mirror . . . . .	1-12
1.7 Microcavity Formed Through Placement of the Photonic Devices Between two DBRs . . . . .	1-13
2.1 Band Structure of a Semiconductor with no Impurities within the Bandgap Region. . . . .	2-6
2.2 Band Structure of a Semiconductor with Impurities within the Bandgap Region. . . . .	2-7
3.1 Growth of the DBR VCSEL: XC0911a. . . . .	3-2
3.2 Growth of the DBR Mirror: XC1118b. . . . .	3-3
3.3 Growth of the Electrical Pumped VCSELs: E319 . . . . .	3-4
3.4 Line Diagram of the Relative Reflectance Measurement Set-up. . . . .	3-5
3.5 Line Diagram of the Absolute Measurement Platform Equipment Configuration . . . . .	3-7
3.6 Line Diagram of the Electrical Pumping Platform Equipment Configuration . . . . .	3-9
3.7 Ohio State University's 500 kW Research Reactor - Top Down diagram, courtesy OSURR. . . . .	3-14

Figure	Page
3.8 Reactor Plug for Ohio State University's Research Reactor . . . . .	3-15
3.9 Representative Differential Flux at 400 kW in Beam Port 1 . . . . .	3-17
4.1 Theoretical Spectral Response by Varying the Extinction Coefficient Through adding a Constant over the Complete Wavelength Range . . . . .	4-3
4.2 Theoretical Spectral Response by Varying the Extinction Coefficient Through adding a Constant over the Segment of the Wavelength Range . . . . .	4-4
4.3 Theoretical Spectral Response with Varying Absorption Coefficients . . . . .	4-5
4.4 Initial Relative Reflectance After a 72,000 kW-min Irradiation . . . . .	4-6
4.5 Control Sample Reflectance After a 75 min Bake at 120 °C . . . . .	4-8
4.6 Relative Reflectance 72,000 kW-min with Apparent Spectral Distortion with the Wrong Background Correction is Made. . . . .	4-9
4.7 Relative Reflectance Measure for a 1500 kW-min Irradiation After White Equipment Repairs and Re-optimization . . . . .	4-10
4.8 Absolute Reflectance Measurement. . . . .	4-11
4.9 Absolute Reflectance Measurement Locations Overlaid onto a Relative Reflectance Spectrum . . . . .	4-12
4.10 Absolute Reflectance Measurements for a 25 kW-min Irradiation of a DBR VCSEL . . . . .	4-13
4.11 Determination of the Damage Constant for XC0911a, VCSEL Structure, by Minimizing the Sum of the Squares . . . . .	4-15
4.12 Messenger-Spratt Relationship for the VCSEL Reflectance. . . . .	4-15
4.13 Determination of the Damage Constant for XC1118b, DBR Mirror, by Minimizing the Sum of the Squares . . . . .	4-16
4.14 Messenger-Spratt Relationship for the DBR Mirror Reflectance. . . . .	4-16
4.15 Linear Relationship Between Equivalent Damage for Neutrons, Protons, and Electrons. . . . .	4-20

Figure	Page
4.16 Subthreshold L-I data for 50 $\mu\text{m}$ Aperture Electrically Pumped VCSELs.....	4-20

## List of Tables

Table	Page
3.1 Irradiation Set Component Breakdown . . . . .	3-10
3.2 History of the Irradiation Sample Sets . . . . .	3-11
4.1 VCSEL and DBR Mirror Damage Constants over the Spectral Range . . . . .	4-18
4.2 Damage Constants for Bipolar Transistors and GaAs Laser Diodes . . . . .	4-19

Abstract

Distributed Bragg Reflectors (DBRs) grown on a gallium-arsenide substrate for a solid state mirror and a vertical cavity surface emitting laser (VCSEL) were subjected to a neutron fluence to determine the sensitivity of the DBRs. The samples were irradiated at Ohio State University's 500 kW research reactor. Relative and absolute reflectance measurements were taken before and after each irradiation over a spectral band of 530-880 nm. Relative reflectance measurements showed that the irradiation did not cause any spectral shift over seven decades of neutron fluences. The reflectivity of the DBRs decreased from their initial measurements after being irradiated. The reflectance decrease was correlated to the incident neutron fluence to determine a Messenger-Spratt type of equation to predict the DBRs response. A radiation damage constant for the VCSEL and DBR mirror were determined to be  $3.83 \times 10^{13}$  [neutrons/cm<sup>2</sup>] and  $2.19 \times 10^{13}$  [neutrons/cm<sup>2</sup>] respectively utilizing a 1 MeV equivalent (Si) neutron fluence.

# Neutron Damage in Distributed Bragg Reflectors and Microcavity Lasers

## I. Introduction

This thesis investigates the effects of neutron irradiation on semiconductor Distributed Bragg Reflectors (DBR) and some of the solid state devices that use them. The use of these mirrors to form microcavity devices has become wide spread. When fully fielded, these miniature devices will be placed in environments where interactions from ionizing and non-ionizing radiation occur. Understanding their response to particle interactions enable predictions of the expected degradation in performance as well as allow for improving current designs. A radiation study of DBRs is a logical first step since they are a key technology employed in these microcavity devices. In order to understand the reason for a study of this nature a brief overview of DBRs follows, along with the environmental concerns necessitating this study. As a result of the potentially harsh environment of ionizing and non-ionizing particles, an overview of radiation effects on materials is presented. Following at the end of the chapter are the goals and scope of the thesis.

DBRs consist of a periodic structure of high and low index of refraction material deposited onto a surface forming a quarter wave stack. Incident light at the interface of each layer produces a transmitted and reflected component that constructively interferes at a design wavelength ( $\lambda_0$ ). The overall transmittance and reflectance are governed through the selection of the high and low index material as well as the number of period pairs. Microcavity devices use the DBR period pairs to bound the cavity, forming an effective

Fabry-Perot interferometer. When an interferometer employs mirrors with a fixed separation distance, the structure becomes an etalon. This etalon will only support longitudinal modes that are integer multiples of half of the design wavelength:  $m\lambda_0/2$ ,  $m \in [1, 2, 3, \dots]$ . DBR mirror pairs form an etalon providing for enhanced efficiency and sensitivity over a frequency range.

Solid state devices with DBRs are becoming an industry standard as miniaturization of photonic devices continues. It is reasonable therefore to expect these devices to find their way into military hardware both in space and on the battlefield. A concept of counterproliferation of nuclear weapons, current policy developed by the DoD, demands that US force employment not be curtailed by renegade nuclear threats. If this policy fails to keep nuclear weapons out of the hands of potential proliferators then a new threat is levied upon the DoD. Therefore the battlefield must be considered a nuclear battlefield. Both environments have unique radiation hazards that effect the operability of these devices. They are full of highly energetic ionized and non-ionized particles that will interact with anything in their path. Space environments place devices in contact with galactic cosmic rays, protons, electrons, X-rays, gamma rays, neutrons, and heavy ions all with energies spanning over ten decades (eV-GeV). Neglecting the blast and thermal effects, a nuclear battlefield is composed of the same type of radiation particles except for the galactic cosmic rays. However, neutrons are much more prominent on the nuclear battle field than in space.

Devices will experience both ionization and displacement damage in space and nuclear environments. Due to the nature of the DBR structure, they should be immune to



the ionizing effects of radiation while prone to displacement damage by high energy neutrons, electrons, protons, and ions. Ionization damage can change latent traps between the band structure into active traps as well as creating electron-hole pairs that do not effect the passive operation of the DBR as a quarter-wave stack. Displacement damage in the DBR creates trapping and recombination centers within the band structure of the material adding parasitic losses. Before going into these topics, a more in-depth review of radiation effects and DBRs is warranted.

## **1.1 Background**

To understand the effects of radiation upon any device, the basic interaction mechanisms need to be understood. When dealing with radiation effects some essential questions must be asked: “What are particles of interest?” “How is the damage manifested?” “Will these effects anneal, or are they permanent?” These questions come from understanding the environment that the device will see, as well as knowing how the device operates and how it was made.

**1.1.1 Nature of Radiation Effects.** When an energetic particle interacts with a solid both ionizing and non-ionizing effects are sustained. These effects can either be transient or permanent. Ionizing damage results primarily from charged particle interactions; whereas, non-ionizing effects result fundamentally from neutral particle collisions. If a charged particle has sufficient energy it can produce ionizing (predominate mechanism) and non-ionizing effects. Neutral particles with enough energy to free a charged particle from the lattice can also produce ionization effects in addition to its primary non-ionizing mechanism. The nature of the overall damage to a material is

directly related to the particle composition and energy dependence of the incident particle flux.

An ionizing particle transfers part of its kinetic energy to the surrounding lattice as it slows down, and produces changes in the bulk material properties. One of the bulk material parameters that change is the conductivity. Conductivity of the material increases due to the production of excess charge carriers (electron-hole pair creation), trapped charges (in insulated regions), or through disturbances the electric and magnetic fields of the material [4]. If the incident particle is energetic enough to overcome the Coulombic force, it can also displace the stationary lattice atom to cause further damage. Ionization damage is significant with devices that rely on majority and/or minority carriers to operate.

All devices are subject to non-ionizing damage, or displacement damage, which results from neutral or highly energetic charged particle interactions. Whenever displacement damage is discussed, the main focus is on damage as a result of neutral particle interactions. Neutrons interact by way of the nuclear force causing either elastic or in-elastic collisions. There is no effect from Coulombic force interactions due to the charge neutrality of the neutrons. A collision might displace the atom from its lattice site causing a vacancy, and move the atom to take up a new position with the crystal. This occurs when the neutron imparts part of its kinetic energy to the atom that is equal to or above the energy binding it to the lattice. The mean energy needed to displace an atom from the lattice ( $E_d$ ) is approximately 20-25 eV for silicon and 7-11 eV for gallium-arsenide [4].

A primary knock-on atom (PKA) or interstitial atom results when a stationary atom is displaced from its equilibrium lattice position (Figure 1.1). The resulting interstitial-vacancy pairs (Frenkel defects) cause a distortion of the local lattice structure. There is a potential for the PKA to cause further displacements if the kinetic energy of the PKA exceeds the mean displacement energy ( $E_d$ ) of a lattice site by a factor of two or more. Along the PKA's particle track there will be displacement damage until its kinetic energy is less than or equal to  $2E_d$ .

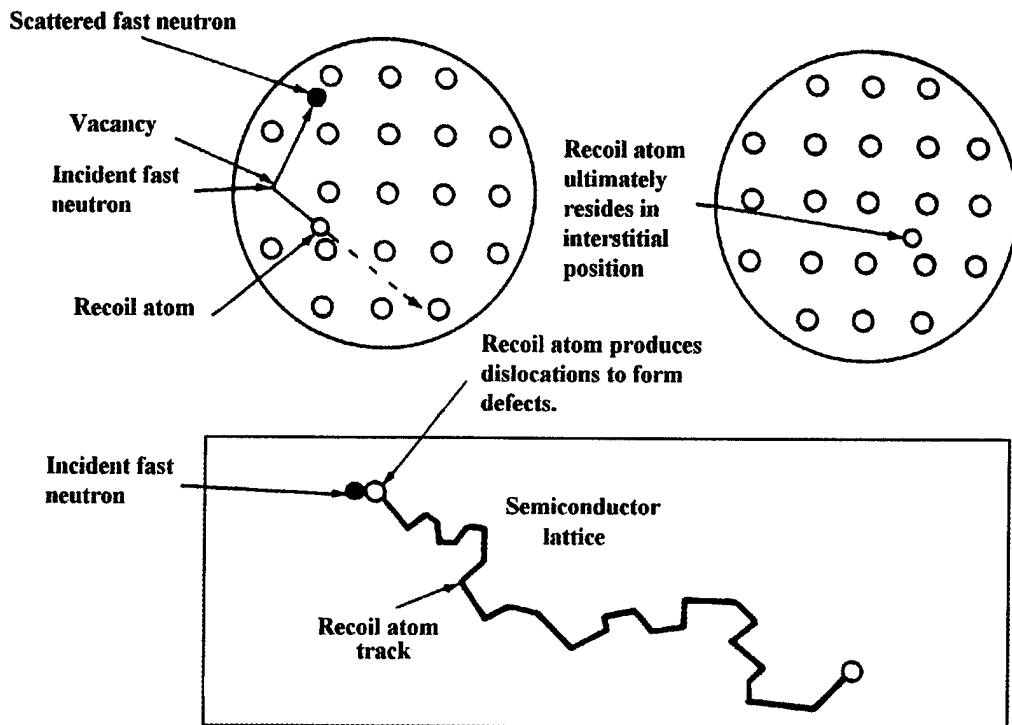


Figure 1.1: Displacement Damage Kinetics of Frenkel Defects from an Initial Neutron Interaction with a Semiconductor Lattice [4].

The incident particle as well as the PKA can cause ionization damage through secondary interactions. The resulting neutron induced ionization manifests itself in three different ways. The initial neutron can produce PKA or ions that can in turn produce ionization through the material. Next, neutrons colliding with lattice atoms inelastically leave the atom in an excited state where it will decay by gamma emission (an  $(n,\gamma)$  reaction). The final process is through neutron absorption. The absorption reaction can be either a transmutation or a fission event. Transmutation changes the initial atom into an isotope with one more neutron. Depending on the stability of that isotope it might decay by alpha ( $\alpha$ ), beta ( $\beta^\pm$ ), or neutron emission. Each of which can produce ionization within the material. If the atom is fissionable, then the atom will split into heavy fission fragments that will decay, neutrons, and gamma. Again all will contribute to the secondary ionization. Due to charged particle reactions, damage is localized near the creation of the secondary particles. Damage clusters or spikes appear at the end of the PKA tracks where a majority of the ionization takes place [4] (Figure 1.2). The majority of the damage in the cluster is from the residual kinetic energy of the PKA after it is less than or equal to  $2E_d$ . Still ionization damage is found throughout the particle track.

The overall effect of displacement damage for electrical devices is the formation of recombination and trapping centers in the forbidden band gap between the conduction and valance bands. Frenkel defects may combine with impurity or dopant atoms to produce stable defects, or they can stand on their own forming defect complexes. These trapping and recombination sites are directly responsible for reducing minority carrier lifetime. Passive devices, like DBRs, experience the same damage due to recombination and

trapping centers. Instead of a minority carrier lifetime of active devices, the DBR loss mechanism is due to the new trapping and recombination sites within the lattice. Incoming photons are now absorbed by these traps or scattered from Frenkel defects making the structure more lossy.

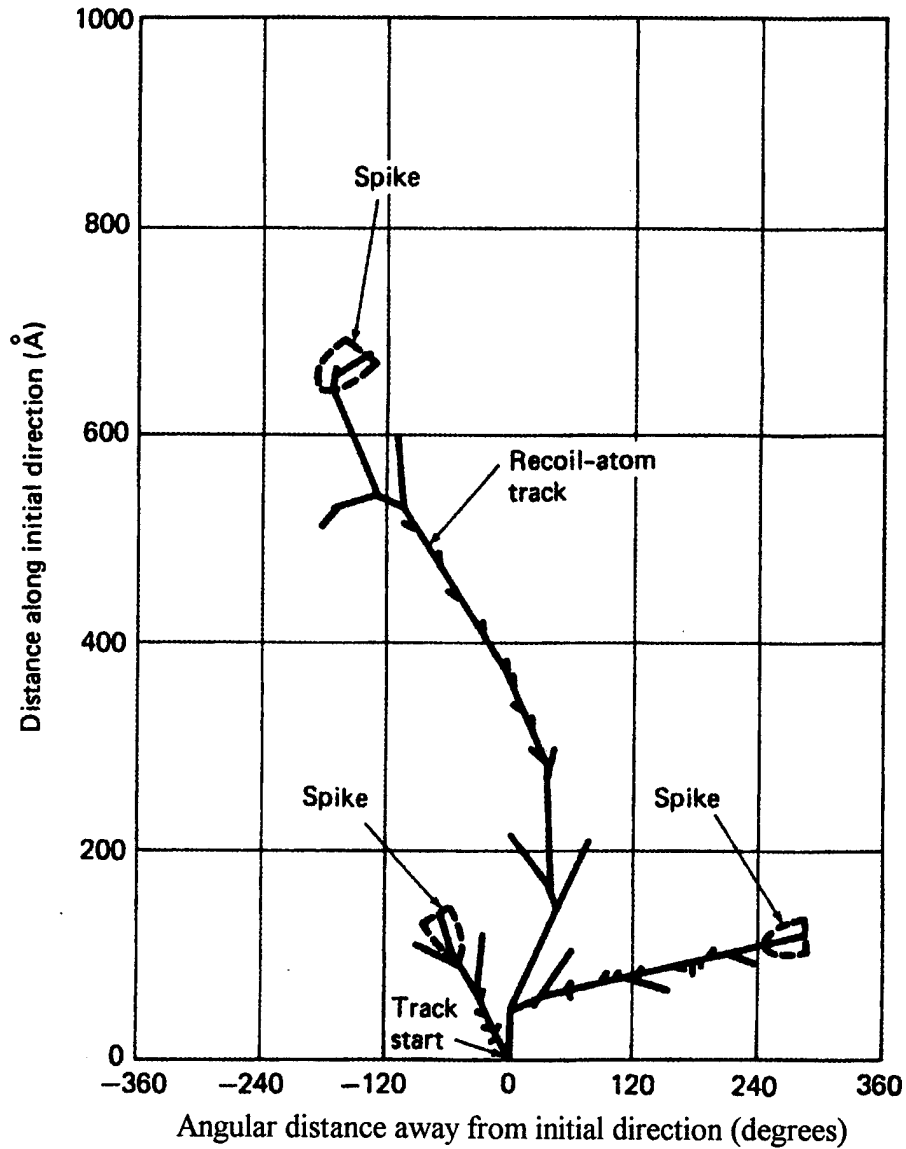


Figure 1.2: Monte Carlo Result of PKA Tracks Through a Material [4]

The neutron damage can be temporary or permanent after an irradiation. Some defects from neutron damage can anneal over time, thereby reducing the total amount of damage to the structure. There are two types of annealing: isothermal and isochronal. Isothermal annealing takes place over a period of time at a given temperature (normally room temperature). Isochronal annealing elevates the temperature of the sample to accelerate the damage removal that would have been removed at a lower temperature albeit a longer time span. The effects of isothermal and isochronal annealing are of interest to this irradiation study only to determine if an identified defect is transient or not.

**1.1.2 Damage Constant.** The overall effect of radiation on a sample is determined through characterizing specific parameters initially and after an irradiation to find a difference. This process is carried out using a range of particle fluences to determine an effective damage constant, K. The damage constant is determined from the line after plotting the parameter as a function of fluence. These characteristic “knee” curves, as in Figure 1.3, show the parameter degradation (relative resistivity) as a function of neutron fluence. The damage constant is determined from the slope of the linear region after the parameter transitions from the nominal value. From the experimentally calculated damage constant, a relationship can be written through a Messenger-Spratt type of equation:

$$\text{Parameter}(\Phi) = \text{Parameter}_{\text{initial}} + \Phi K$$

Here the device parameter varies proportionally with the fluence.

The damage constant is based on a fluence of a mono-energetic particles. It is not easy to get a high fluence of mono-energetic particles, but one can determine it from a bombarding particle flux with a known broad band spectrum. The equivalent mono-

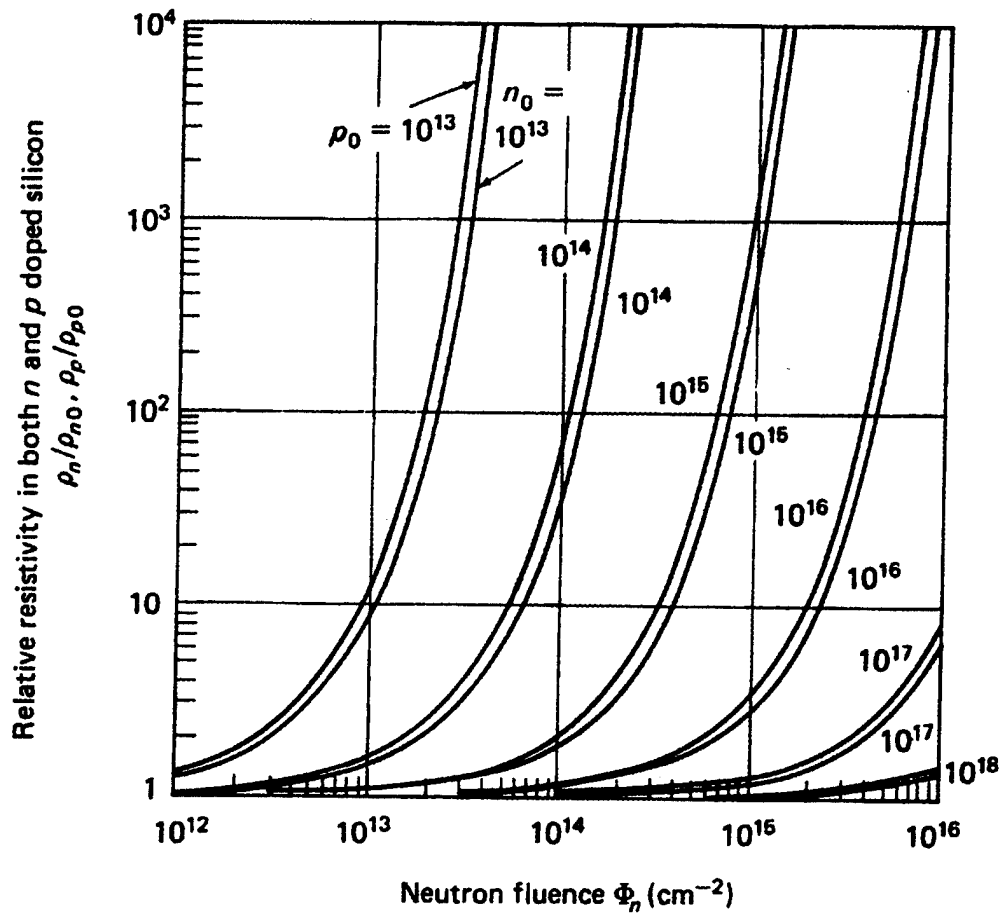


Figure 1.3: Knee Curve Illustrating Messenger-Spratt Type of Equation [4]

energetic fluence is calculated from the displacement damage of a given material at a given energy. A mono-energetic fluence allows for repeatability of experiments as well as comparability of results due to the variance in the energy between different particle sources. Within the radiation effects community the damage is usually reported as a 1 MeV equivalent fluence to silicon or gallium arsenide [17].

The damage from one type of mono-energetic particle can be correlated to produce an estimation of the damage expected from other types of particles. This

correlation is accomplished through calculation of a particle's Nonionizing Energy Loss (NIEL), and is analogous to a linear energy transfer that one sees in ionizing effects.

While it is not economically feasible to test every device against every particle that it might encounter in its operating environment, it is possible to use NIEL of a singular particle to determine a damage constant, and then predict new damage constants for other particles [20]. The damage constant is plotted as a point on a graph with an extrapolated line with a 1 decade per decade slope on a log-log graph to predict all other particles. The ratio of the damage constant for protons, electrons, and  $^{60}\text{Co}$  to that of 1 MeV equivalent (Si) fission neutrons are plotted versus the calculated NIEL in Figure 1.4. The linear dependence between electrons, protons, neutrons, and gamma rays from the  $^{60}\text{Co}$  is readily apparent from the figure. This thesis attempts to experimentally determine a damage constant and NIEL graph for the solid state DBR structures investigated.



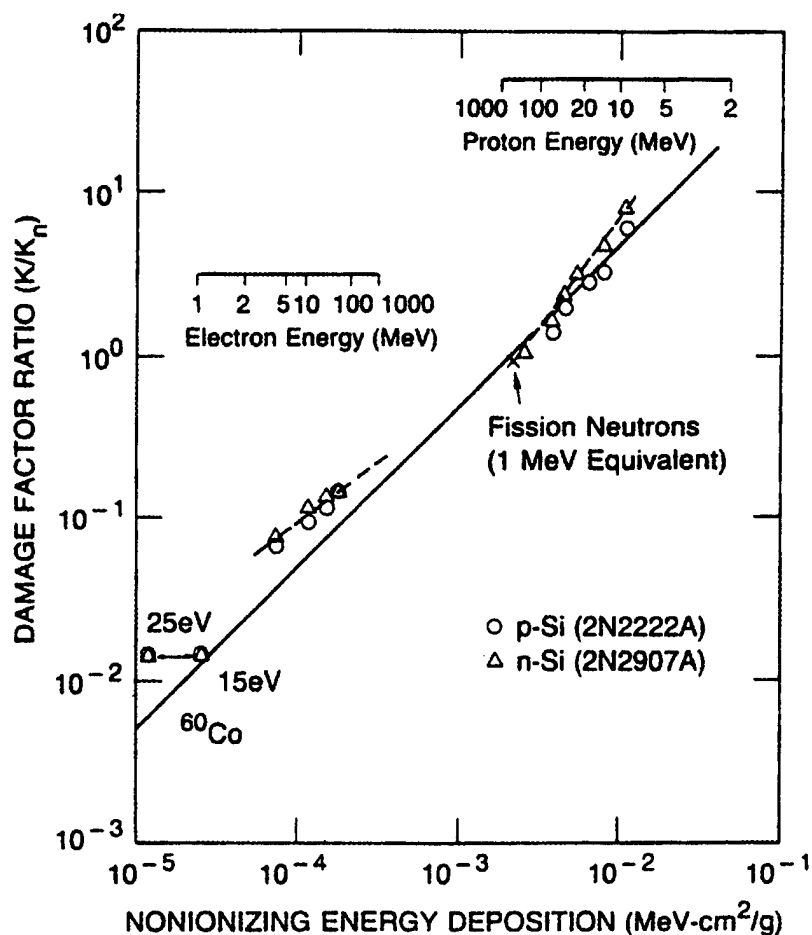


Figure 1.4: Damage Constants Ratio for Protons, Electrons and Gamma Rays Versus Nonionizing Energy Deposition. Note: Log-Log Scale [29]

**1.1.3 Distributed Bragg Reflectors (DBR).** The ability to deposit precise multi-layer films on a substrate have increased over the years allowing for the success of DBR mirrors and microcavities [23]. Epitaxial layers of alternating high and low index of refraction material produce the DBRs. Figure 1.5 illustrates how a DBR works. Incident light upon the first layer is both reflected and transmitted. Only light that has close to the designed wavelength ( $\lambda_0$ ) will be reflected at a maximum. All other wavelengths will suffer losses due to the destructive and constructive interference. Figure 1.6 illustrates the reflectance

of the DBR mirror used in the irradiation study. The high reflectance region from 660-680 nm can be seen along with the decreasing side bands.

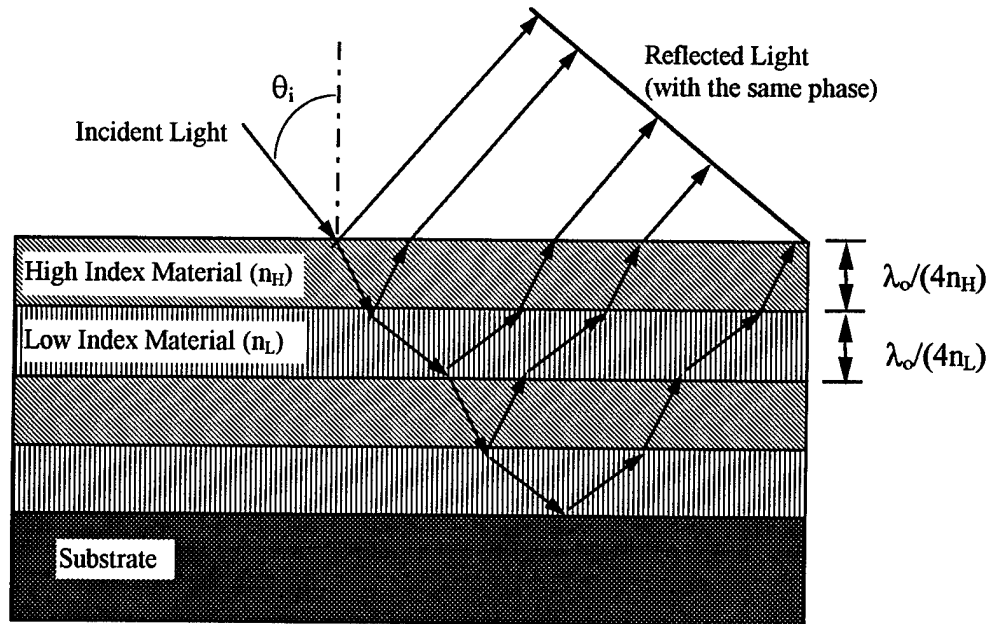


Figure 1.5: DBR Reflection and Transmission for Incident Light

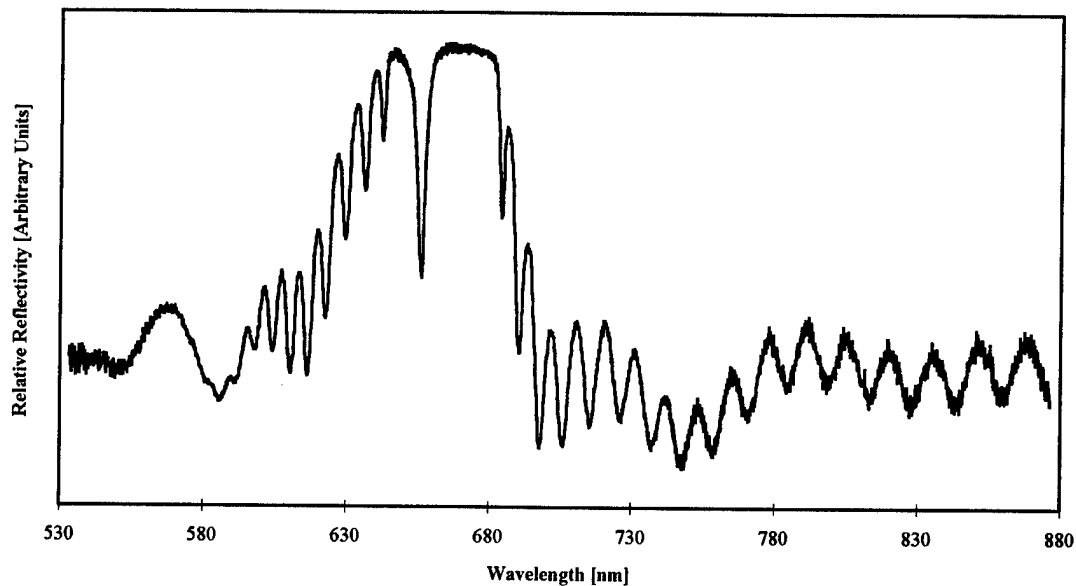


Figure 1.6: Relative Reflectance Spectrum of a DBR Mirror from 530-880 nm Using a Quartz Halogen Lamp and a Silver Near Infrared Reference Mirror.

When DBRs are employed with a microcavity, a Fabry-Perot etalon is created (Figure 1.7). This etalon confines the electromagnetic modes within the cavity as well as increasing the device sensitivity and spectral response. The DBR-etalon pair create a resonant cavity allowing only wavelengths that match the spacing of the etalon:  $d = m\lambda/2$ ,  $m \in [1, 2, 3, \dots]$ . When coupled together the pair yields a single mode device (longitudinal mode), and allows a device designer to tailor the DBR-etalon for a specific purpose.

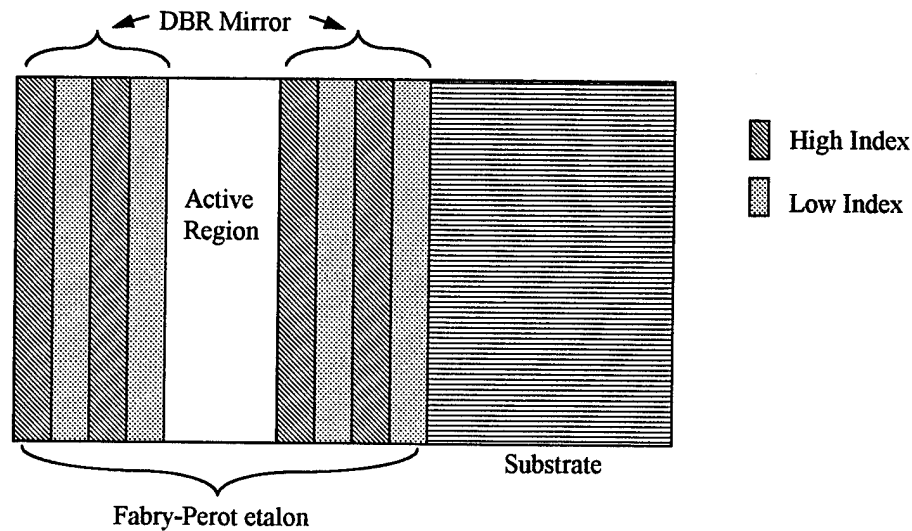


Figure 1.7: Microcavity Formed Through Placement of the Photonic Devices Between two DBRs

## 1.2 Goal

This thesis examines the effect that neutron irradiation has upon DBRs. The main goal is to determine a damage constant for a reflectivity at a 1 MeV equivalent fluence (Si), allowing correlation with other particle types. A secondary goal is to gather information about the damage mechanisms that degrade the mirror's performance.

### 1.3 Scope

The scope of the effort was to determine a Messenger-Spratt damage constant for the reflectivity. A damage constant from neutrons will allow for an equivalent damage constant for protons, electrons, and ions through NIEL. The DBR study utilized an unprocessed vertical cavity surface emitting laser (VCSEL) and a DBR mirror, both grown on GaAs substrates. The primary goal focuses on the ability to couple the resulting neutron damage to the structure's index of refraction through the change in reflectivity. A secondary focus was determining the effect of neutron irradiation upon an additional set of electrically pumped VCSELs also grown from GaAs. A damage constant was attempted for the lasing slope efficiency, lasing current threshold, and spectral response of the excited light (FWHM and  $\Delta\lambda$ ). The electrically pumped VCSEL study covered the same neutron fluence range as the reflectivity study.

The effects of annealing could not be addressed specifically. When the samples were irradiated at Ohio State they could not be cryogenically cooled to freeze the damage within the lattice immediately after the fluence was stopped. As a result, all of the samples tested after irradiation had already experienced annealing. Post irradiation data was obtained only after a decay time, based on the neutron activation, reducing the sample's radioactivity. The time lag introduced uncertainties for a true annealing study (minimum of 1 day and an average of three days). A limited attempt to study isochronal annealing was performed on some of the samples to determine if there was any variation in the post irradiation behavior. This study determined if the samples had fully annealed or if they were still annealing.

#### **1.4 Approach/Methodology**

The unprocessed VCSEL and DBR samples were cleaved from a one inch wafer for the study (Appendix A). These samples were characterized for their broad band reflectance ranging from 530-880 nm. The data was collected by an optical multi-channel analyzer from a white light filament. These relative reflectance measurements were checked with an absolute reflectance measurement from a Ti-sapphire laser. Each of these measurements were performed before and after irradiation. The slope efficiency, current threshold, and spectral data on the electrically pumped VCSELs were obtained before and after irradiation as well. A few samples were tested to determine if the samples were still annealing through isochronal methods.

All of the neutron irradiation was performed at the Ohio State University's 500 kW research reactor. The samples were covered with a cadmium foil to cut off neutrons of energy below 150 eV, reducing thermal activation of the material. The total damage study covered a range of  $10^{10}$ - $10^{17}$  neutrons/cm<sup>2</sup> of 1 MeV equivalent Si fluence.

#### **1.5 Sequence of Presentation**

Chapter II will cover the theory behind the optical properties of materials as well as consequences of placing substances in contact with a neutron beam. All of the equipment and experimental procedures are covered in Chapter III. The details of the data obtained through the course of the thesis work will be examined in Chapter IV. Chapter V summarizes the work and presents recommendations.

## II. Theory

In order to discuss the damage caused to DBRs as a result of neutron irradiation a basic foundation needs to be understood. This chapter contains the physics associated with DBRs along with the damage created through particle interactions. Presented is a development of the mechanisms behind damage displacement along with a set of equations to predict changes in the refractive index. Described at the end of the chapter are the effects of annealing of radiation damage.

### 2.1 Distributed Bragg Reflectors

The DBRs consist of alternating high and low index of refraction material that form a quarter wave stack. Alternating layers are deposited in a fashion such that their thickness times the real part of the index of refraction equals one fourth the design wavelength:

$$l_H n_H = l_L n_L = \lambda_0 / 4 \quad (2.1)$$

where:

- $l_H$ : thickness of high index layer
- $n_H$ : index of refraction for the high index layer
- $l_L$ : thickness of the low index layer
- $n_L$ : index of refraction for the low index layer
- $\lambda_0$ : design wavelength

The subscripts H and L refer to the high and low index of the stack material respectively.

Incident light normal to the surface constructively interferes off all of the subsequent layers to produce a peak in reflectivity at the designed wavelength. Constructive

interference implies that light reflected from the layers differ in phase by integer multiples of  $2\pi$ .

Consider electro-magnetic waves traveling within a multilayer medium composed of N layers. Waves traveling through a given layer in the material will be a superposition of all of the incident and reflected waves within that layer. The electric and magnetic fields for the  $m^{\text{th}}$  layer are obtained from boundary conditions requiring continuity of the fields across layers (a full derivation is presented in *OPTICS* by Hecht [2]). Both the electric and magnetic fields are dependent upon the fields of the  $m+1$  layer and the dielectric properties of the  $m^{\text{th}}$  layer.

$$\begin{aligned} E_m &= E_{m+1} \cos(k_o h) + H_{m+1} \frac{i \sin(k_o h)}{Y_m} \\ H_m &= E_{m+1} Y_m i \sin(k_o h) + H_{m+1} \cos(k_o h) \end{aligned} \quad (2.2)$$

where:

$E_m$ : electric field layer in the  $m^{\text{th}}$  layer  
 $H_m$ : magnetic field layer in the  $m^{\text{th}}$  layer  
 $k_o = 2\pi / \lambda_o$ : propagation number  
 $h \equiv n_m d_m \cos(\theta_m)$   
 $d_m$ : thickness of the  $m^{\text{th}}$  layer  
 $\theta_m$ : angle of incidence in the  $m^{\text{th}}$  layer  
 $n_m$ : index of refraction in the  $m^{\text{th}}$  layer  
 $\delta_m = k_o h$ : phase of the field in the  $m^{\text{th}}$  layer  
 $Y_m$ : optical admittance of the  $m^{\text{th}}$  layer

$$Y_m = \sqrt{\frac{\epsilon_m}{\mu_m} \frac{n_m}{\cos(\theta_{m+1})}}$$

$\epsilon_m$ : dielectric constant in the  $m^{\text{th}}$  layer  
 $\mu_m$ : permeability of the  $m^{\text{th}}$  layer

The representation of the electric and magnetic fields in equation 2.2 provides an efficient way of linearizing the problem for a N layer stack. Equation 2.2 is now represented as a matrix of the electric and magnetic fields from the m and m+1 layers [2].

$$\begin{bmatrix} E_m \\ H_m \end{bmatrix} = \begin{bmatrix} \cos(k_o h) & \frac{i \sin(k_o h)}{Y_m} \\ Y_m i \sin(k_o h) & \cos(k_o h) \end{bmatrix} \begin{bmatrix} E_{m+1} \\ H_{m+1} \end{bmatrix} \quad (2.3)$$

Given that the multi-layer stack is composed of N layers, it is readily apparent that the solution can be represented as a power series.

$$\begin{bmatrix} E_m \\ H_m \end{bmatrix} = \prod_{m=1}^N M_m \begin{bmatrix} E_{m+1} \\ H_{m+1} \end{bmatrix} \quad (2.4)$$

where:

$$M_m = \begin{bmatrix} \cos(k_o h) & \frac{i \sin(k_o h)}{Y_m} \\ Y_m i \sin(k_o h) & \cos(k_o h) \end{bmatrix}$$

DBR structures are designed so that the distance between layers is  $\lambda_o/4$ , which reduces the phase change between propagating waves to  $\delta_m = \pi/2$  at normal incidence.

The characteristic matrix  $M_m$  reduces to:

$$M_m = \begin{bmatrix} 0 & \frac{i}{Y_m} \\ iY_m & 0 \end{bmatrix} \quad (2.5)$$

Assuming that we have light normally incident to the surface of an N layer stack, then the power series solution of equation 2.4 will change due to equation 2.5. The electric and magnetic fields entering the stack (subscript 0) are dependent upon the



material properties of the layered stack and substrate (subscripts of  $m$  and  $sub$  respectively). The new power series relation is:

$$\begin{bmatrix} E_0 \\ H_0 \end{bmatrix} = \prod_{m=1}^{N+sub} M_m \begin{bmatrix} E_{sub} \\ H_{sub} \end{bmatrix} = \prod_{m=1}^{N+sub} \begin{bmatrix} 0 & \frac{i}{Y_m} \\ iY_m & 0 \end{bmatrix} \begin{bmatrix} 1 \\ Y_{sub} \end{bmatrix} E_{sub} \quad (2.6)$$

The solution of the electro-magnetic fields outside the layered stack allows for a calculation of the stack's reflectance. The reflectivity is based on the optical admittance of the incident medium ( $Y_0$ ) and the assembly admittance ( $Y = H_0/E_0$ ) [23,30]:

$$\mathfrak{R} = \frac{\left| \frac{Y_0 E_0 - H_0}{Y_0 E_0 + H_0} \right|^2}{\left| \frac{Y_0 - \frac{H_0}{E_0}}{Y_0 + \frac{H_0}{E_0}} \right|^2} = \frac{\left| \frac{Y_0 - Y}{Y_0 + Y} \right|^2}{\left| \frac{Y_0 - Y}{Y_0 + Y} \right|^2} \quad (2.7)$$

Equation 2.7 is generalized for any  $N$  layered stack; although, the stack optical admittance,  $Y$ , is dependent upon the number of layers. There is a slightly different form of the optical admittance if, for a  $N$  layered stack,  $N$  is either even or odd.

$$Y = \begin{cases} \frac{Y_1^2 Y_3^2 \dots Y_N^2}{Y_2^2 Y_4^2 \dots Y_{sub}^2}, N - odd \\ \frac{Y_1^2 Y_3^2 \dots Y_{N-1}^2 Y_{sub}^2}{Y_2^2 Y_4^2 \dots Y_N^2}, N - even \end{cases} \quad (2.8)$$

Once the stack admittance is calculated, the reflectivity of the structure is easily determined from equation 2.8. The structure should be maximized as close to one as possible for the design wavelength  $\lambda_0$ . The ultimate reflectance in a stack will be limited due to the losses from absorption and scattering [30]. Scattering losses are principally due to defects within the layers, where absorption is a result of material properties.

Materials for a stack should be chosen to maximize the high reflection region while not adding inherent loss mechanisms.

A material's index of refraction is actually a complex number. The absorption of light through the material is governed by the imaginary component of the index of refraction which is frequency dependent. Absorption is significant when photons incident on the DBR have energy greater than the bandgap energy [24]. As a result the change in phase of the electro-magnetic fields between layers must be represented by the complex index of refraction:  $n_m = n - i\kappa$ . Thus the new phase change is dependent upon an absorptive term as well as the real refractive index. The material's index of refraction will change upon suffering displacement damage from neutrons. Trapping and recombination centers formed as a result of neutron interactions will increase the refractive index's absorptive term. Therefore losses within the DBR structure will be due to the incident neutron fluence.

## **2.2 Band Theory**

Semiconductors are characterized by a finite energy gap between the valence and conduction bands. Valence bands are lower energy states that are nearly or completely filled with electrons. Conduction bands are higher energy states that are sparsely populated with or void of electrons. A forbidden energy band separates the conduction band from the valence band. This forbidden region is devoid of any energy states given no impurities in the material. Semiconductor action results in the interaction of the valence and conduction bands. For an electron to move from the valence band to the conduction band it needs at least the energy separating the valence and conduction bands

Where  $E_{\text{gap}} = E_C - E_V$ . Electrons with energy less than the bandgap energies are not able to transition from the valance to conduction band.

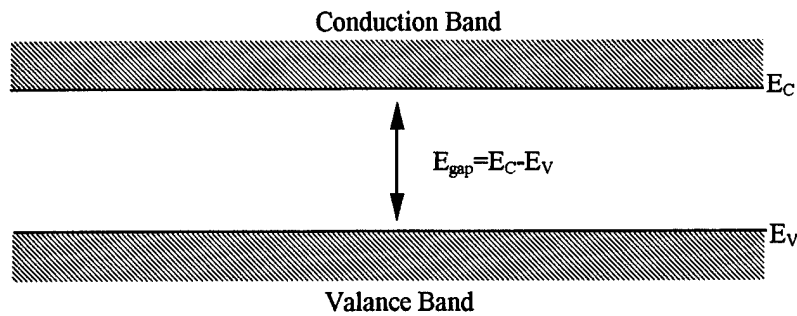


Figure 2.1. Band Structure of a Semiconductor with no Impurities within the Bandgap Region.

When impurities exist in a semiconductor, they can produce energy levels within the forbidden gap region. These impurity sites allow for recombination and trapping centers where before there were none. The new energy levels can hold a carrier (electron or hole) until the oppositely charged carrier comes along to cause a recombination process. If these recombination centers are more likely to reemitt the carrier before it can recombine, then the center is deemed a trapping site.

Carriers no longer need the gap energy to transition from the valance to conduction band. The trapping and recombination sites allow transitions at energies much less than the band gap energy. The magnitude of the energy difference depends on where the trap resides within the forbidden energy region. Figure 4.2 represents a semiconductor with trapping and recombination sites located in the forbidden region. The energy necessary to move an electron from the valance band to the trap site depends on where in the forbidden region that the trap lies. Trapping sites close to the valance band will

require little additional energy to promote a transition, where traps closer to the conduction band require energies nearer to  $E_{gap}$ .

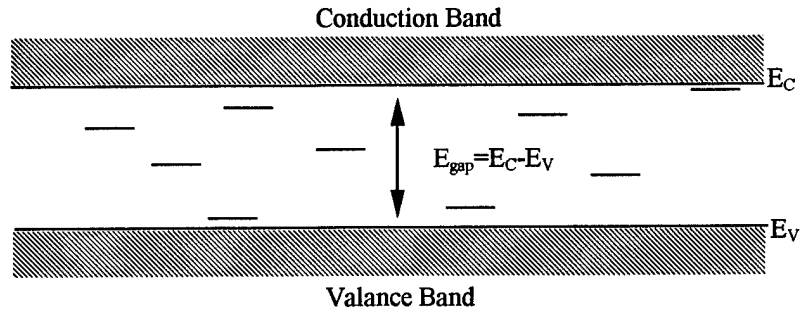


Figure 2.2. Band Structure of a Semiconductor with Impurities within the Bandgap Region.

These trapping and recombination centers will effect the operation of a device depending on how the device is operated.

### 2.3 Displacement Damage

Displacement damage is a result of neutrons interacting with the atoms of a given material. Being a neutral particle, the neutron will interact by way of the nuclear force giving rise to scatter or absorption. For most solid state materials, only scattering reactions are important due to the extremely low probability of absorptive reactions (e.g., fission or radiative capture). These scattering reactions will either be elastic or inelastic.

The probability per nucleus that a neutron in a beam will have an interaction is proportional to the microscopic cross section  $\sigma$  [26] which is a complex function of the neutron's energy. There is a higher probability of interaction for thermal neutrons (neutrons with an energy  $\leq 0.025$  eV) than fast neutrons (neutrons with energy  $>1$  MeV). The interaction cross section tends to go as  $E^{-1/2}$ ; however, there are resonances where the

cross section increases by orders of magnitude. Thus neutrons with an energy close to the resonance energy will most likely interact through whatever mechanism the cross section represents. This could be non-fission absorption, scattering, radiative capture, etc...

These resonances are important when trying to determine the number of displacements. It is to be hoped that there are few neutrons close in energy to a resonance energy. This will help to decrease the total amount of damage.

In order to find the number of displacements, two important material properties need to be determined: number density and mean free path. The number density is a measure of how many atoms are within a cubic centimeter volume.

$$N = \frac{\rho N_A}{MW} \quad (2.8)$$

where:

$\rho$ : the density of the material  
 $N_A$ : Avogadro's number  
 MW: Molecular weight

When the number density for a material is determined the total probability of interaction per centimeter of travel is given by the macroscopic cross section:  $\Sigma = N\sigma$ . The mean free path ( $\lambda$ ) is the inverse of the macroscopic cross section representing the mean distance between collisions.

Messenger and Ash present a method for calculating the total number of displaced atoms from a neutron fluence [4].

$$N_d = N \int_{E_{th}}^{E_{max}} dE \int_{E_d}^{E_{max}} dE_r N_s(E_r) \sigma_D(E, E_r) \phi_n(E) \quad (2.9)$$

where:

$\phi_n(E)dE$ : neutron fluence within energy interval  $dE$   
 $\sigma_D(E, E_r)$ : cross section for producing a PKA with energy  $E_r$   
 $N_s(E_r)$ : number of displaced atoms that expend all of their energy  $E_r$   
 $E_r$ : energy received from a PKA  
 $E$ : incident neutron energy  
 $E_{th}$ : threshold energy required to dislodge an atom from the lattice  
 $E_d$ : maximum energy transferable to the PKA from an incident neutron  
 $E_{max}$ : maximum energy received from a PKA  
 $E_{max}$ : maximum neutron energy

Equation 2.9 may be rewritten as the product of two integrals to a good approximation, since the mean free path ( $\lambda$ ) varies slowly over the incident neutron energies [4]:

$$N_d \cong \int_{E_{th}}^{E_{max}} \phi_n(E) dE \int_{E_d}^{E_r max} \frac{N_s(E_r)}{\lambda} dE_r \quad (2.10)$$

This product represents the total fluence of neutrons ( $\Phi_n$ ) that have the ability to cause a displacement reaction times the expected number of defects produced at energy  $E_r$  within  $dE_r$ , per mean distance to a collision. The final simplification arises from the fact that the macroscopic cross section varies slowly over the decades of neutron energies.

$$N_d \approx \Phi_n \frac{n_s}{\lambda} \quad (2.11)$$

where:

$$n_s = \int_{E_d}^{E_r max} N_s(E_r) dE_r$$

Equation 2.11 states that the total number of displaced atoms ( $N_d$ ) is given as the product of the number of PKAs produced per  $cm^3$  ( $\Phi_n/\lambda$ ) and the average number of displaced atoms per PKA ( $n_s$ ). This allows for an estimate of the total number of displaced atoms per unit volume ( $cm^3$ ) for a given incident neutron fluence ( $\Phi_n$ ). The displaced atoms

will form defects that can be presented as either clusters of defects or randomly spaced point defects scattered throughout the volume of the material.

An early model put forth by Gossick proposed that the dominant damage mechanism resulting from neutron irradiation was due to the formation of these defect clusters and not from isolated point defects [18]. These Gossick clusters are supposed to have a core of ionized defects with a surrounding ring of depleted carriers, and therefore being of opposite charge. The net effect of Gossick clusters was the formation of small intrinsic regions that would be large recombination centers for minority carriers and increase the bulk resistivity [4]. In effect these Gossick clusters had formed spherical p-n junctions.

A problem with the Gossick model is that there are not enough excess carriers available to create these clusters. There is approximately one carrier removed for every PKA produced per unit incident neutron fluence per cubic centimeter [4]. This does not allow enough excess carriers to be trapped to form the cluster. Additionally, if these were truly occurring then one would see different effects when charged particles interacted in the same manner. Through NIEL a linear relationship demonstrated damage correlation over several orders of magnitude for neutrons, protons, and electrons that disputes the hypothesis of the clusters (Figure 1.4). The damage per unit fluence was determined to be essentially the same [4]. Therefore, it is the random point defects that are the heart of the neutron damage.

The point defects created from the interstitial-vacancy pairs produce trapping and recombination centers within the forbidden energy gap of a material. Between the

conduction and valance band new energy levels are created that allow lower energy photons access to either the valance band, conduction band, or trapping-recombination sites (Figure 4.2). The overall effect is the production of trapping sites that allow for incoming photons to be absorbed more readily within a material. Thus displacement damage should increase as point defects are created upon exposure to a neutron fluence. Device parameters are necessary to characterize the manifestation of the damage along with a tool to predict further degradation.

### 2.3 Messenger-Spratt Equation

Tools to predict the changes in device parameters are in the form of the Messenger-Spratt common emitter gain relations.

$$\Delta\left(\frac{1}{\beta}\right) = \frac{1}{\beta} - \frac{1}{\beta_i} = \frac{\Phi_n}{K_\beta \omega_T} \quad (2.12)$$

where:

- $\beta$ : common emitter current gain
- $\beta_i$ : initial common emitter current gain
- $\Phi_n$ : neutron fluence
- $\omega_T$ : inity gain corner frequency
- $K_\beta$ : camage constant

The common emitter current gain degrades upon neutron irradiation after there is a sufficient fluence to make  $\Phi_n/(K_\beta \omega_T)$  non-negligible.  $K_\beta$ , a parameter damage constant, is represented in t is a measure of the ability of a device to withstand a neutron fluence.

Sets of Messenger-Spratt equation types can be found for many bulk parameters.



Degradation of the minority carrier lifetime has the same form as the common emitter gain degradation. Here the relationship has been rearranged so that the carrier lifetime is dependent upon the initial lifetime and the neutron fluence.

$$\frac{1}{\tau} = \frac{1}{\tau_i} - \frac{\Phi_n}{K_\tau} \quad (2.13)$$

The minority carrier lifetime is reduced due the formation of the point defect formation of trapping and recombination centers. In other words, these loss centers remove the minority carriers as they are transported across the base of the device [4].

Upon irradiation a DBR loses some of its effectiveness. This is a result of trapping and recombination centers that remove the photons from the incident waveform. Thus the index of refraction is analogous to the minority carrier lifetime. The trapping and recombination centers remove photons traveling through the material. One affects the lifetime of the minority carriers, while the other affects the material properties of absorption. Therefore, it is plausible to model the index of refraction by a Messenger-Spratt relationship as well. The complex index of refraction, or the extinction coefficient, represents frequency dependent absorption within a material. The extinction coefficient represents a mean time or distance for photon absorption, much in the same manner as the time it takes a minority carrier to combine with a majority carrier ( $\tau$ ). Thus, it stands to reason that the index of refraction should have the same type of behavior as the minority carrier lifetime due to the increased trapping and recombination centers. These defect sites represent areas where photons can be lost through absorption. Material reflectance is tied directly into the index of refraction through equation 2.7. Therefore we will represent a change in the reflectance analogously to equation 2.13.

$$\frac{1}{\mathfrak{R}} = \frac{1}{\mathfrak{R}_i} - \frac{\Phi_n}{K_{\mathfrak{R}}} \quad (2.14)$$

or: 
$$\Delta\left(\frac{1}{\mathfrak{R}}\right) = \frac{1}{\mathfrak{R}} - \frac{1}{\mathfrak{R}_i} = \frac{\Phi_n}{K_{\mathfrak{R}}}$$

An extrapolation to all other particles can be performed from an initial displacement damage relationship (as a function of neutron fluence) of a bulk parameter. Through the non-ionizing energy loss theory (NIEL) a displacement damage based on the kinetic energy released in the material (KERMA) of one particle can be extrapolated for all others. KERMA is analogous to the linear energy transfer for ionizing particles. A linear relationship has been found [20] from attempts at correlating damage on devices to different particles. The result is a relation between different particles at various energies.

$$NIEL = (N_A/MW)(\sigma_e T_e + \sigma_i T_i) \quad (2.15)$$

where:

$N_A$  = Avogadro's number

$MW$  = molecular weight

$\sigma_i$  = total inelastic cross section

$\sigma_e$  = total elastic cross section

$T_i$  = average recoil energy for inelastic collisions

$T_e$  = average recoil energy for elastic collisions

A more accurate relationship for NIEL considers the angular dependence of the collision as the product of the recoil energy and the differential scattering cross section [20]

$$NIEL = \frac{N_A}{MW} \int_{\theta_{\min}}^{\pi} L[T(\Theta)]T(\Theta) \frac{d\sigma}{d\Omega} d\Omega \quad (2.16)$$

where:

$T(\Theta)$ : recoil energy in direction  $\Theta$

$L[T(\Theta)]$ : fraction of the recoil energy transferred into displacements

$MW$ : Molecular weight

By knowing a single damage constant for one particle, all other particles can be determined through a NIEL curve. The x-axis of a NIEL curve is based on the amount of displacement energy given up in [Energy-Area/Mass]. The y-axis, logarithmic like the x-axis, represents a specific damage constant. From an initial, experimentally determined, damage constant, a one-decade per decade slope is drawn to extrapolate to all other particles. In order to do this, a damage constant needs to be found for any type of particle.

Mono-energetic sources that provide a substantial fluence for testing are hard to find. A broad band energy spectrum is folded into an equivalent mono-energetic spectrum [17]. Neutron damage is represented by a 1 MeV equivalent fluence of Si or GaAs, and a Si fluence is more commonly used. A mono-energetic fluence is determined by the ratio of the first moment of the fluence to a KERMA for a given material [21].

$$\Phi_{eq}(E_0) = \frac{\int \Phi_{eq}(E) K_D(E) dE}{K_D(E_0)} \quad (2.17)$$

Thus, all broad energy neutron spectrums can be folded into a single mono-energetic equivalent fluence, for a known material, for comparison of the displacement damage.

## 2.4 Annealing

Displacement damage can be transient or permanent. Most of the Frenkel defects are unstable at room temperature, and the random thermal motion of the atoms may allow for the Frenkel pairs recombination. This recombination process is helpful in reducing the total damage in a material. A competitive process is the formation of divacancies that

cause further degradation. Divacancies occur when an atom from a Frenkel pair combines with an impurity to form a stable compound at room temperature. There are two ways to attempt to reduce the total amount of displacement damage: isothermal and isochronal annealing.

Isothermal annealing is accomplished by waiting for time to correct any neutron damage. This relies upon the random thermal motion of the atoms to cause the Frenkel pair recombination with hopes of minimum divacancy formation. If the sample was heated to increase the thermal motion of the atoms as well as increase the spacing distance of the lattice, then the damage may be annealed at a faster rate. This isochronal annealing essentially speeds up the time by quickly giving the defect sites the thermal energy to find their way back to a normal lattice site. There is an increased rate of divacancy formation in isochronal annealing, but normally the Frenkel defect recombination will occur at a much faster rate. This only applies if the lattice is not raised to a high enough temperature where recrystallization or amorphization of the device occurs.

### III. Experimental Procedures

This section begins with the composition and growth of the samples used in the irradiation study. The sample growth is followed by the experiments performed to determine the damage constant for the DBR structures: absolute and relative reflectance measurements. The surface reflectance was measured with two different configurations: one determined if there was any spectral shift or change in the spectral shape, and the other determined the magnitude of any amplitude shift after irradiation. The experimental platform used to characterize electrical pumped VCSEL is outlined along with the measurements needed to determine the current threshold shift, spectral change, and change in slope efficiency. Appendix C lists all of the equipment utilized to perform the necessary measurements.

#### 3.1 Sample Growth

There were three sample types used for this thesis investigation all grown from a substrate of GaAs by metal organic chemical vapor deposition (MOCVD). The two samples used to determine the damage to the DBR structures were designated XC0911a (VCSEL) and XC1118b, both grown at Sandia National Laboratory. The electrically pumped VCSELs, designated E319, were grown at the University of New Mexico. Growth of the three samples is outlined below.

The VCSELs used for the DBR study were composed of alternating layers of  $\text{Al}_{0.5}\text{Ga}_{0.5}\text{As}$  (high index material),  $\text{Al}_{0.75}\text{Ga}_{0.25}\text{As}$ , and AlAs (low index material). From the substrate, forty and a half alternating periods were deposited in a two step fashion

comprising layers that are a quarter wavelength thick (Figure 3-1). The lower DBR stops as a 420 Å barrier layer of  $(Al_{0.7}Ga_{0.3})_{0.5}In_{0.5}P$  begins for the three quantum well structures composed of  $Ga_{0.44}In_{0.56}P$ . A barrier layer is deposited after each quantum well, and both

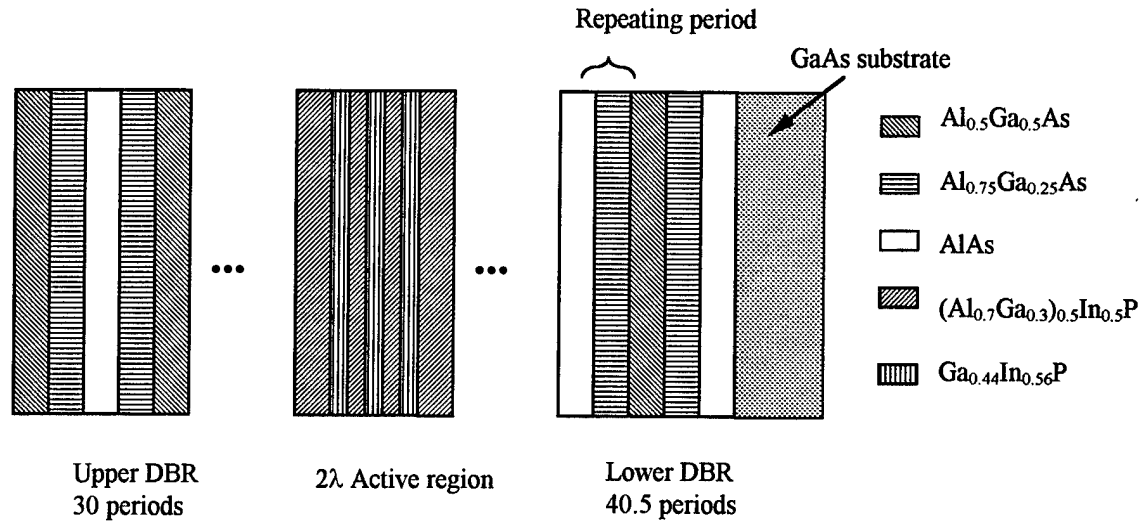


Figure 3-1. Growth of the DBR VCSEL: XC0911a

well and barrier are deposited in 100 Å layers. An additional 420 Å barrier is laid finishing the  $2\lambda$  cavity before the top DBR is deposited. The upper DBR has the same structure of the lower DBR except it has thirty periods. A 100 Å cap layer of GaAs is laid down on the last layer to finish the structure. This GaAs layer is not added on top of the last layer, it replaces the last 100 Å of  $Al_{0.5}Ga_{0.5}As$  keeping a quarter wavelength layer.

The DBR mirror, XC1118b, has a similar structure to the DBR of XC0911a (Figure 3-2). Twenty period pairs of material are laid down onto a GaAs substrate. The pairs are composed of  $(Al_{0.7}Ga_{0.3})_{0.5}In_{0.5}P$  as the high index material, and  $Al_{0.5}In_{0.5}P$  as the low index material. A 100 Å cap layer of GaAs finishes the structure just as it was done in

XC0911a. The contact layer replaces 100 Å of the  $(\text{Al}_{0.7}\text{Ga}_{0.3})_{0.5}\text{In}_{0.5}\text{P}$ , keeping it a quarter wavelength layer.

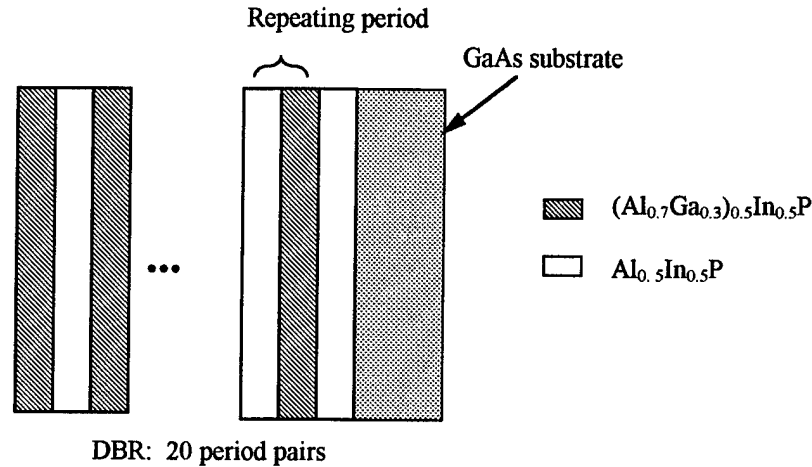


Figure 3.2. Growth of the DBR Mirror: XC1118b

The last structures used in this study were the electrically pumped VCSELs from the Center for High Technology Materials at the University of New Mexico. The exact structure is considered proprietary, but the essentials of the design follow (see Figure 3.3). The lower DBR, grown on the GaAs substrate, consists of 35.5-43.5 periods of linearly graded  $\text{Al}_x\text{Ga}_{1-x}\text{As}$ , where the mole fraction runs from  $\text{Al}_{0.15}\text{Ga}_{0.85}\text{As}$  to  $\text{AlAs}$ . A period consists of the linear grade up to and down from  $\text{AlAs}$ . There is a linear grade up to the barrier for the  $3\lambda$  active region. The active region is composed of four GaAs quantum wells spaced by barriers of  $\text{Al}_{0.15}\text{Ga}_{0.85}\text{As}$ . The upper mirror begins after a linear grade down in the gallium mole fraction and subsequent increase in the aluminum mole fraction

to AlAs. The upper stack is a replica of the lower mirror; although there are 23-30 period pairs. The structure is finished by the placement of a cap layer.

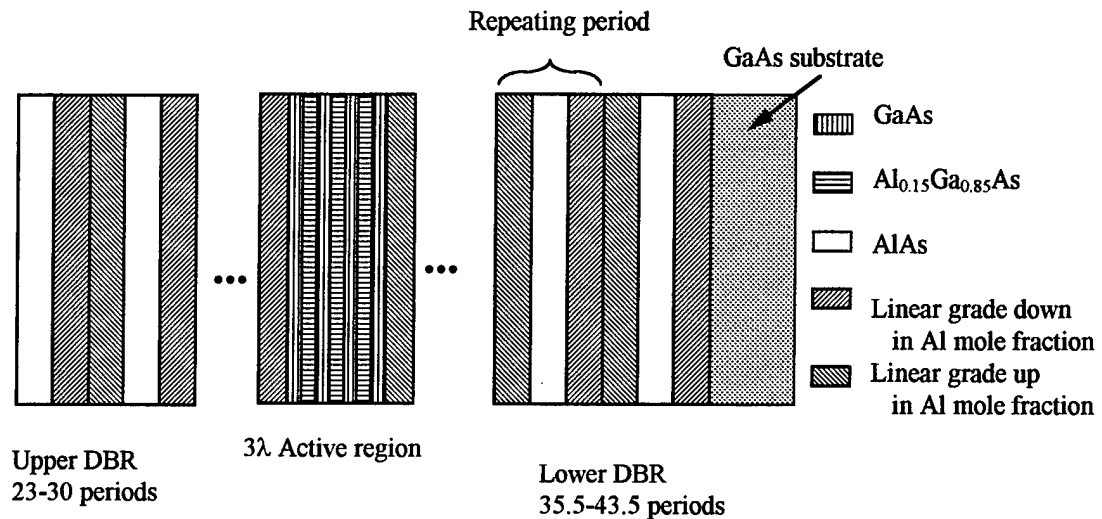


Figure 3.3: Growth of the Electrical Pumped VCSELs: E319

### 3.2 Laboratory Configuration

The reflectance measurements were performed to determine how the DBRs responded to increasing neutron fluence. Both absolute and relative reflectance measurements were performed before and after each irradiation. The relative measurements reflected a broad band white light source off the sample surface; whereas the absolute measurements reflected a tunable Ti-sapphire laser off the sample.

The relative reflectance measurement was configured as in Figure 3.4. The light from the broad band white light source was focused onto the sample, which was mounted on a translation stage. Light reflected from the surface was sent to the optical multi-channel analyzer (OMA) through a beam splitter and turning mirror. Light intensity



versus wavelength was plotted through the data acquisition system connected to the OMA. A reference spectrum was taken over 580-880 nm with a New Focus broadband infrared (IR) high reflectance silver mirror ( $R > 0.95$  from 600-3000 nm) after verifying the optical alignment of the light path. Several measurements at different locations were taken for the same spectral range on a single sample. The reference mirror and sample files were divided to obtain a reflectance spectrum relative to the IR mirror.

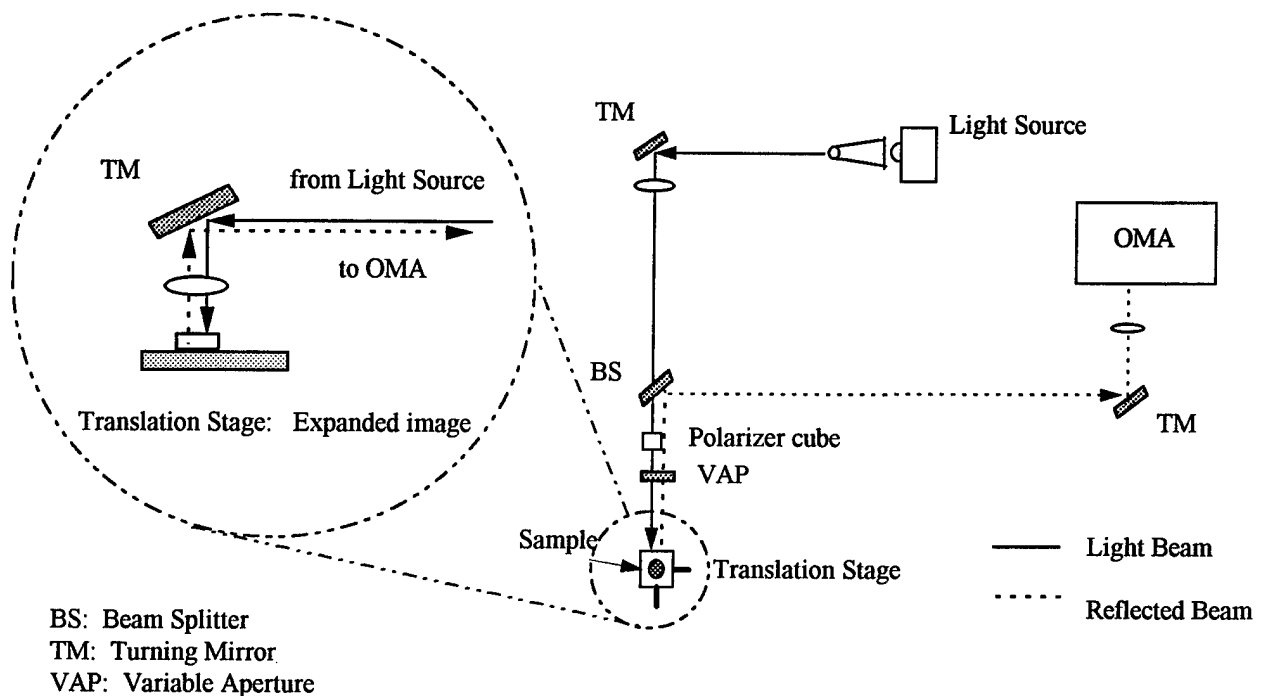


Figure 3.4: Line Diagram of the Relative Reflectance Measurement Set-up

The spectrum was acquired by the OMA using a grating having 600 lines/mm. The light was initially focused on the reference mirror by retroreflection and the intensity was maximized before any data was taken. VCSEL and DBR mirror sample data were taken with the optimized intensity equipment settings from the reference mirror. A

translation “reference zero” was determined by placing the focused beam on a specific corner of the sample. Measurement spots and locations were based on this reference. Before data was collected on the sample, the beam was refocused by retroreflection to account for the thickness difference between the reference mirror and samples. This procedure was repeated for each spot location and sample both before and after neutron irradiation.

In order to insure repeatability of the measurements, several procedures were followed. A special sample holder was made to ensure that the samples had the same reference plane for all the measurements. The orientation of the sample to the reference plane was recorded for all future measurements. Spectral data for each of the spot locations were obtained after subtracting the ambient background light that reached the detector. All of the data files were saved for analysis. To further ensure that the measurement was both unbiased and repeatable, reference reflectance measurements were taken on control samples that were not irradiated, and did not leave the optical laboratory. These three controls minimized the probability that there was an experimental bias to the data.

The absolute reflectance measurements were performed at a different platform than the relative reflectance measurements, as depicted in Figure 3.5. The beam path of the Ti-sapphire was verified before measurements began. Absolute reflectance was based on the fraction of the intensity of the Ti-sapphire after it reflected off of the sample. The first turning mirror was mounted on a sliding fixture to allow wavelength measurements. A calibrated wavemeter was used to determine the laser’s wavelength by sliding the first

turning mirror so that the beam could go directly into the wavemeter. When the turning mirror was released, the beam traveled through an optical isolator, to prevent feedback, and a lens pinhole combination to collimate the beam. The beam was then focused onto the surface of the sample so the reflected light could be collected at a powermeter.

First the sample was mounted on the translation stage and imaged on to a camera by illuminating it with a visible light source. A corner edge was aligned to the edge of the video screen for a reference zero. Translating the sample from the reference zero to a measurement location, data was taken. The absolute reflectance was calculated from four

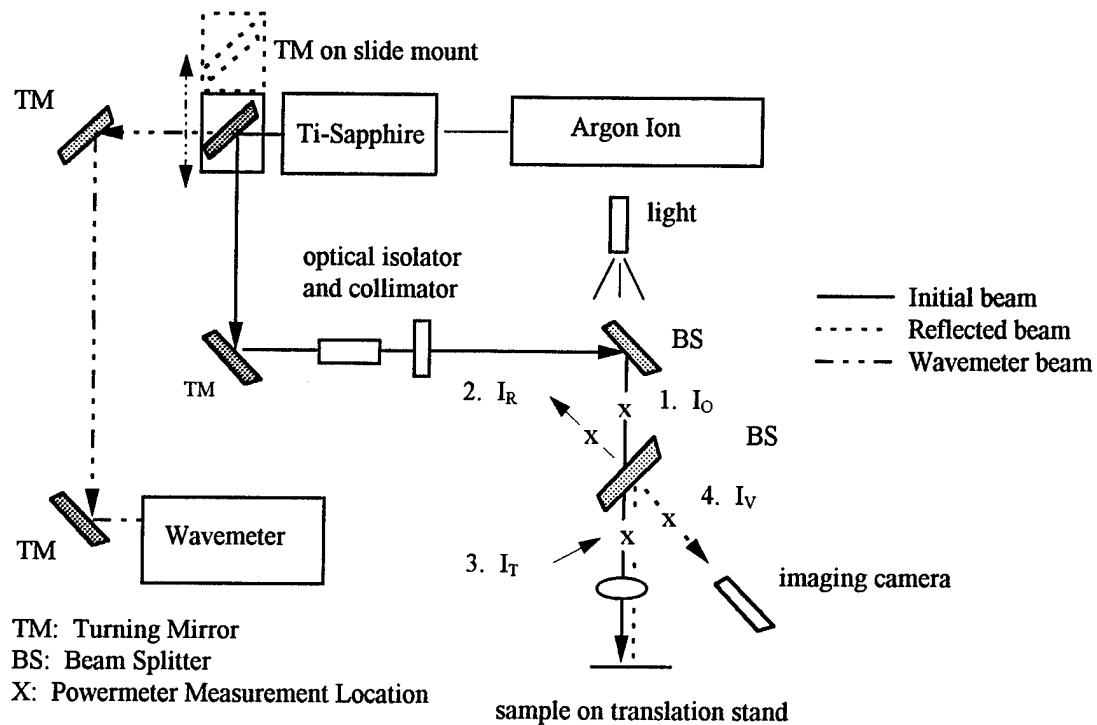


Figure 3.5: Line Diagram of the Absolute Measurement Platform Equipment Configuration

separate measurements taken for each wavelength at each spot location. The four measurements recorded with the power meter were:  $I_0$  -- initial intensity at location #1,  $I_R$  -- reflected intensity from the beam splitter at location #2,  $I_T$  -- transmitted intensity from the beam splitter at location #3, and  $I_V$  -- reflected intensity from the sample at location #4. Exploiting the range of the Ti-sapphire, reflectance was measured at eleven separate wavelengths from 840-710 nm. The high reflectance area for the two samples ran from 630-680 nm, and therefore only the longer wavelength sidebands could be reached. Reflectance data was taken at 840, 830, 820, 810, 800, 790, 750, 740, 730, 720, and 710 nm. Wavelengths between 755-785 were unobtainable due to a resonance in the wavemeter. This resonance accounts for the gap in absolute reflectance data presented in Section IV.

A similar reference slide was made to ensure that the samples had a constant alignment source for all of their measurements. The orientation of the samples were noted before they were mounted onto the slide. A control sample was used with each of the data sets to account for any variance of the measurement as well as ensuring repeatability.

The equipment configuration in Figure 3.6 was utilized for the electrically pumped VCSELs. This stand allowed for measuring the injected current, voltage drop across the device, power out of the VCSEL, and spectral data for a given injection current. Experimentally determined data was used to construct current versus voltage (I-V), light intensity versus voltage (L-I), and spectral data curves.

A sample was placed on the translation stand and imaged by the camera to determine the orientation of the sample for placement of the current probe. Once the

probe completed the circuit to the VCSEL, a sample spectral response was obtained by collecting the output light at the OMA. After the spectral data was taken, a power meter was placed in the VCSEL beam path to determine the output intensity. In order to develop the L-I and I-V curves, the voltage drop across the device, along with the injection current, were measured with digital multimeters.

The orientation of the VCSEL with respect to the camera was kept the same for both initial and final measurements. The first time a VCSEL was tested it was injected with a current that allowed the device to pass threshold. The current was turned off after the voltage stabilized allowing for device burn-in. Spectral data was taken at a given current ( $I_{max}$ ) depending on the size of devices' aperture. Voltage, current, and power (light intensity) were taken for each device spanning  $0-I_{max}$ . Control samples were used with each VCSEL sample batch for the electrical characterization measurements.

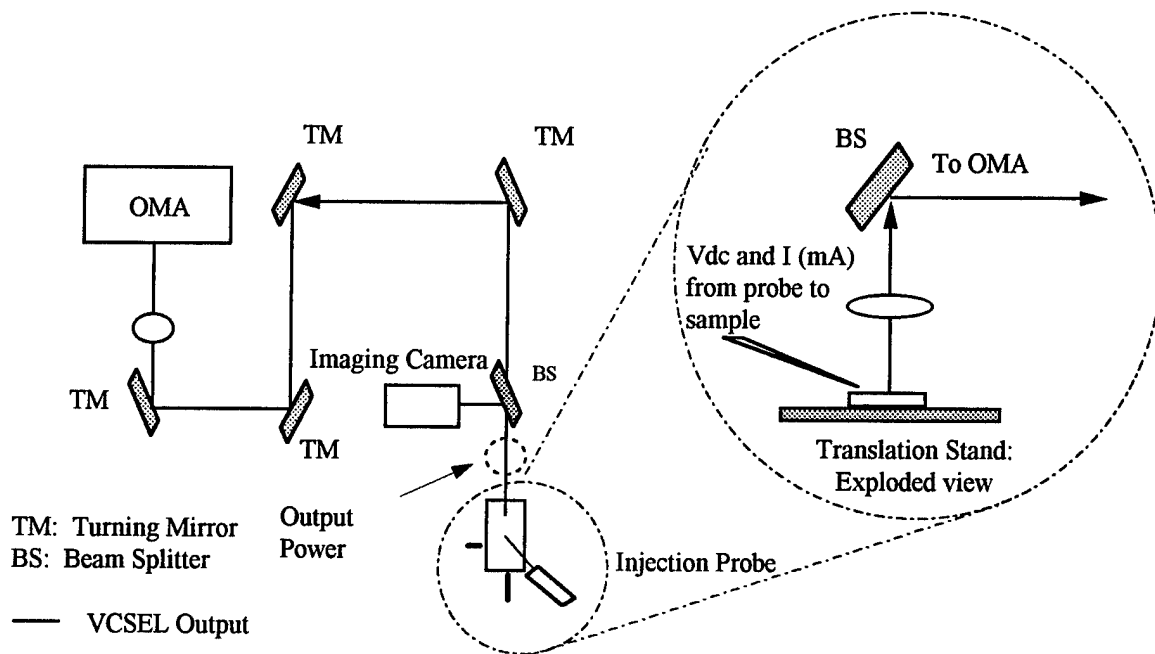


Figure 3.6: Line Diagram of the Electrical Pumping Platform Equipment Configuration

All of the data for each of the samples were taken with the use of the three experimental configurations outlined above. When isochronal annealing effects were considered, a hot plate was used to heat up the samples. The samples were allowed to cool and placed back on the same test configurations for additional measurements.

### 3.3 Test Matrix

Three different sample sets were used for the irradiation study. The DBR mirror and VCSEL samples were cleaved into various sample sizes for the study. Appendix B shows how each of the original one inch wafers were divided and labeled. Table 3.1 below lists the irradiation sample set number, DBR mirror and VCSEL sample identification, and electrically pumped VCSEL identification.

Table 3.1. Irradiation Set Component Breakdown.

Sample Set Number	DBR Mirror	DBR VCSEL	Electrically Pumped VCSEL
Fact Finding #1	#1 and #2	#1	N/A
1	(3,0) (2,0)	(1,-1) (2,-1a)	N/A
2	(0,0) (1,0)	(2,-2a) (1,-2)	N/A
3	(0,1)	(1,-3a)	1
4	(1,1)	(1,-5)	2 *
5	(2,1)	(2,-5)	4
6	(3,1)	(3,-5)	5 *
7	(0,2)	(2,-4b)#1	7 *
8	(1,2)	(3,-4)	9
9	(2,2)	(4,-4)	10
10	(3,4)	(1,-4)	10'
11	(4,2)	(2,-4a)	11
12	(3,2)	(1,-3)	12

\*Lost Sample

The irradiation program was laid out to cover a broad neutron fluence spectrum to determine an effective damage constant. This study ran through seven orders of magnitude covering a range of  $10^{10}$ - $10^{17}$  neutrons/cm<sup>2</sup> 1 MeV equivalent (Si). Previous radiation studies on electrically pumped VCSELs have shown that appreciable damage starts to appear around  $10^{14}$  neutrons/cm<sup>2</sup> 1 MeV equivalent (Si) [19]. Through testing samples with neutron fluences approximately three decades above and below where the expected damage is to occur, a full damage curve can be found with a well defined knee. Table 3.2 covers the irradiation date, date of the initial post irradiation measurement, and fluence levels for each of the sample irradiation's as the search was conducted for the damage constant.

Table 3.2. History of the Irradiation Sample Sets

Sample Number	Desired kW-min	$\Phi$ (1 MeV Si) [neutrons/cm <sup>2</sup> ]	Irradiation Date	Initial Measurement Date (Post Rad)
0	30,000	$6.07 \times 10^{16}$	26 Apr 1995	26 Apr 1995
1	72,000	$1.46 \times 10^{17}$	19 Jul 1995	27 Jul 1995
2	72,000	$1.46 \times 10^{17}$	1 Aug 1995	11 Aug 1995
3	12,000	$2.43 \times 10^{16}$	10 Aug 1995	14 Aug 1995
4	5	$1.01 \times 10^{13}$	25 Aug 1995	29 Aug 1995
5	25	$5.06 \times 10^{13}$	25 Aug 1995	28 Aug 1995
6	100	$2.02 \times 10^{14}$	25 Aug 1995	29 Aug 1995
7	25	$5.06 \times 10^{13}$	8 Sep 1995	14 Sep 1995
8	0.05	$1.01 \times 10^{11}$	4 Sep 1995	7 Sep 1995
9	0.5	$1.01 \times 10^{12}$	6 Sep 1995	7 Sep 1995
10	500	$1.01 \times 10^{15}$	11 Sep 1995	13 Sep 1995
11	15000	$3.03 \times 10^{15}$	8 Sep 1995	13 Sep 1995
12	1	$2.02 \times 10^{12}$	8 Sep 1995	13 Sep 1995

The initial "fact finding" samples, set #0, were irradiated at a high level to determine if the samples were going to be a radiation hazard. An activation model was

made for the three sample types before any sample was sent to the reactor for irradiation. The model takes into account each of the constituent atoms, their volume, and the isotopic concentrations. These factors are folded into an ingrowth-decay model. The irradiation profile was designed to screen out thermal neutrons by shielding the samples with cadmium covers. Cross section from Erdtmann and LeClerc [27,28] were used for the epithermal resonance cross sections. The activation products were calculated from the transmutation of the initial stable isotopes, total activity in Curies for a given beam time. The activity follows a normal exponential decay once the irradiation time is finished. This allowed a first order calculation to ensure that the samples would not be sent to the reactor which would become too radioactive to safely handle.

The models determined that there should not be any significant exposure hazard for any of the samples, and the first fact finding run confirmed the initial calculations. A radioactive survey by OSU of sample set #0 initially after the irradiation found that the DBR Mirror #1 had an activity level of 668  $\mu\text{Ci}$ . The Mathcad model predicted an activity of 2.4 mCi and 12 mCi for the thermal and epithermal cross sections respectively for the ingrowth. These values were off by a factor of 4 and 20 activity using OSU's reported flux of  $3.14 \times 10^{14}$  neutrons/cm<sup>2</sup>-sec. OSU also reported that the total neutron flux above 1 MeV was  $9.8 \times 10^{11}$  neutrons/cm<sup>2</sup>-sec. Using this value for the total flux, the model predicts an activity of 900  $\mu\text{Ci}$  and 6 mCi for thermal and epithermal cross sections respectively. These new predicted activities are off by a factor of 1.35 and 9. A reasonable assumption is that the actual activity lies somewhere between those values obtained with the total flux over the entire energy spectrum and total flux above 1 MeV.



It was determined that the initial representation for the sample growth as inaccurate. Correcting the structural information changed the number densities; although, the change was on the order of one percent. Resulting activities did not differ from the initial result. The most likely source of error in the program comes from the calculated density of the  $\text{Al}_x\text{Ga}_{1-x}\text{As}$  and  $(\text{Al}_{0.7}\text{Ga}_{0.3})_{0.5}\text{In}_{0.5}\text{P}$ . No known value of the density could be found, and the density was calculated by taking the sum of the individual elemental densities times their mole fraction divided by the total molecular weight. Calculated densities using this method to known compounds, were higher than the actual values. The conclusion of the Mathcad model was that it allows for a high upper bound of the activity for the structures.

#### **3.4 Ohio State University's 500 kW Research Reactor**

The neutron irradiation was performed through the Department of Energy's Reactor Sharing Program at Ohio State University's research reactor. The samples were placed on the end of beam port #1 as depicted in Figure 3.7. A 0.5 mm cadmium cover shielded the samples from thermal neutrons to reduce thermal activation products.

The samples were mounted on the aluminum plate on the end of the beam port plug (Figure 3-8). After covered the samples with cadmium, the plug was slid into the neutron beam port. The port allows neutrons from the reactor and surrounding environment to stream through the port until they interact with the beam port plug. The plug does not contain any hydrogenous material, and therefore there is virtually no attenuation as the particles stream through the tube. Particles will interact with any material obstructing the streaming path.

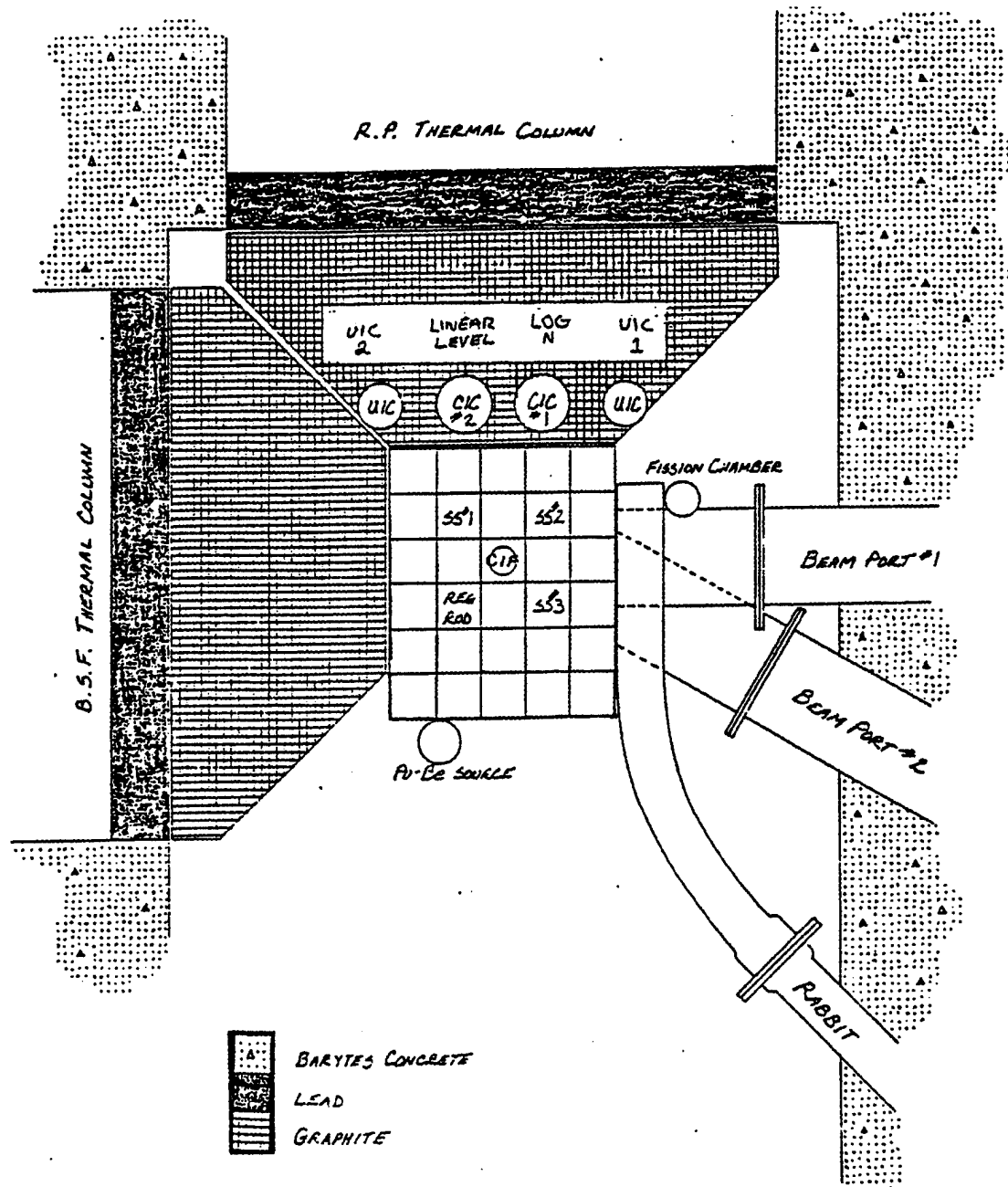


Figure 3.7 Ohio State University's 500 kW Research Reactor- Top down diagram, courtesy OSURR

Neutron fluences within the beam tube are attenuated after hitting the cadmium covered samples. The plug was designed so that there would be minimal scattering back to the source. Low Z materials provide efficient thermalization of neutrons, i.e. slow them down to thermal energies. The plug design starts with the reactor grade graphite to initially slow the neutrons. Borated concrete has a two fold benefit. First the boron ( $^{10}\text{B}$ ) has a huge absorption cross section to remove neutrons from the stream. Secondly, the concrete contains water. Hydrogen is the best scatterer since a neutron can lose up to half of its energy in one collision with a hydrogen atom. The borated polyethylene provides neutron absorption and scattering. Any neutrons getting to the borated polyethylene are quickly absorbed. This graded plug reduces any potential of backscattering. Thus target samples and measured flux calculations should not be biased from the back scattering of neutrons.

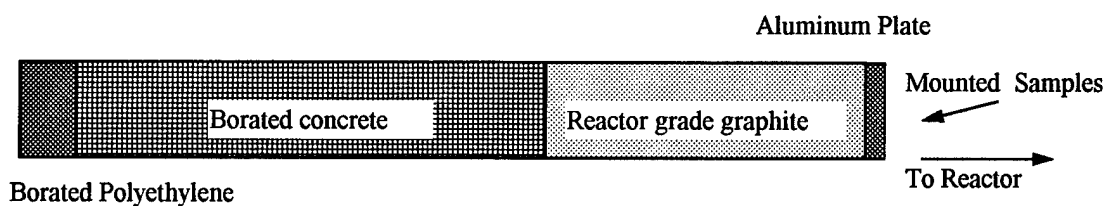


Figure 3.8: Reactor Plug for Ohio State University's Research Reactor

After each irradiation run, the samples were counted and packaged for shipping to Wright-Patterson AFB. All of the samples were checked into the Base Radiation Safety Office before any experimentation was performed on the irradiated samples. The samples are under the control of the Base Radiation Safety Office until they qualify the samples as non-radioactive debris.

After the longest lived activation product decays past approximately ten and a half half-lives, the sample can be considered normal waste. This time represents the time for the most significant isotope ( $^{76}\text{As}$ ) to decay, which is approximately 11 days after an irradiation ( $T_{1/2} = 26.3$  hr). Appendix D lists the explicit procedure for handling the radioactive material.

Whenever samples were sent to OSU for irradiation the irradiation time was specified in terms of kW-min. The operational staff at OSU decided the best power and irradiation time to meet the desired kW-min. Due to the fact that reactor power increases exponentially until it reaches a plateau, the time in the plateau was maximized to count the exponential power rise and fall as negligible. This allowed for a more accurate estimate of the neutron fluence that hit the samples.

### 3.5 Dosimetry

All of the neutron flux monitoring was performed at Ohio State by the reactor staff. Neutron flux wire was placed in the same configuration as samples to determine the most probable neutron flux. A differential energy flux calculated through the SAND-II neutron spectrum unfolding code. OSU performed the SAND-II runs using the flux wire to determine the neutron flux (Figure 3.9). The spectrum is obtained from the activation of the multiple flux wires along with assumptions of the spectrum's shape between fission and thermal energies. The spectrum shapes are normally chosen to be Maxwellian for the thermal range (0~0.5 eV),  $1/E$  for the resonance region (0.5 eV ~ 1.0 MeV), and a fission spectrum,  $\chi(E)$ , based on the reactor's fuel for the fast region (1.0 MeV -  $\infty$ ).

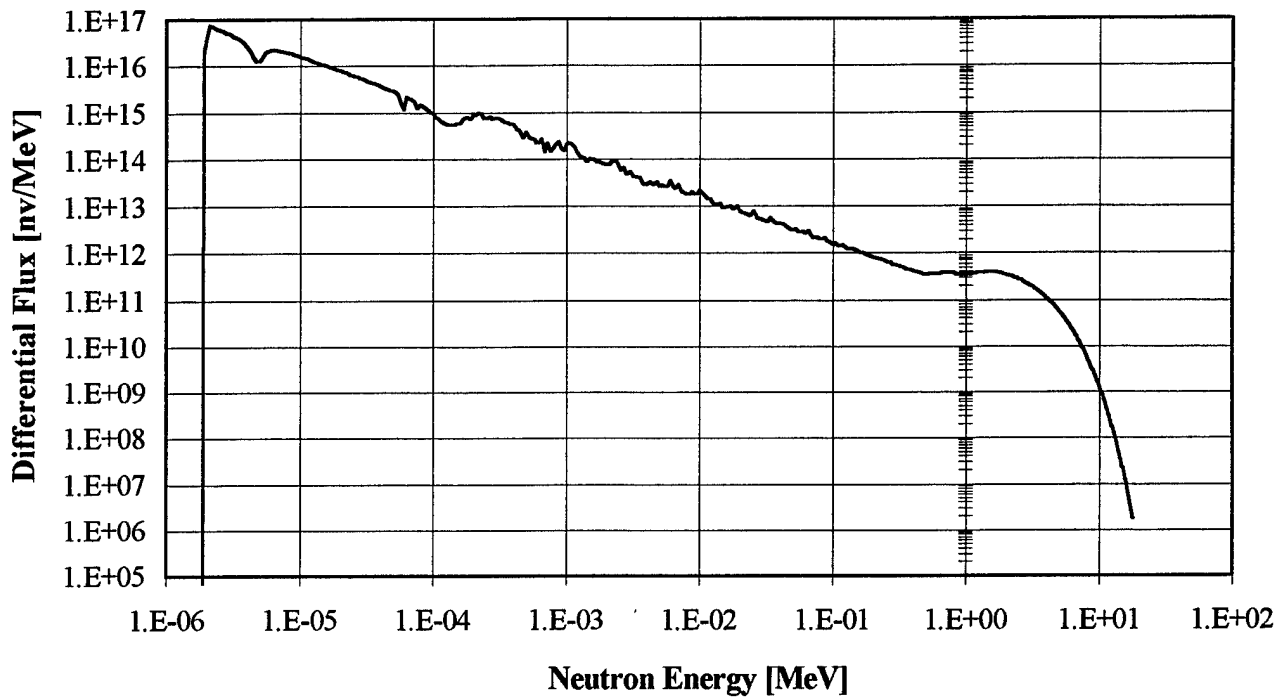


Figure 3.9. Representative Differential Flux at 400 kW in Beam Port 1

This differential spectrum is used to calculate the 1 MeV equivalent fluence in accordance with ASTM E 722-85 [21]. The flux measurement is important since the damage constant is based on the exposure of the samples. The spectrum drops sharply around 1 eV due to the cadmium cutoff. Cadmium was used to cover the samples to reduce thermal neutrons thereby reducing the activation products.

## IV. Data Analysis

The results presented in this section cover the theoretical and experimental techniques used to determine the displacement damage on DBR structures. The initial theoretical spectral response program is presented before any of the experimental data. Both DBR structures, VCSEL and mirror, are examined for their relative and absolute reflectivity responses. From the reflectance data a damage constant for each structure can be obtained. The methodology in obtaining the damage constants is outlined. The chapter concludes with a comment on the work with the electrically pumped VCSELs.

### 4.1 Theoretical Change in Reflectance

There have been numerous studies on neutron damage to solid state devices [12, 19], but none have specifically looked at the DBRs used to make the devices. The initial hypothesis for the project was that the reflectance should decrease for irradiated structures due to point defects. These defects should add additional loss from absorption and scattering that was not present before irradiation.

A theoretical model was necessary to confirm the hypothesis. The tool employed was a Mathcad program created by Fitzgerald [24] in designing resonant cavity light emitting diodes (RCLEDs). RCLEDs have fewer period pairs to their DBR structures than VCSELs. Therefore, the cavity is dominated by losses and will never obtain the population inversion required for lasing. The model is representative of the materials used in the DBR samples for this study (AlGaAs).

Design parameters were changed to reflect a VCSEL with an optimal wavelength of 850 nm. The model used 30 and 38 pairs for the upper and lower DBR respectively.

The effect of photon scattering and absorption was attempted through the use of Fitzgerald's Model [24]. Both models involved changing the extinction coefficient and computing the resulting reflectance spectrum. An initial reflectance spectrum obtained through data by Aspnes and Adachi [13, 14] were used to compare the results of the model.

Absorption of light in the structures was modeled by adding a constant factor to the extinction coefficient. By adding a constant through the entire energy spectrum, the absorption increased everywhere. The increase was not proportional across the wavelength range since some values would be affected more than others. Figure 4.1 depicts the results of three different additive values. The shape is distorted by raising the low reflectance region and lowering the high reflectance region. Hence, the reflectance spectrum appears to be compressed in amplitude. Additionally, the reflectance at shorter wavelengths are changed more than the longer wavelengths. This can be seen by the shoulder around 812 nm which is softer than the longer wavelength shoulder at 900 nm.

The effects of the loss were further explored by utilizing a step increase to the extinction coefficient for wavelengths below a turn-off wavelength. Since absorption will be more pronounced at energies greater than the bandgap energy, which implies a shorter wavelength, a step increase was used to determine if there are any energy dependent effects. The step function assumed a constant value for the addition factor when the wavelength was less than or equal to a turn off wavelength, and zero elsewhere. Figure 4.2 depicts the model for a step increase at three wavelengths: 800, 860, and 900 nm.

## Theoretical Reflectance by Varying the Complex Index of Refraction

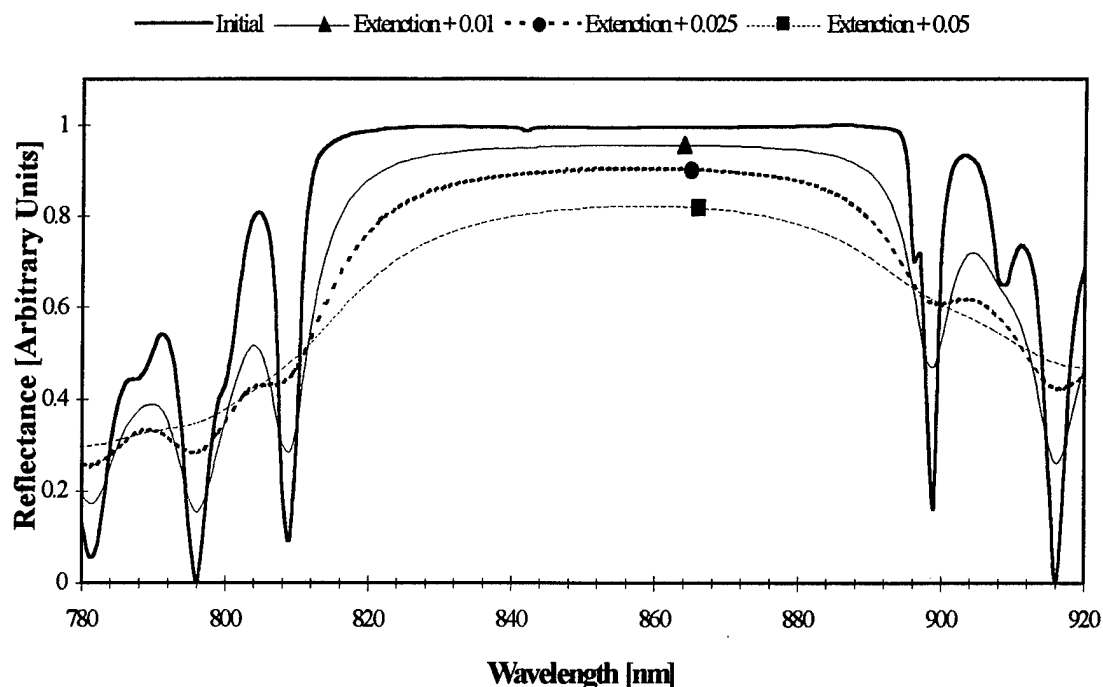


Figure 4.1: Theoretical Spectral Response by Varying the Extinction Coefficient Through Adding a Constant Over the Complete Wavelength Range

The same phenomena occurred in the step addition to the non-step when the figures are compared. The original curve is preserved at wavelengths greater than the step value, and compressed at wavelengths below the turn-off wavelength. The compressed curve is identical to the curve shown in Figure 4.1. This stands to reason, since the initial case (non-step addition) can be considered a step increase at an infinite wavelength.

The other mechanism modeled was the scattering of light in the structures. Instead of adding a change, a proportional factor multiplied the extinction coefficient. Figure 4.3 represents the same structure defined in the absorption model with a proportional increase



in the extinction coefficient. The reflectance curves follow the same general trend.

Shorter wavelengths appear to be effected more than the long wavelengths, and the curve is compressed. The compression is not as pronounced as before, and the peak reflectance does not drop as rapidly as it did in Figure 4.1.

### Theoretical Reflectance by Varying the Complex Index of Refraction

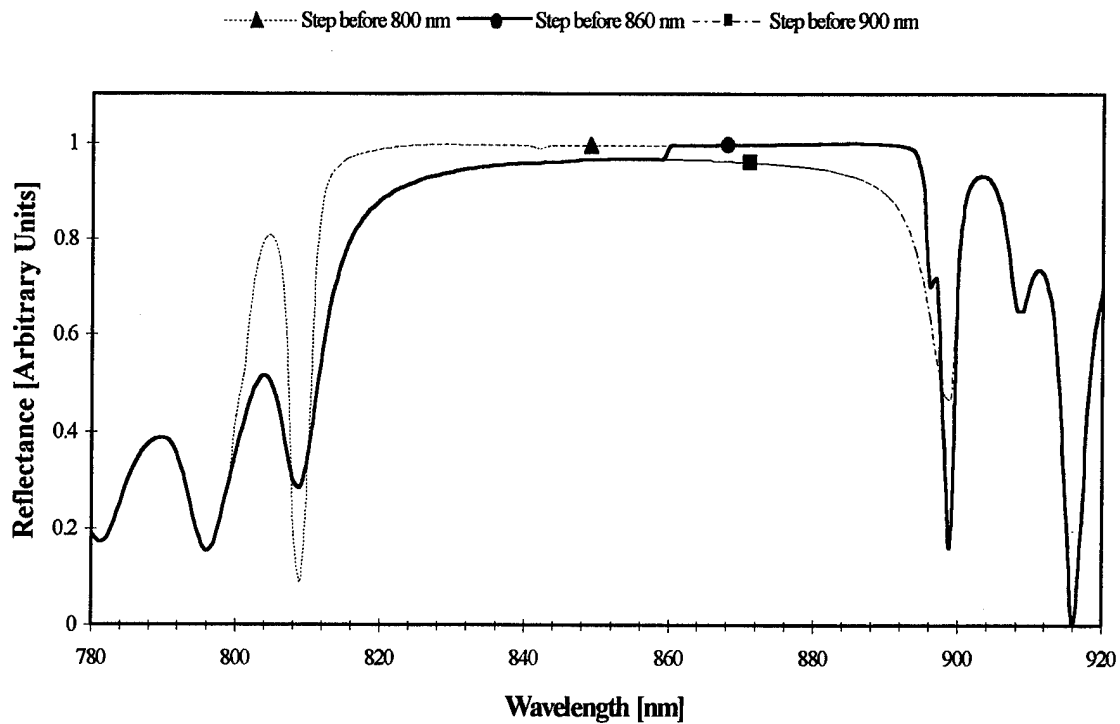


Figure 4.2: Theoretical Spectral Response by Varying the Extinction Coefficient Through Adding a Constant Over a Segment of the Wavelength Range

The Mathcad model predicts that there should be some decreases if the absorption and/or scattering increase. Experimental data was expected to show the same general trends of a decreasing peak reflectance and the compression of the curve. Thus the

reflectivity should be expected to increase and decrease depending on whether the additional absorption/scatterer is in a peak or valley.

### Theoretical Reflectance with Varying the Complex Index of Refraction

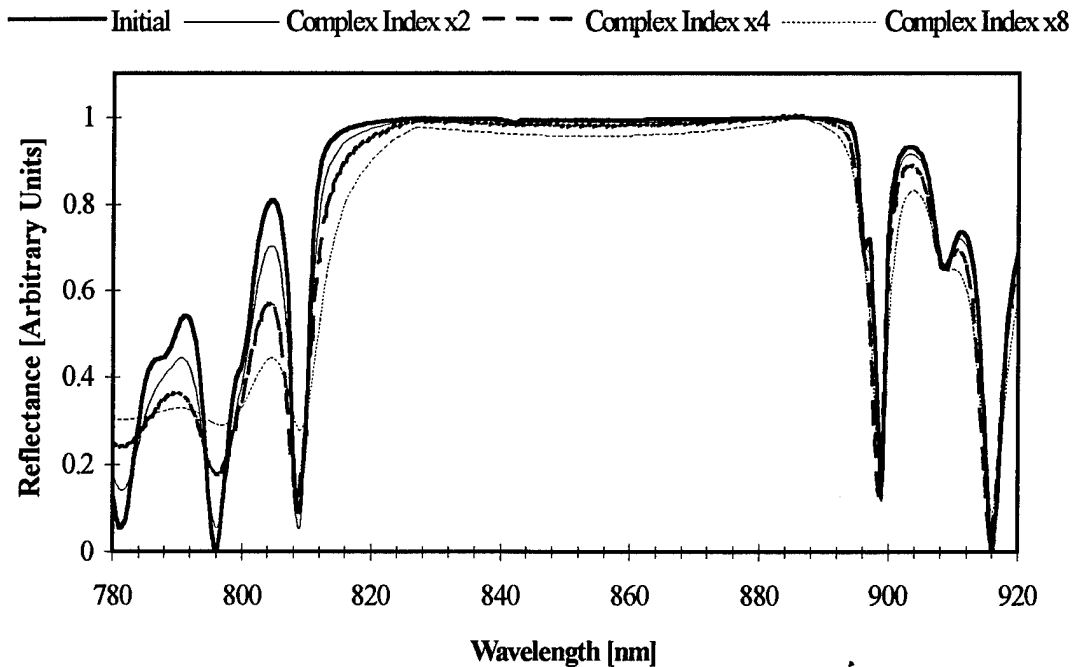


Figure 4.3: Theoretical Spectral Response with Varying Absorption Coefficients

#### 4.2 Relative Reflectivity Response

Each of the samples were characterized before and after each irradiation to verify the predicted behavior of the spectral response. Data collection procedures outlined in Chapter III were followed for all of the samples. It was the initial intention to use only the relative reflectance measurements, as shown in Figure 4.4, to determine the damage from

the neutron fluence. However, after the first three sample sets were run, the absolute reflectance measurements were added due to inconsistencies.

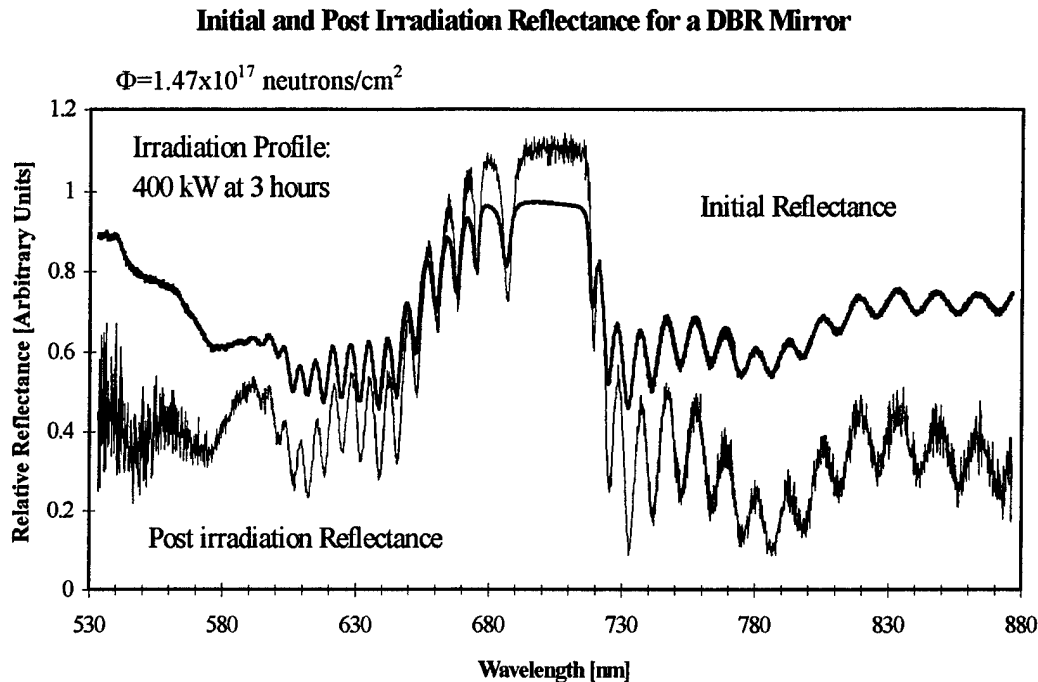


Figure 4.4. Initial Relative Reflectance After a 72,000 kW-min Irradiation

The initial response of the relative reflectance curves was baffling at first. Data from the same sample after an irradiation showed the new relative reflectance data was both below and above the initial reflectivity with distortions at the low wavelength region for multiple measurement locations on a single sample. Three questions initially came up that required answers.

- Was the measurement on the sample at the same location within the limits of experimental error?
- Did the neutron environment introduce enough heating to turn all or part of the DBR structure into an amorphous stack?
- Was there an instrument problem?

Repeatability was the first question addressed. Unirradiated samples from both the VCSEL and DBR mirror were measured, removed from the equipment platform, replaced, and measured again. The spectral responses overlaid each other with only a small amount of variance. Although, when the same samples were checked days later when the light had to be realigned and maximized from the translation stage to the OMA, there was a difference in the magnitude only. Several other measurements were performed to confirm the result. As a result, the relative spectral responses were used only to determine if there was any spectral shift or distortion as a result of neutron irradiation.

After the initial question of repeatability was addressed, the heating problem was tackled. A VCSEL and a DBR mirror sample were placed on a hot plate for the same duration that the irradiated samples saw after their initial reflectivity was determined. The hot plate was set for an upper temperature of 120 °C. This temperature represented the peak temperature that the samples would have seen during their irradiation (400 kW at 75 min). Again there was no spectral shift or distortion, only a change in magnitude (Figure 4.5). These results do not support the idea that the DBR structures changed due to heating when irradiated by neutrons.

The final question dealt with the equipment. There were three problems discovered with the experimental platform. First of all, the OMA was sensitive to the placement of the incident light upon its entrance slit. There appeared to be several “optimal” spots over the length of the entrance slit. When the turning mirrors did not change at all, the reflectance response was essentially identical. Unfortunately though, the optical bench was home to multiple users, and the turning mirrors were constantly

adjusted. The second problem was a result of a user programmed macro to save the data. A complete spectrum covered three separate data files centered at 600, 700, and 800 nm. After sample data was taken a background spectrum was subtracted from it; although, when the data was saved, the macro only kept the sample (non-background data). This introduced errors in the visible end of the reflectance curves leading to the faulty conclusion that there was a spectral distortion as in Figure 4.6.

#### Relative Reflectance for a DBR Mirror Control Sample

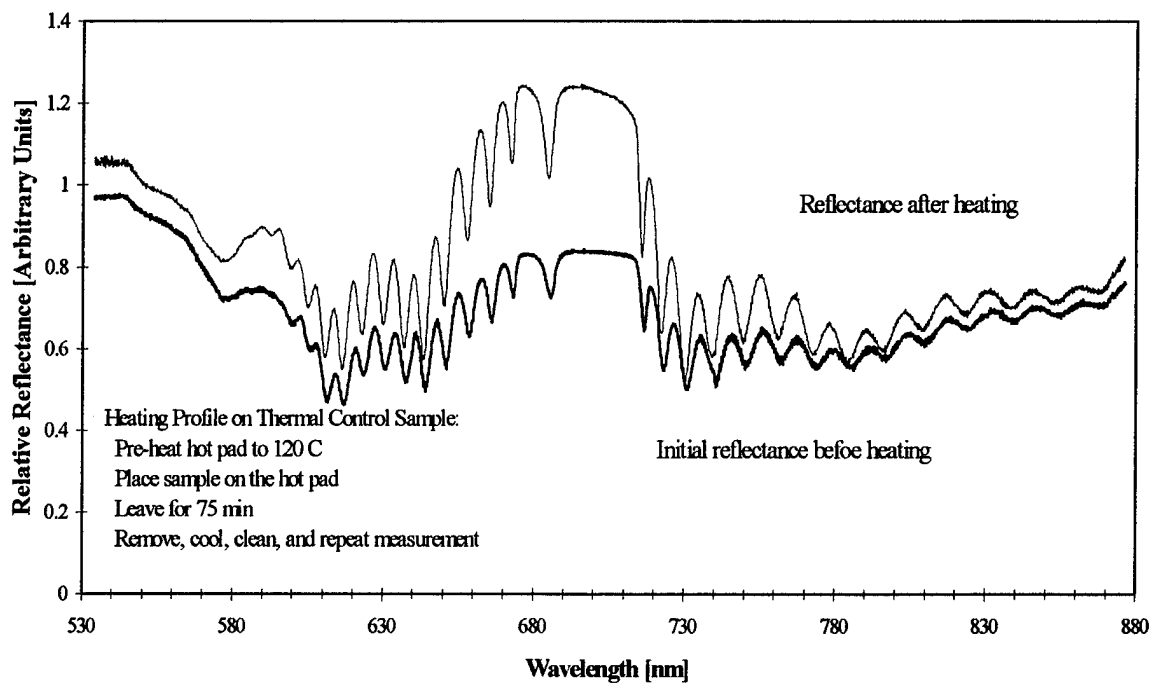


Figure 4.5. Control Sample Reflectance After a 75 Minute Bake at 120 °C

Attempts were made to factor-out the background, but due to the multiple variations within the spectral range, mainly in the visible region, this effort was abandoned. The macro was corrected for further data collection. Spectral response showed

reflectivities greater than one at times and sometimes on the order of three. The near-IR, high reflectance mirrors used as a reference should have bounded the response between zero and one. This deviation was due to the variation of the intensity of the white light source. The intensity wane was due to a failing bulb, so the source was reoptimized after a bulb replacement. This appeared to correct the large reflectances, and bounded the remaining reflectance spectrum between 0 and 1.2 (Figure 4.7).

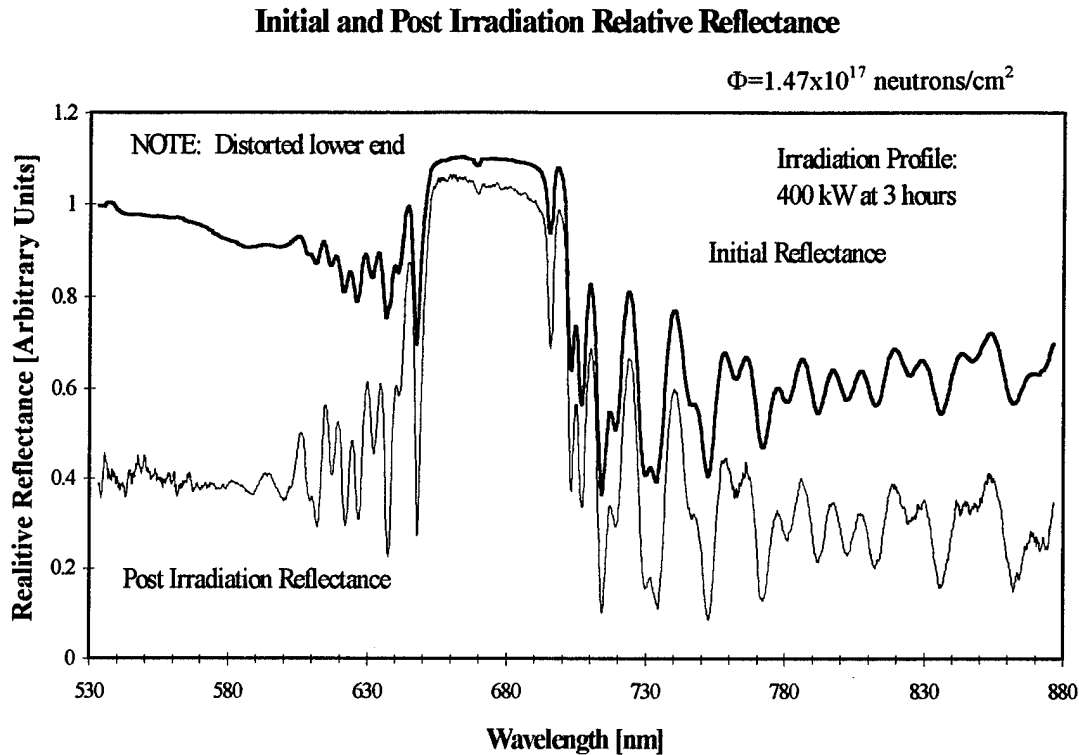


Figure 4.6 Relative Reflectance 72,000 kW-min with Apparent Spectral Distortion Caused When the Wrong Background Correction is Made

The relative measurements throughout the study were only used for determination of spectral shifts and distortions. This was due to the random nature of the relative

measurements to be higher, almost equal to, as well as lower when data was acquired post irradiation. The only concrete information from the relative curves was that there was not any distortion or shifting. Absolute measurements were relied on to determine the change in the magnitude of the reflectance for eleven different wavelengths.

#### Initial and Post Irradiation Reflectance for a DBR VCSEL

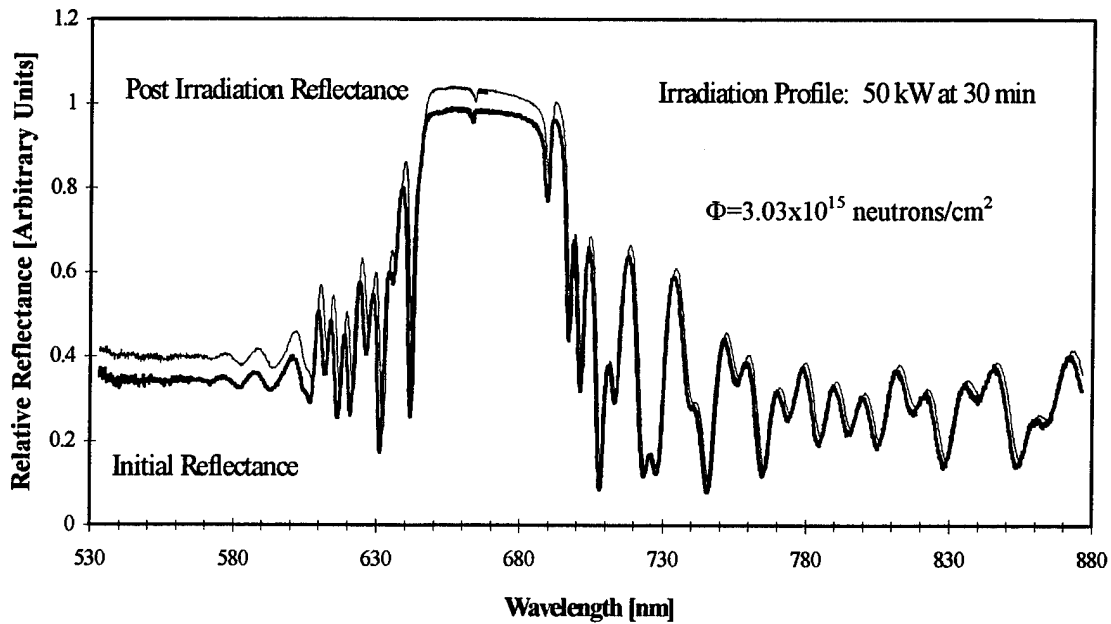


Figure 4.7 Relative Reflectance Measure for a 1500 kW-min Irradiation After White Light Equipment Repairs and Re-optimization

### 4.3 Absolute Reflectivity Response

The absolute reflectivity measurements performed on the last six sample sets provided the necessary data required to calculate a damage constant. A shift in the magnitude of the reflectance was easily obtained with the platform set-up. The sample's reflectivity was calculated from four measurements:  $I_o$ ,  $I_R$ ,  $I_T$ , and  $I_V$  (see Figure 4.8).

The sample reflectance was calculated from the expression  $I_V \equiv I_T \eta_{\text{lens}} R \eta_{\text{lens}} I_R / I_o$ .

Rearranging  $R = I_V I_o / (I_T I_R \eta_{\text{lens}}^2)$ . Where  $\eta_{\text{lens}}$  was experimentally determined as the transmission efficiency.

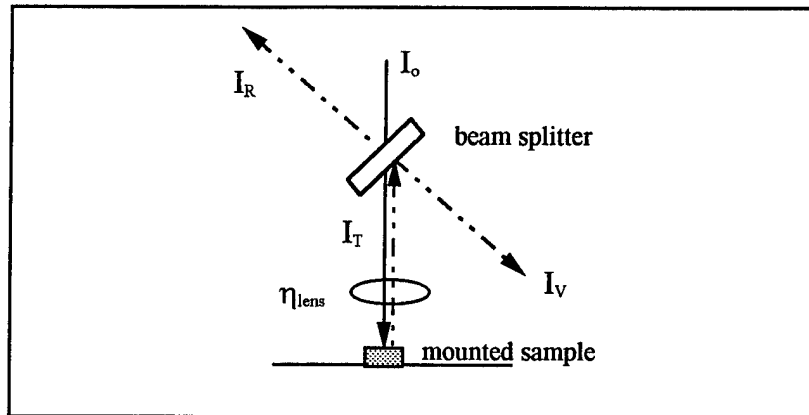


Figure 4.8. Absolute Reflectance Measurement

Eleven absolute reflectance measurements were taken from each sample. These measurements were within a wavelength range of 710-840 nm. Figure 4.9 is an expanded view of the longer wavelength relative reflectance spectrum of Figure 4.7. The measurement locations indicated on the graph are 710, 720, 730, 740, 750, 790, 800, 810, 820, 830, and 840 nm.

The initial and post irradiation calculated absolute reflectances showed the general trend of a decreasing reflectivity from the DBR structure. As long as the output from the Ti-sapphire was constant and the power meter was fixed at the correct beam height, the reflectance showed a decrease after an irradiation (see Figure 4.10). Several measurement sets did show an increase of reflectivity after an irradiation, but most of these values were



within the range that the control sample saw as well. Therefore, the increased reflectivity was not due to the irradiation, but due to the variation of the equipment.

#### Reflectance Region for Absolute Reflectance Measurements

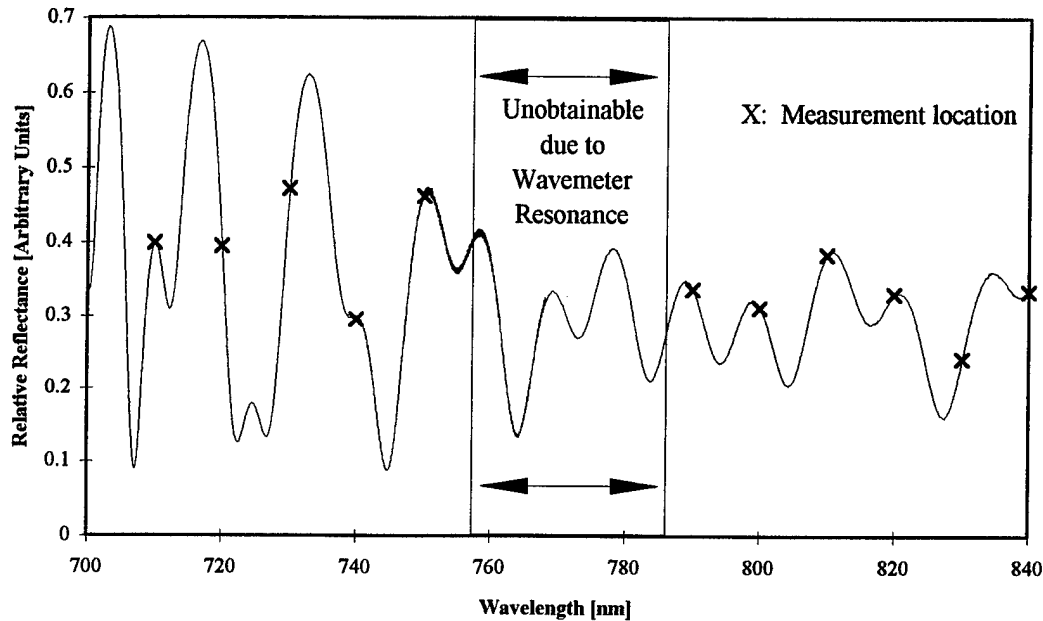


Figure 4.9. Absolute Reflectance Measurement Locations Overlaid onto a Relative Reflectance Spectrum

The results of absolute measurements for a DBR VCSEL sample is represented in Figure 4.10. Error bars on the absolute data represent the fluctuation of the powermeter. They are not true statistical errors associated with numerous measurements. The absolute data confirms that structures sustain damage from neutron bombardment that can reduce the bulk reflectance. The overlay (Figure 4.9) helps to visualize why some changes were larger than others. When the sampling point was on a feature that had a large slope, e.g., 720 nm, there was a large relative change in the absolute reflectance after irradiation. Additionally, when there was a small change, or no apparent change, e.g., 740 nm, the

data was from a region that did not change that rapidly. The most insightful data that could have been obtained would have been information in the high reflectance plateau. Unfortunately, this could not be performed due to equipment limitations. Absolute reflectance data did provide a feasible route to determine a damage constant.

### Initial and Post Absolute Reflectance for a DBR VCSEL

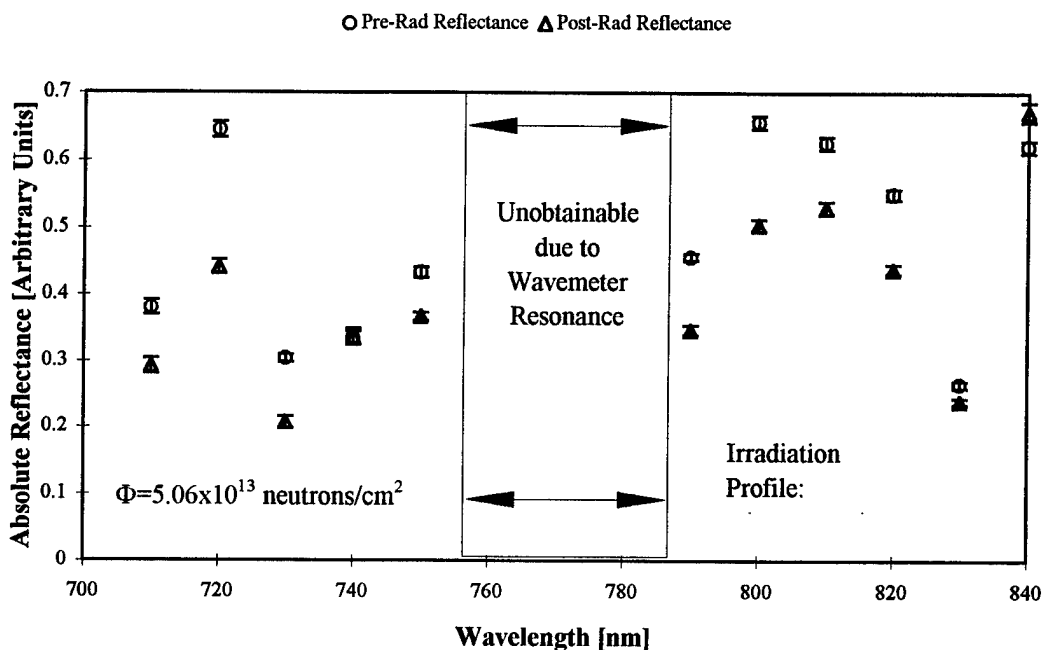


Figure 4.10. Absolute Reflectance Measurements for a 25 kW-min Irradiation of a DBR VCSEL

#### 4.4 Damage Constants

The process of determining a damage constant for a DBR structure started with a group average of the reflectance over the wavelength range for all of the pre-irradiation samples. An average reflectance was obtained first for each of the discrete wavelengths,

but also an overall average pre-irradiation reflectance. This allowed for verification of the Messenger-Spratt equation relationship. The same process of obtaining an average value for a given irradiation set was performed for the  $\Delta(1/\mathcal{R})$ . Thus, an inverse difference for the absolute reflectivity was found for each of the different fluence levels. Correlating the shift in the inverse reflectance versus fluence allowed a determination of the damage constant.

A Mathcad template was created to take the  $\Delta(1/\mathcal{R})$  and fluence data to find a damage constant that minimized the sum of the squares between the Messenger-Spratt type equation (equation 2.19) and the experimental data. Figures 4.11 and 4.13 are the inverse changes in reflectivity versus fluence for the VCSEL and DBR mirror along with the equation that minimized the error. Recall from equation 2.14 that  $\Delta(1/\mathcal{R}) = \Phi_n/K_{\mathcal{R}}$ . The y-axis of the two figures is a plot of the fitted  $K_{\mathcal{R}}$  to the experimental  $\Delta(1/\mathcal{R})$ . The full Messenger-Spratt relationship form for the two structures is depicted in Figures 4.12 and 4.14. This verifies the initial hypothesis of the  $\Delta(1/\mathcal{R})$  dependence.

The majority of the experimental data fit the curve within experimental uncertainty. A better fit to the data should result if there were more experimental data points to force a better curve fit through them. Presently, due to the experimental data, the mathematical search for  $K$  in the VCSEL (Figure 4.11) shows a better fit than does the DBR mirror (Figure 4.13). An argument can be made that these damage constants are within the correct order of magnitude, and they both do an adequate job of reproducing the characteristic “S” shaped curve through the data points (Figure 4.12 and 4.14). Additional data needs to be collected to obtain a more accurate damage constant.

### Search for Damage Constant by Sum of Squares.

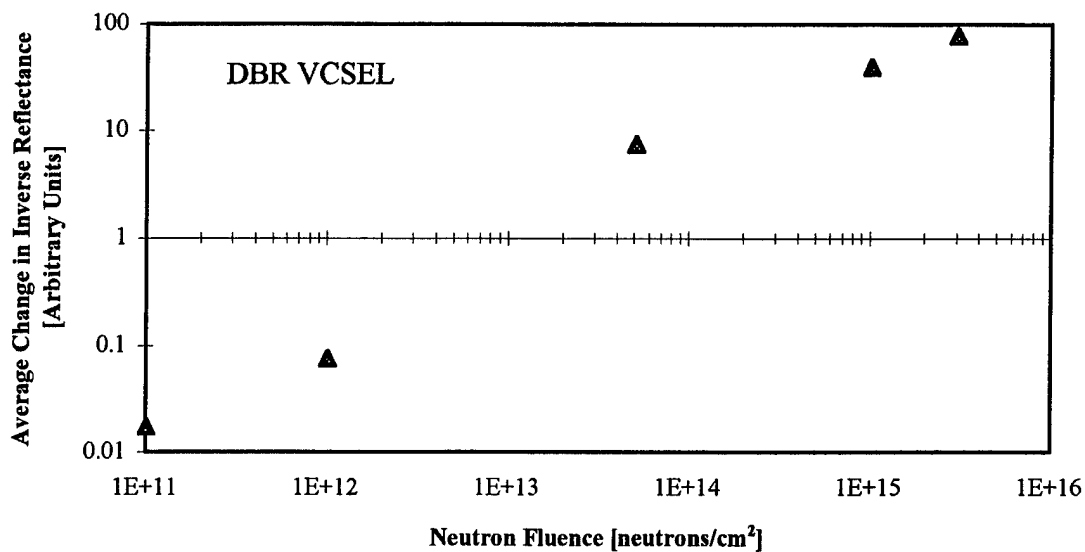


Figure 4.11. Determination of the Damage Constant for XC0911a, VCSEL Structure, by Minimizing the Sum of the Squares.

### Absolute Reflectance Damage for a DBR VCSEL

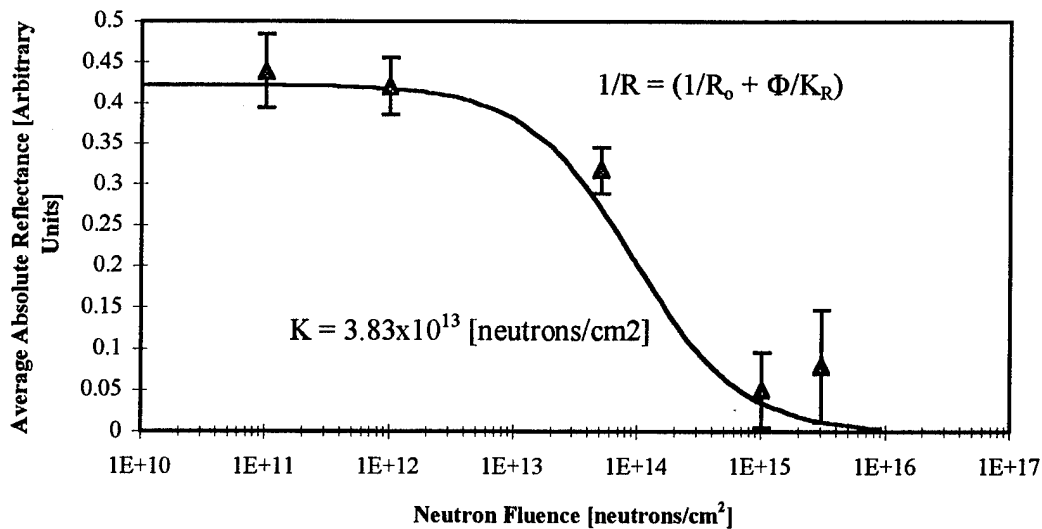


Figure 4.12. Messenger-Spratt Relationship for the VCSEL Reflectance

### Search for Damage Constant by Sum of Squares

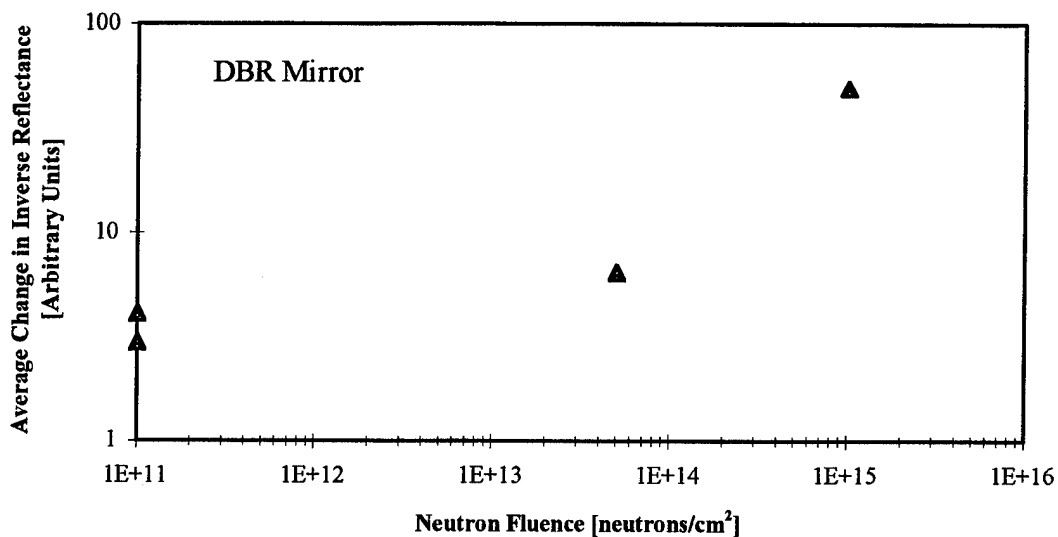


Figure 4.13. Determination of the Damage Constant for XC1118b, DBR Mirror, by Minimizing the Sum of the Squares.

### Absolute Reflectance Damage for DBR Mirror

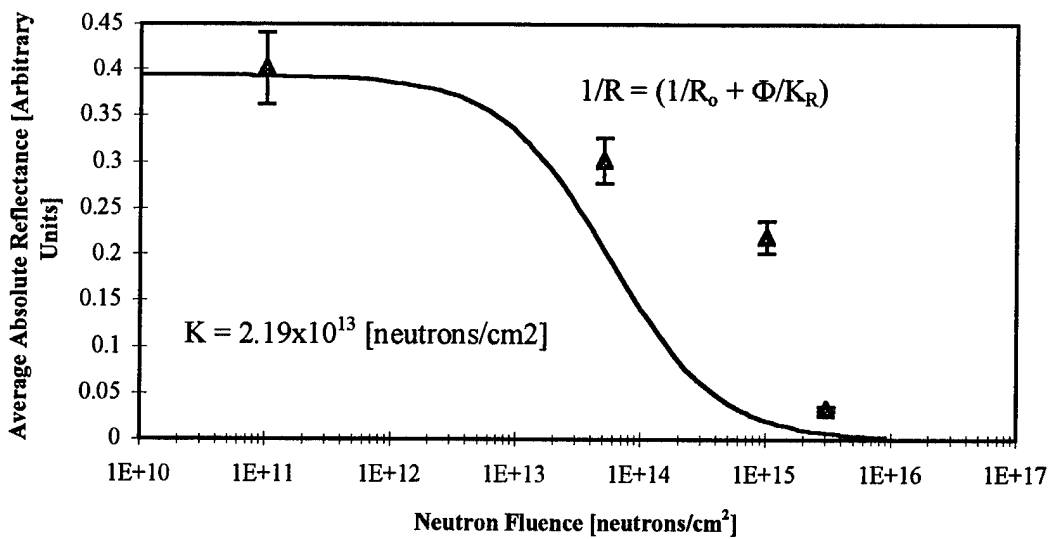


Figure 4.14. Messenger-Spratt Relationship for the DBR Mirror Reflectance

The damage constants for the two structures are given in Table 4.1. Within the table the maximum and minimum average reflectance for the structure is listed. The damage constant was minimized by iterating around a guessed value for  $K_{\mathfrak{R}}$ . A Mathcad program found the minimum value of  $K_{\mathfrak{R}}$  from the experimental data points and an average pre-irradiation reflectance. The  $K_{\mathfrak{R}}$  which is reported in Table 4.1, is the minimized constant with an average reflectance (pre-irradiation) from the 710-840 nm range.

Understanding that the entire reflectance spectrum should be bounded between one and zero, a damage constant was found by the model for the range of values with an initial average reflectance between one and zero. This was done to determine the sensitivity of the calculated damage constant to the initial assumption of the average bulk reflectance. After the damage constants were determined, the maximum deviation from the smallest to largest value of the fitted  $K_{\mathfrak{R}}$  was determined. These are reported in the Sensitivity over [1.0, 0.0] column of Table 4.1. These values show that the calculated damage constant varies by 15.7 percent and 22.6 percent over the entire reflectance range of zero to one for the DBR VCSEL and Mirror respectively. A similar calculation was performed using the maximum and minimum reflectances over the 710-840 nm range to determine the variance of the damage constant over the measured spectrum. This is reported in the [Max  $\mathfrak{R}$ , Min  $\mathfrak{R}$ ] column, and was found to be 2.1 percent and 7.1 percent for the DBR VCSEL and Mirror. Over the range of wavelengths used for the absolute measurement, the damage constants were fairly constant.

Table 4.1: VCSEL and DBR Mirror Damage Constants Over the Spectral Range.

Structure	$K_{\mathcal{R}}$ [neutrons/cm <sup>2</sup> ]	Maximum $\mathcal{R}$	Minimum $\mathcal{R}$	Sensitivity over [1.0, 0.0]	Sensitivity over [Max $\mathcal{R}$ , Min $\mathcal{R}$ ]
DBR VCSEL	$3.83 \times 10^{13}$	0.5488	0.2707	15.65	2.13
DBR Mirror	$2.19 \times 10^{13}$	0.5309	0.2187	22.55	7.12

These calculations show that the damage constants are fairly constant over the range, and can be applied to the full spectrum. The structure's response to neutrons did not vary much over the measured spectrum, 2.1% and 7.1% for the DBR VCSEL and Mirror respectively. Noting that these are not perfect, a general response to the entire spectrum (530-880 nm) should not be off more than 15.6% and 22.6% for the DBR VCSEL and Mirror respectively.

The calculated damage constants are of the correct magnitude to other damage constants quoted in the literature. Summers et. al. [20] give a listing of 1 MeV equivalent (Si) damage constants for some bipolar transistors, while Barnes [8] gives damage constants for GaAs laser diodes. The reported damage constants are the reciprocal of the damage constant found in this study and represent damage constants represent gain degradation for the transistors and a reduction in light intensity for the laser diodes. Summers et. al and Barnes report  $K_n$  and  $\tau_{no}K_n$  respectively in their articles with units of [cm<sup>2</sup>]. In order to compare the damage constants Table 4.2 below presents the reciprocal of the constants presented by Summers et. al. and Barnes.

These damage constants from a 1 MeV equivalent (Si) neutron fluence can be used to predict further damage constants by protons, electrons, helium atoms, etc... NIEL

allows for the linear relationship between the various particles. Figure 4.15 is a log-log plot of the two damage constants found in this study with extrapolations to electrons and protons. The NIEL values are taken from Summers et.al. [12] for GaAs, and were not calculated as described in section 2.3. It is assumed that these NIEL values are suitable for the two DBR sample outlined in section 3.1. There are two sub-scales on the graph for the proton and electron energy. By knowing the particle energy, a damage constant can be picked off of one off the linear lines. The proton energy scale runs up five decades from 0.001 MeV to 100 MeV. Electron energy runs approximately three decades starting at 0.3 MeV and continuing to 100 MeV in decade increments starting at 1 MeV.

Table 4.2. Damage Constants for Bipolar Transistors and GaAs Laser Diodes

Device:	Bipolar Transistors	Damage Constant [cm <sup>-2</sup> ]
	2N2222A (Ic = 30 mA)	2.51x10 <sup>16</sup>
	2N2907A (Ic = 30 mA)	2.06x10 <sup>15</sup>
	2N3055 (Ic = 1 A)	1.00x10 <sup>15</sup>
	2N6678 (Ic = 5 A)	1.06x10 <sup>14</sup>
	2N6547 (Ic = 3 A)	3.55x10 <sup>13</sup>
Device:	GaAs Laser Diode	Damage Constant [cm <sup>-2</sup> ]
	RCA p-type diodes	1.41x10 <sup>14</sup>
	RCA p-type diodes	2.33x10 <sup>14</sup>



### Damage Constant versus NIEL

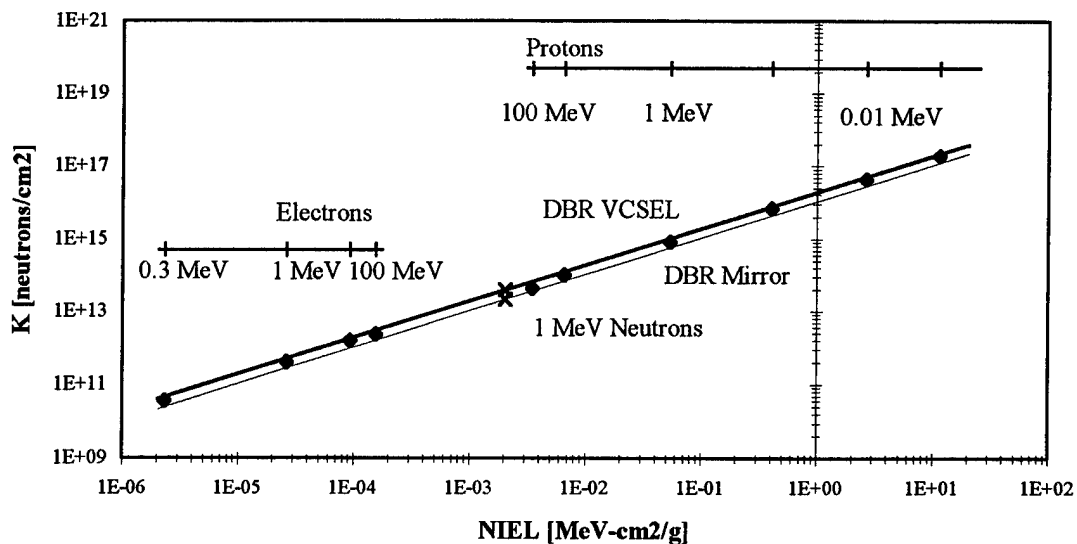


Figure 4.15. Linear Relationship Between Equivalent Damage for Neutrons, Protons, and Electrons [12]

#### 4.5 Electrically Pumped VCSELs

The effect of neutron irradiation on fully functional, electrically pumped VCSELs was performed along with the reflectivity study. These electrically pumped VCSELs were characterized for their I-V, L-I (light intensity versus current), and spectral output initially and after irradiation. Each sample set of these VCSELs did manifest damage. There was a change in the slope efficiency upon lasing, if it did lase, the necessary current to achieve lasing was increased upon post irradiation examination, and the light output was reduced. These phenomena were seen on all of the samples.

There were a limited amount of samples that could be cleaved from the initial wafer. As a result not every sample had the same size aperture devices on them. The

devices were laid with 5, 10, 20, 30, 40, and 50  $\mu\text{m}$  apertures. Unfortunately, not all of the samples made it back from the reactor for a post irradiation analysis. Therefore, a damage constant for the above parameters could not be determined due to missing data. There were general trends that tracked for all of the samples with various apertures.

The most interesting data from the electrically pumped VCSELs was the change in the L-I curves between their initial and post irradiation behavior. Each of the lasers behaved a little differently upon reaching threshold after irradiation due to mode hopping, but their sub-threshold data was very consistent. Figure 4.16 represents the response of 50  $\mu\text{m}$  devices upon irradiation. The slope of the sub-threshold lines decrease as well as experience a shift to higher currents with increasing exposure to neutron fluences. This trend appears to fit to all of the fluences except for the  $3.03 \times 10^{15}$  data. The sub-threshold L-I curve has shown improvement from the previous fluence of  $1.01 \times 10^{15}$ . This phenomena has not been explained, and needs to be repeated for confirmation and further study.

The I-V and spectral data changed in a similar matter, although there was not as much confidence in this data as in the L-I data. It was determined that the current driver did not provide a steady current. A digital multimeter was installed in series with the device to obtain a more accurate reading. The trends appear to be similar, although no real confidence can be counted on at the present time. This uncertainty is reflected in irradiation samples as well as control sample data. Similar devices on the same sample showed different conflicting results in the shift of the threshold and slope efficiency both

for irradiation and control samples. The variation appears to be a result of the uncertainty in the actual current delivered to the sample from the driver.

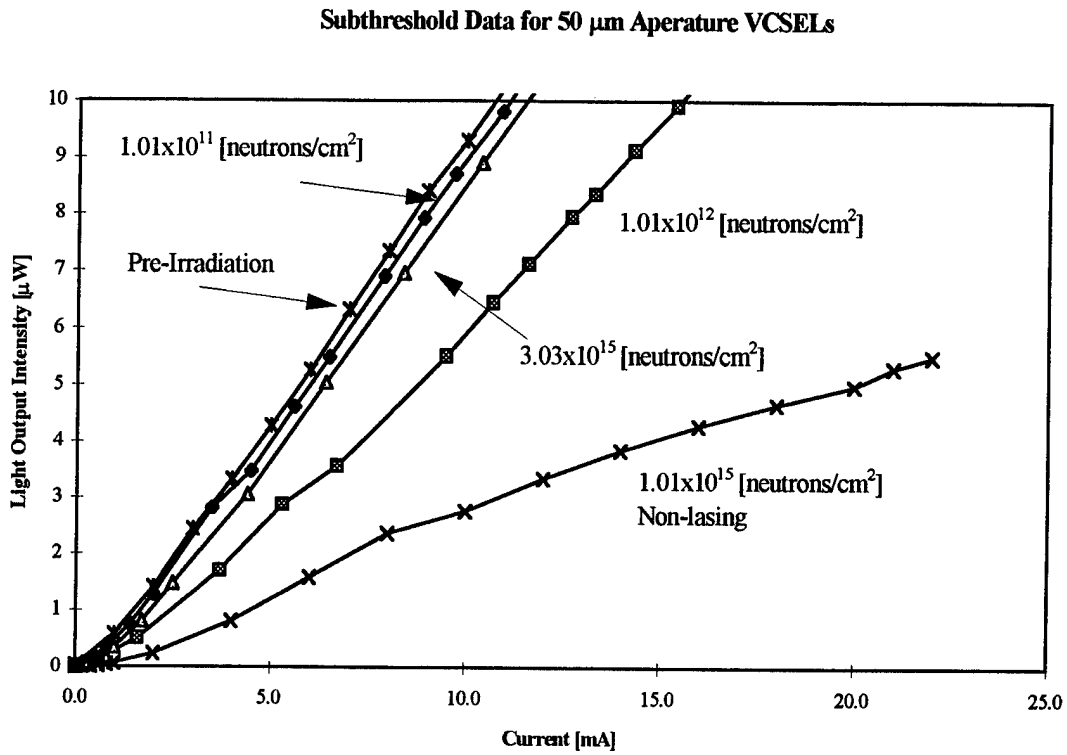


Figure 4.16: Subthreshold L-I data for 50  $\mu\text{m}$  Aperture Electrically Pumped VCSELs.

## V. Conclusions and Recommendations

The goal of this project was to determine a damage constant and predict the damage mechanism that DBRs experience upon neutron irradiation. Accomplishing these goals required an initial investigation of what the structure's response should be due to an interaction with a neutron spectrum. The response was determined through a design tool for RCLEDs along with an activation calculations to determine what level of radiation protection should be considered. These theoretical tools were tried and tested with experimental data. Twelve sample sets were sent to Ohio State University's 500 kW Research Reactor for irradiation at various time and power profiles. The overall test matrix produced samples that acquired sufficient damage to plot the displacement damage, manifested as a decrease in the bulk reflectivity, versus a 1 MeV equivalent (Si) neutron fluence. A damage constant was obtained from this data, which can be applied to predict further device degradation and act as an input for future designs. Some specific results to the DBR structures are worth noting.

- Spectral response to neutral particle bombardment is not affected by either a lateral shift or in shape distortion
- Reflectivity of DBRs will degrade as a result of displacement damage resulting in a structure that has more absorptive losses.

These conclusions were determined for only the DBR mirror and VCSEL (XC1118b and XC0911a samples). The VCSEL sample was not operated through optical pumping for initial and post irradiation behavior. The relative magnitude of the DBR damage to other damage mechanisms could not be evaluated with these two samples. This is not important for the DBR mirror. Solid state DBR mirrors that are employed in

space will experience a bulk reflectivity decrease as the exposure to neutrons increases. This is true for the VCSELs due to all of the other processes involved. Additional samples need to be tested that allow initial and final device characterization to a neutron fluence. Device parameters for the electrically pumped VCSELs were characterized except for their bulk reflectivities.

There was interesting data on the electrically pumped VCSELs that showed a general trend of a decrease in light output and an increase in current threshold with decreasing slope efficiencies. This data is not as strong as the reflectivity data, due to equipment problems. Further investigation on these devices is warranted to tie the overall effectiveness of the DBR degradation to other factors such as the reduction in the minority carrier lifetime.

Additional testing should be carried out on the same devices to better define the damage curve and constant. These follow-on tests will be able to show the relative magnitude of DBR damage to changes within the device. Optically and electrically pumped VCSELs should be tested for their initial reflectance as well as device operation both before and after neutron irradiation at a range of fluences. Other samples should be used that could be tested by deep level transient spectroscopy to determine characteristics of the defects caused by displacement damage.

Further work should be pursued by having samples that only differ by the addition of active regions. An example would be identically grown samples, one a DBR mirror and the other a DBR-quantum well device. If the device can be electrically and/or optically

activated, then a better correlation to the individual effects as well as device compounded effects can be distinguished. Specifically:

- Use a DBR mirror for a measure of stack damage
- Use an optically pumped VCSEL with the same structure and material as the DBR mirror. Measure the bulk reflectance by both absolute and relative means. Determine the laser's performance through viewing the spectrum for the FWHM and lasing wavelength ( $\lambda_0$ ), as well as taking a measure of the ratio of the input pump beam to output of the device's beam. Perform all of these measurements both initially and after irradiation.
- Use an electrically pumped VCSEL with the same structure and material as the DBR mirror and optically pumped VCSEL. Measure the bulk reflectance by absolute and relative means. Determine initial and post irradiation behavior through I-V, L-I, and spectral data (FWHM and  $\lambda_0$ ). From the data calculate a slope efficiency upon lasing.
- Fill in enough samples to be able to characterize a well definable curve for damage relationships. This includes enough data points to pin down the knee of the curve as well as the slope, hence damage constant, in the transition region.

Performing this work will provide the knowledge of how damage emanating the DBR will effect the entire device. If the DBR's are the weak link of a device, then more work can go into perfecting a more resilient stack. Otherwise, if the device will experience deleterious damage decades before the DBR stack, then the work can shift to improving the device. This appears to be an area that will lead to many significant discoveries in the field of photonics and radiation effects in ensuring that DBR and microcavity devices have sustained operations in a harsh environment.

## Bibliography

1. S. M. Sze, Physics of Semiconductor Devices, 2nd Ed., J. Wiley & Sons, New York, 1976.
2. E. Hect, Optics, 2nd Ed., Addison Wesley Publishing Company, Massachusetts, 1987.
3. J. T. Verdeyen, Laser Electronics, Prentice-Hall Inc, New Jersey, 1989.
4. G.C. Messenger, and M.S. Ash, The Effects of Radiation on Electronic Systems, 2nd Ed., Van Nostrand Reinhold, New York, 1992.
5. G.P. Summers, E.A. burke, M.A. Xapsos, C.J. Dale, P.W. Marshall, and E.L. Petersen, "Displacement Damage in GaAs Structures," *IEEE Trans. in Nucl. Sci.*, vol. 35, pp. 1221-1226, 1988.
6. J.H. Crawford, and J.W. Cleland, "Nature of Bombardment damage and Energy Levels in Semiconductors," *J. Appl. Phys.*, vol. 30(8), pp. 1204-1213, 1959.
7. L.W. Aukerman, P.W. Davis, R.D. Graft, and T.S. Shilliday, "Radiation Effects in GaAs," *J. Appl. Phys.*, vol 34(12), pp. 3590-3599, 1963.
8. C.E. Barns, "Neutron damage in Epitaxial GaAs Laser Diodes," *J. Appl. Phys.*, vol 42(5), pp. 1941-1949, 1971.
9. C. Barns, d. Heflinger, and R. Reel, "Effect of neutron irradiation on laser diode properties," *Proc. of SPIE*, vol. 1174, pp 233-261, 1989.
10. R.F. Carson, and W.W. Chow, "Neutron Effects in High-Power GaAs Laser Diodes," *IEEE Trans. in Nuc. Sci.*, vol. 36(6), pp. 2076-2082, 1989.
11. P.J. Griffin, J.G. Kelly, T.F. Luera, A.L. Barry, and M.S. Lazo, "Neutron Damage Equivalence in GaAs," *IEEE Trans, in Nuc. Sci.*, Vol 38(6), pp. 1216-1224, 1991.
12. G.P. Summers, E.A. Burke, P. Shapiro, S.R. Messenger, and R.J. Walters, "Damage Correlations in Semiconductors Exposed to Gamma, Electron, and Proton Radiations," *IEEE Trans. in Nuc. Sci.*, vol 40(6), pp. 1372-1379, 1993.
13. D.E. Aspnes, S.M. Kelso, R.A. Logan, and R. Bhat, "Optical Properties of  $Al_xGa_{1-x}As$ ," *J. Appl. Phys.*, vol 60(2), pp. 754-767, 1986.
14. S. Adachi, "GaAs, AlAs, and  $Al_xGa_{1-x}As$ : Material parameters for use in research and device applications," *J. Appl. Phys.*, vol 58(3), pp. R1-R29, 1985.

15. D.W. Jenkins, "Optical constants of  $\text{Al}_x\text{Ga}_{1-x}\text{As}$ ," *J. Appl. Phys.*, vol 68(4), pp. 1848-1853, 1990.
16. D.W. Jenkins, "Erratum: Optical constants of  $\text{Al}_x\text{Ga}_{1-x}\text{As}$  [J. Appl. Phys. 68, 1848 (1990)]," *J. Appl. Phys.*, vol 72(7), p 3223, 1992.
17. E.E. Conrad, "Considerations in Establishing a Standard for Neutron Displacement Energy Effects in Semiconductors," *IEEE Trans. on Nuc. Sci.*, vol 18(6), pp 200-205, 1971.
18. B.R. Gossick, "Disordered Regions in Semiconductors Bombarded by Fast Neutrons," *J. Appl. Phys.*, vol 30(8), pp. 1214-1218, 1959.
19. H. Lischka, H. Henschel, O. Kön, W. Lennartz, and H.U. Schmidt, "Radiation Effects in Light Emitting Diodes, Laser diodes, Photodiodes, and Optocouplers," Proc. of the 2nd European Conference on Radiation and Its Effects on Components and Systems, pp. 226-231, Sep 13-16, Saint-Milo, France, 1993.
20. G.P. Summers, E.A. Burke, C.J. Dale, E.A. Wolicki, P.W. Marshall, and M.A. Gehlhausen, "Correlation of Particle-Induced Displacement Damage in Silicon," *IEEE Trans. in Nucl. Sci.*, vol 34, pp. 1134-1139, 1989.
21. ASTM, "Characterizing Neutron Energy Fluence Spectra in Terms of an Equivalent Monoenergetic Neutron Fluence for Radiation-Hardness Testing of Electronics," E-722-85, pp. 463-469, 1985.
22. R.J. Iwanowski, B.J. Kowalski, J. Bak-Misiuk, and B.A. Orlowski, "Optical reflectivity studies of radiation-induced trace disorder in silicon," *Applied Surface Sci.*, vol 70/71, pp. 318-321, 1993.
23. R.J. Bagnell, Design and Characterization of Optically Pumped Vertical Cavity Surface Emitting Lasers, MS thesis, Air Force Institute of Technology (AU), Wright-Patterson AFB, OH, December 1992.
24. T.M Fitzgerald, Design and Characterization of Resonant Cavity Light-Emitting Diodes, MS thesis, Air Force Institute of Technology (AU), Wright-Patterson AFB, OH, December 1994.
25. T.E Walsh, Effects of Neutron Radiation on Aluminum-Gallium-Arsenide Lasers, MS thesis, Air Force Institute of Technology (AU), Wright-Patterson AFB, OH, December 1978.
26. J.L. Duderstadt and L.J. Hamilton, Nuclear Reactor Analysis, J. Wiley & Sons, New York, 1976.



27. Erdtmann, G. , Neutron Activation Tables, Kernchemie in Einzeldarstellungen, Vol 6, Weinheim: Verlag Chemie, 1976.
28. J.C. Leclerc and A. Cornu, Neutron Activation Analysis Tables, University of Microfilms International, Ann Arbor, 1995.
29. C.J. Dale, P.W. Marshall, E.A. Burke, G.P. Summers, and E.A. Wolick, "High Energy Electron Induced Displacement Damage in Si," *IEEE. Trans. in Nucl. Sci.*, NS-35, vol 34, pp. 1208-1214, 1988.
30. H.A. MacLeod, Thin Film Optical Filters, 2nd Edition, Macmillan Publishing Co., NY, 1986.

## Appendix A: Mathcad Program to Estimate Activity of Irradiated Samples

This document estimates the activity that a solid state device composed of Ga, Si, As, In, and P will have after an exposure to a neutron fluence for a given time. The activity will account for ingrowth and decay of the products. The essential inputs are the number densities found in the first section. All of the decay constants and cross sections were taken from Erdtmann.

### Section 1: Problem Set-up of Number densities

Total number of atoms per element present in sample, i.e. number density times volume

$$N_C := 6.105564 \cdot 10^{11} \quad N_{Ga} := 9.167282 \cdot 10^{19} \quad N_P := 1.467282 \cdot 10^{15}$$

$$N_{Si} := 8.140752 \cdot 10^{12} \quad N_{As} := 9.170194 \cdot 10^{19}$$

$$N_{Al} := 8.059433 \cdot 10^{15} \quad N_{In} := 7.336408 \cdot 10^{14}$$

### Section 1.1: Decay constants after a neutron absorption

Decay constants in decays per second for each of the isotopes for the above elements

$$\lambda_{C14} := 3.829238 \cdot 10^{-12} \quad \lambda_{As76} := 7.320946 \cdot 10^{-6} \quad \lambda_{In116g} := 4.881318 \cdot 10^{-2}$$

$$\lambda_{Si31} := 7.348889 \cdot 10^{-5} \quad \lambda_{In114m2} := 15.75335 \quad \lambda_{P32} := 5.618023 \cdot 10^7$$

$$\lambda_{Al28} := 7.348889 \cdot 10^{-5} \quad \lambda_{In114m1} := 1.620387 \cdot 10^{-7}$$

$$\lambda_{Ga70} := 5.475096 \cdot 10^{-4} \quad \lambda_{In114g} := 9.640434 \cdot 10^{-3}$$

$$\lambda_{Ga72m} := 25.67212 \quad \lambda_{In116m2} := 0.3150669$$

$$\lambda_{Ga72g} := 1.365538 \cdot 10^{-5} \quad \lambda_{In116m1} := 2.131449 \cdot 10^{-4}$$

### Section 2: Cross Sections

#### Section 2.1: Thermal Cross Sections

Thermal cross sections for reaction in barns for each of the above isotopes:

$$\sigma_{C13} := 9 \cdot 10^{-28} \quad \sigma_{As75} := 4.3 \cdot 10^{-24} \quad \sigma_{In115g} := 4.5 \cdot 10^{-23}$$

$$\sigma_{Si30} := 1.07 \cdot 10^{-25} \quad \sigma_{In113m2} := 3.1 \cdot 10^{-24} \quad \sigma_{P31} := 1.8 \cdot 10^{-25}$$

Thermal cross sections continued:

$$\begin{aligned} \sigma_{Al27} &:= 2.32 \cdot 10^{-25} & \sigma_{In113m1} &:= 4.4 \cdot 10^{-24} \\ \sigma_{Ga69} &:= 1.68 \cdot 10^{-24} & \sigma_{In113g} &:= 3.9 \cdot 10^{-24} \\ \sigma_{Ga71m} &:= 1.5 \cdot 10^{-25} & \sigma_{In115m2} &:= 9.2 \cdot 10^{-23} \\ \sigma_{Ga71g} &:= 4.71 \cdot 10^{-24} & \sigma_{In115m1} &:= 6.5 \cdot 10^{-23} \\ \sigma_{Ga71} &:= \sigma_{Ga71m} + \sigma_{Ga71g} \\ \sigma_{In113\_1} &:= \sigma_{In113m2} + \sigma_{In113m1} & \sigma_{In115\_1} &:= \sigma_{In115m2} + \sigma_{In115m1} \end{aligned}$$

## Section 2.2: Epi-Thermal Cross Sections

Epi-Thermal cross sections for reaction in barns for each of the above isotopes:

$$\begin{aligned} I_{C13} &:= 1.3 \cdot 10^{-27} & I_{As75} &:= 4.1 \cdot 10^{-24} & I_{In115g} &:= 6 \cdot 10^{-22} \\ I_{Si30} &:= 6.6 \cdot 10^{-25} & I_{In113m2} &:= 0 & I_{P31} &:= 8 \cdot 10^{-26} \\ I_{Al27} &:= 2.45 \cdot 10^{-25} & I_{In113m1} &:= 2.58 \cdot 10^{-22} \\ I_{Ga69} &:= 1.17 \cdot 10^{-23} & I_{In113g} &:= 2.82 \cdot 10^{-21} \\ I_{Ga71m} &:= 0 & I_{In115m2} &:= 9.2 \cdot 10^{-23} \\ I_{Ga71g} &:= 3.12 \cdot 10^{-23} & I_{In115m1} &:= 2.7 \cdot 10^{-21} \\ I_{Ga71} &:= I_{Ga71m} + I_{Ga71g} \\ I_{In113\_1} &:= I_{In113m2} + I_{In113m1} & I_{In115\_1} &:= 2.114 \cdot 10^{-21} \end{aligned}$$

Natural abundance for the following isotopes and branching ratios as needed:

$a_{C13} := 0.011$	$a_{As75} := 1.0$	$BR_{In113m2} := 1$	$BR_{In115g} := 1$
$a_{Si30} := 0.031$	$a_{In113} := 0.043$	$BR_{In113m1} := 0.965$	$BR_{Ga71m} := 1$
$a_{Al27} := 1.0$	$a_{In115} := 0.957$	$BR_{In113g} := 1$	$BR_{Ga71g} := 1$
$a_{Ga69} := 0.6011$	$a_{P31} := 1.0$	$BR_{In115m2} := 1$	
$a_{Ga71} := 0.3989$		$BR_{In115m1} := 1$	

### Section 3: Neutron Beam Time

Initial data for the irradiation:

$t_{sd} := 1.08 \cdot 10^4$  time after zero when the beam is shut down in seconds  
(presently at a 3-Hour beam time)

Activity at time of shut down

The ingrowth and decay equation are of the following form:  $A(\text{time}, \text{flux}, \text{region})$ . The region is a Boolean flag that allows Mathcad to switch the thermal cross section ( $R=1$ ) to epi-thermal cross section ( $R=2$ ).

Activity equations for the VCSEL (bulk, mirrors, and QWs)

$$A_{C14}(t, \phi, R) := \text{if} \left[ R=1, \phi \cdot N_C \cdot a_{C13} \cdot \sigma_{C13} \cdot \left( 1 - e^{-\lambda_{C14} t} \right), \phi \cdot N_C \cdot a_{C13} \cdot I_{C13} \cdot \left( 1 - e^{-\lambda_{C14} t} \right) \right]$$

$$A_{Si31}(t, \phi, R) := \text{if} \left[ R=1, \phi \cdot N_{Si} \cdot a_{Si30} \cdot \sigma_{Si30} \cdot \left( 1 - e^{-\lambda_{Si31} t} \right), \phi \cdot N_{Si} \cdot a_{Si30} \cdot I_{Si30} \cdot \left( 1 - e^{-\lambda_{Si31} t} \right) \right]$$

$$A_{Al28}(t, \phi, R) := \text{if} \left[ R=1, \phi \cdot N_{Al} \cdot a_{Al27} \cdot \sigma_{Al27} \cdot \left( 1 - e^{-\lambda_{Al28} t} \right), \phi \cdot N_{Al} \cdot a_{Al27} \cdot I_{Al27} \cdot \left( 1 - e^{-\lambda_{Al28} t} \right) \right]$$

$$A_{Ga70}(t, \phi, R) := \text{if} \left[ R=1, \phi \cdot N_{Ga} \cdot a_{Ga69} \cdot \sigma_{Ga69} \cdot \left( 1 - e^{-\lambda_{Ga70} t} \right), \phi \cdot N_{Ga} \cdot a_{Ga69} \cdot I_{Ga69} \cdot \left( 1 - e^{-\lambda_{Ga70} t} \right) \right]$$

$$A_{Ga72}(t, \phi, R) := \text{if} \left[ R=1, \phi \cdot N_{Ga} \cdot a_{Ga71} \cdot \sigma_{Ga71} \cdot \left( 1 - e^{-\lambda_{Ga72g} t} \right), \phi \cdot N_{Ga} \cdot a_{Ga71} \cdot I_{Ga71} \cdot \left( 1 - e^{-\lambda_{Ga72g} t} \right) \right]$$

$$A_{As76}(t, \phi, R) := \text{if} \left[ R=1, \phi \cdot N_{As} \cdot a_{As75} \cdot \sigma_{As75} \cdot \left( 1 - e^{-\lambda_{As76} t} \right), \phi \cdot N_{As} \cdot a_{As75} \cdot I_{As75} \cdot \left( 1 - e^{-\lambda_{As76} t} \right) \right]$$

Activity equations for the VCSEL (bulk, mirrors, and QWs) continued

$$\text{Thermal}_{\text{In114}_1}(t, \phi) := \phi \cdot N_{\text{In}} \cdot \text{BR}_{\text{In113m1}} \cdot a_{\text{In113}} \cdot \sigma_{\text{In113}_1} \cdot \left(1 - e^{-\lambda_{\text{In114m1}} \cdot t}\right)$$

$$\text{Epi}_{\text{In114}_1}(t, \phi) := \phi \cdot N_{\text{In}} \cdot \text{BR}_{\text{In113m1}} \cdot a_{\text{In113}} \cdot I_{\text{In113}_1} \cdot \left(1 - e^{-\lambda_{\text{In114m1}} \cdot t}\right)$$

$$A_{\text{In114}_1}(t, \phi, R) := \text{if}(R=1, \text{Thermal}_{\text{In114}_1}(t, \phi), \text{Epi}_{\text{In114}_1}(t, \phi))$$

$$\text{Thermal}_{\text{In114}_2}(t, \phi) := \phi \cdot N_{\text{In}} \cdot a_{\text{In113}} \cdot \sigma_{\text{In113g}} \cdot \left(1 - e^{-\lambda_{\text{In114g}} \cdot t}\right)$$

$$\text{Epi}_{\text{In114}_2}(t, \phi) := \phi \cdot N_{\text{In}} \cdot a_{\text{In113}} \cdot I_{\text{In113g}} \cdot \left(1 - e^{-\lambda_{\text{In114g}} \cdot t}\right)$$

$$A_{\text{In114}_2}(t, \phi, R) := \text{if}(R=1, \text{Thermal}_{\text{In114}_2}(t, \phi), \text{Epi}_{\text{In114}_2}(t, \phi))$$

$$\text{Thermal}_{\text{In116}_1}(t, \phi) := \phi \cdot N_{\text{In}} \cdot a_{\text{In115}} \cdot \sigma_{\text{In115}_1} \cdot \left(1 - e^{-\lambda_{\text{In116m1}} \cdot t}\right)$$

$$\text{Epi}_{\text{In116}_1}(t, \phi) := \phi \cdot N_{\text{In}} \cdot a_{\text{In115}} \cdot I_{\text{In115}_1} \cdot \left(1 - e^{-\lambda_{\text{In116m1}} \cdot t}\right)$$

$$A_{\text{In116}_1}(t, \phi, R) := \text{if}(R=1, \text{Thermal}_{\text{In116}_1}(t, \phi), \text{Epi}_{\text{In116}_1}(t, \phi))$$

$$\text{Thermal}_{\text{In116}_2}(t, \phi) := \phi \cdot N_{\text{In}} \cdot a_{\text{In115}} \cdot \sigma_{\text{In115g}} \cdot \left(1 - e^{-\lambda_{\text{In116g}} \cdot t}\right)$$

$$\text{Epi}_{\text{In116}_2}(t, \phi) := \phi \cdot N_{\text{In}} \cdot a_{\text{In115}} \cdot I_{\text{In115g}} \cdot \left(1 - e^{-\lambda_{\text{In116g}} \cdot t}\right)$$

$$A_{\text{In116}_2}(t, \phi, R) := \text{if}(R=1, \text{Thermal}_{\text{In116}_2}(t, \phi), \text{Epi}_{\text{In116}_2}(t, \phi))$$

$$A_{\text{P32}}(t, \phi, R) := \text{if}\left[R=1, \phi \cdot N_{\text{P}} \cdot a_{\text{P31}} \cdot \sigma_{\text{P31}} \cdot \left(1 - e^{-\lambda_{\text{P32}} \cdot t}\right), \phi \cdot N_{\text{P}} \cdot a_{\text{P31}} \cdot I_{\text{P31}} \cdot \left(1 - e^{-\lambda_{\text{P32}} \cdot t}\right)\right]$$

Assigning either ingrowth or decay for the isotopes from initial time ( $t=0$ ), to the time of the beam shut down ( $t_{sd}$ ), and then allowing for exponential decay.

Ingrowth and decay equation assignment for the VCSEL:

$$\begin{aligned}
 A_{C14}(t, \phi, R) &:= \text{if} \left[ t < t_{sd}, A_{C14}(t, \phi, R), A_{C14}(t_{sd}, \phi, R) \cdot e^{-\lambda_{C14} \cdot (t - t_{sd})} \right] \\
 A_{Si31}(t, \phi, R) &:= \text{if} \left[ t < t_{sd}, A_{Si31}(t, \phi, R), A_{Si31}(t_{sd}, \phi, R) \cdot e^{-\lambda_{Si31} \cdot (t - t_{sd})} \right] \\
 A_{Al28}(t, \phi, R) &:= \text{if} \left[ t < t_{sd}, A_{Al28}(t, \phi, R), A_{Al28}(t_{sd}, \phi, R) \cdot e^{-\lambda_{Al28} \cdot (t - t_{sd})} \right] \\
 A_{Ga70}(t, \phi, R) &:= \text{if} \left[ t < t_{sd}, A_{Ga70}(t, \phi, R), A_{Ga70}(t_{sd}, \phi, R) \cdot e^{-\lambda_{Ga70} \cdot (t - t_{sd})} \right] \\
 A_{Ga72}(t, \phi, R) &:= \text{if} \left[ t < t_{sd}, A_{Ga72}(t, \phi, R), A_{Ga72}(t_{sd}, \phi, R) \cdot e^{-\lambda_{Ga72g} \cdot (t - t_{sd})} \right] \\
 A_{As76}(t, \phi, R) &:= \text{if} \left[ t < t_{sd}, A_{As76}(t, \phi, R), A_{As76}(t_{sd}, \phi, R) \cdot e^{-\lambda_{As76} \cdot (t - t_{sd})} \right] \\
 A_{In114\_1}(t, \phi, R) &:= \text{if} \left[ t < t_{sd}, A_{In114\_1}(t, \phi, R), A_{In114\_1}(t_{sd}, \phi, R) \cdot e^{-\lambda_{In114m1} \cdot (t - t_{sd})} \right] \\
 A_{In114\_2}(t, \phi, R) &:= \text{if} \left[ t < t_{sd}, A_{In114\_2}(t, \phi, R), A_{In114\_2}(t_{sd}, \phi, R) \cdot e^{-\lambda_{In114g} \cdot (t - t_{sd})} \right] \\
 A_{In116}(t, \phi, R) &:= \text{if} \left[ t < t_{sd}, A_{In116\_1}(t, \phi, R), A_{In116\_1}(t_{sd}, \phi, R) \cdot e^{-\lambda_{In116m1} \cdot (t - t_{sd})} \right] \\
 A_{In116\_2}(t, \phi, R) &:= \text{if} \left[ t < t_{sd}, A_{In116\_2}(t, \phi, R), A_{In116\_2}(t_{sd}, \phi, R) \cdot e^{-\lambda_{In116g} \cdot (t - t_{sd})} \right] \\
 A_{P32}(t, \phi, R) &:= \text{if} \left[ t < t_{sd}, A_{P32}(t, \phi, R), A_{P32}(t_{sd}, \phi, R) \cdot e^{-\lambda_{P32} \cdot (t - t_{sd})} \right]
 \end{aligned}$$

Total Activity of the entire sample [mCi]:

$$A_{\text{total}}(t, \phi, R) := \left[ \begin{aligned}
 &A_{C14}(t, \phi, R) + A_{Si31}(t, \phi, R) + A_{Al28}(t, \phi, R) + A_{Ga70}(t, \phi, R) \dots \\
 &+ A_{Ga72}(t, \phi, R) + A_{As76}(t, \phi, R) + A_{In114\_1}(t, \phi, R) + A_{In114\_2}(t, \phi, R) \dots \\
 &+ A_{In116\_1}(t, \phi, R) + A_{In116\_2}(t, \phi, R) + A_{P32}(t, \phi, R)
 \end{aligned} \right] \cdot \frac{1}{3.7 \cdot 10^7}$$

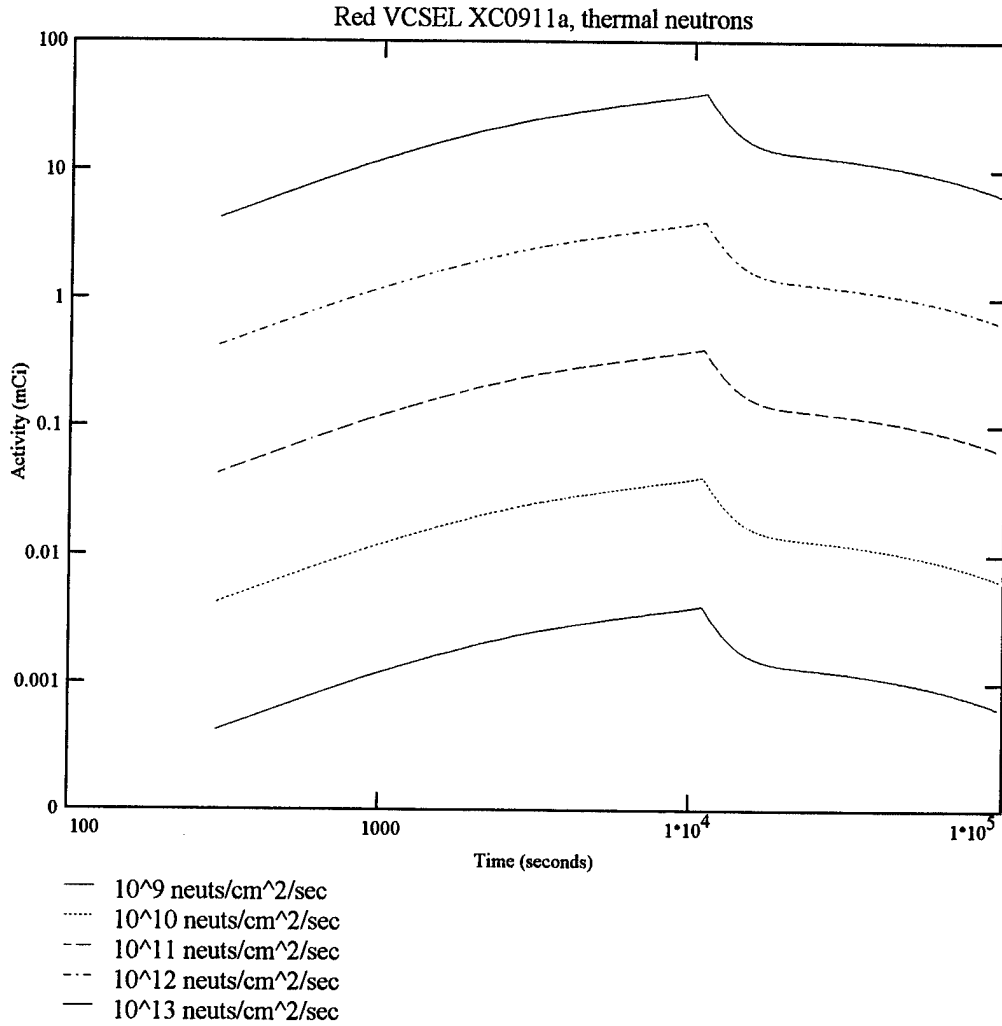
Data on the time of interest and the flux levels for the sample irradiation.

$t := 300, 600 \dots 9.72 \cdot 10^4$  Time will run from essentially zero to 1 day after a 3 hour beam time

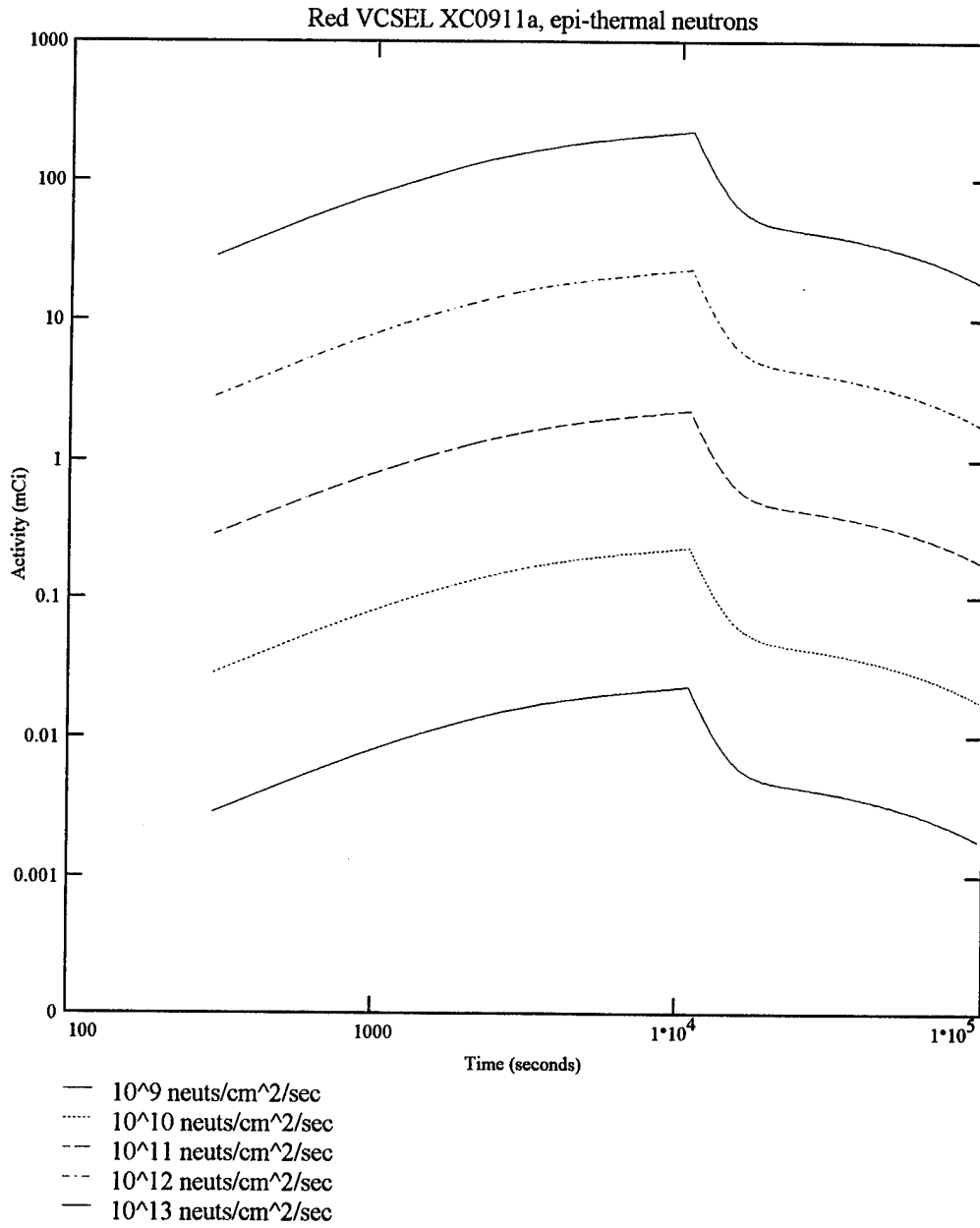
$i := 1 \dots 5$

$\phi_i := 1 \cdot 10^{8+i}$  Flux levels of  $10^9$  to  $10^{13}$  neutrons per  $\text{cm}^2$  per sec

Activity (in mCi) for sample XC0911a for five different irradiation times, assuming thermal cross sections. Decay time reflects 1 day after a 3 hr beam.



Activity (in mCi) for sample XC0911a for five different irradiation times, assuming epi-thermal cross sections. Decay time reflects 1 day after a 3 hr beam.

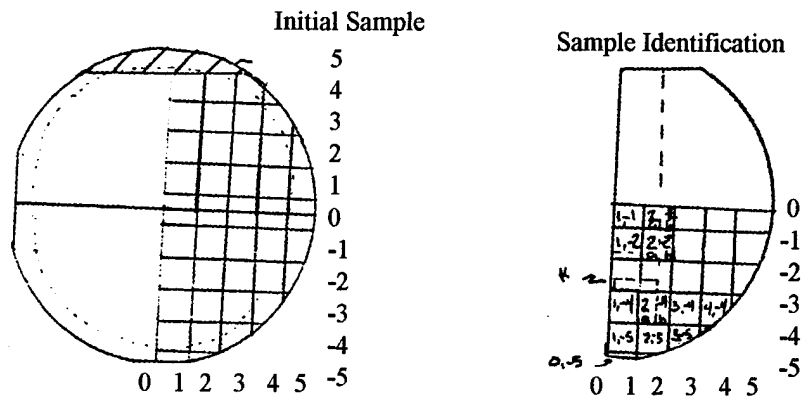




## Appendix B: Wafer Diagrams for Reflectivity Study

The two diagrams represent the initial DBR VCSEL (XC0911a) and mirror (XC1118b) as well as the sub divided and cleaved samples. The sample identification numbers result from their cartesian like grid. An (x,y) pair represents the lower right corner of each of the samples. In order to keep the orientation of the original wafer to the cleaved sample, a permanent mark was made on the backside of the upper left hand corner.

### XC0911a: VCSEL Structure

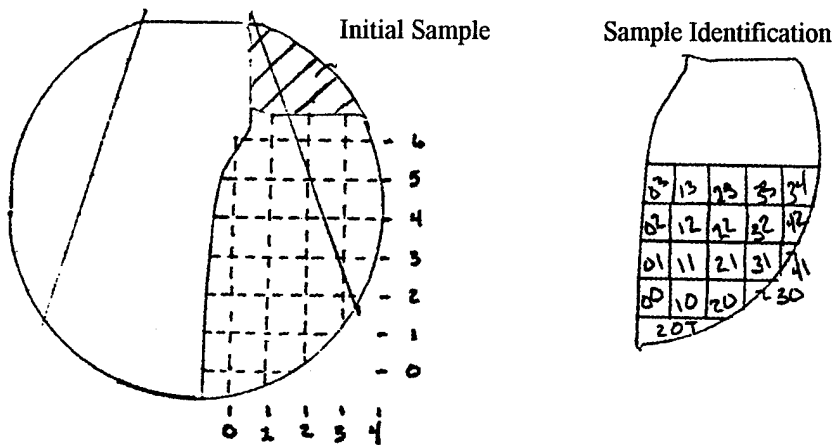


Sample was spun while grown. The dashed circle represents the edge of the growth.

\*  
1, -3

a	b
1	2

### XC1118b: DBR Mirror



Linear gradient to sample growth. Angular lines represent the edge of the growth.

## Appendix C: Equipment List

The equipment needed in order to perform the necessary experimental measurements is listed below.

<u>Equipment Type</u>	<u>Description</u>
Optical Multi Channel Analyzer (OMA)	Silicon diode array that allows a real-time observation of the spectrum sent into the entrance slit.  Manufacturer: EG&G, Model 1471A
DC Power Supply	Controllable power supply to drive the white light source  Manufacturer: KEPCO, ATE 100-10M
Digital Multimeter	Measuring current and voltages throughout the experimental setup.  Manufacturer: Fluke, 77/AN
Translation Stage	Two to three axis control for sample positioning.  Manufacturer: New-Focus and Line Tool Company
Precision Pulsed Current Source	Provide a constant DC current at a given duty cycle. Used to electrically pump the VCSELs  Manufacturer: ILX Lightwave, LDP-3811
Tunable Ti-Sapphire Laser	Tunable laser that allowed for absolute reflectivity measurements.  Manufacturer: Spectra Physics, Model 3900S
Argon Ion Laser	Pump laser needed to excite the Ti-Sapphire to lase  Manufacturer: Spectra Physics, Model 2020-03
Water Chiller	Keeps the lasing medium cool to enhance operational performance.  Manufacturer: NESLAB, Model RTE-111

<u>Equipment Type</u>	<u>Description</u>
Wavemeter	Calibrated meter that determines the wavelength incident light upon its entrance slit.  Manufacturer: Burleigh, Wavemeter WA-10
Video Camera	Allowed for imaging of samples onto a video screen  Manufacturer: COHU, 181502100/ALTS
Powermeter	Calibrated meter and interchangeable detector heads to register the power of incident light.  Manufacturer: Fieldmaster, Coherent FM FE12
Microscope	Magnification of samples for closer viewing  Manufacturer: Bausch and Lomb
Miscellaneous Optics	Neutral Density Filters  Near IR High reflectance Mirrors  Beam Splitters  Lenses  Gaseous Nitrogen
Sodium Iodide detector and multi-channel analyzer	Computerized data acquisition system to allow for counting of gamma spectra from activated materials
Beta/Gamma Detectors	Dose meters to determine a quantitative measurement for the activity of the exposed samples before working with them
Paraffin wax	Beta-Gamma shielding to reduce the amount of incident radiation upon personnel

## Appendix D: Radioactive Material Handling Procedure

All of the radioactive material that came from the reactor at Ohio State had to first be surveyed by the base Radiation Safety Officer. Under the Air Force Institute of Technology's material licensee, 34-30154-1AFP, in accordance with the timely renewal notice, radioactive samples could be accepted from OSU. The samples were hand carried from OSU to Wright-Patterson AFB to minimize rough handling as well as allowing for a first hand account of the sample activity before receipt. Upon arrival to WPAFB the samples were checked in with the Base Radiation Safety Office. An initial survey was performed to catalogue the radiation dose for each of the samples. The samples could only be used after the Radiation Safety released them. Every precaution of time, distance, and shielding were used to keep with the concept of ALARA (as low as reasonably achievable).

The Radiation Safety Officer will be aware of all motion and use of the radioactive material from arrival on WPAFB to the disposal after the most significant peak energy has decayed to approximately 10 half lives. When the sample is no longer distinguishable above background, the sample will proceed with its normal disposal route. The samples are expected to remain classified as radioactive until the  $^{76}\text{As}$  decays through ten half lives at approximately 11 days ( $T_{1/2} = 26.3 \text{ hr}$ ).

The optical measurements were not performed in the same area where the samples were stored. As a result, when the samples were checked out of the hot cell, an initial dose reading was taken. This radiation dose was displayed so that everyone working in the same environment was aware of the active samples. Any potential dose to personnel

was reduced through shielding the active samples when not in direct use. Once a set of measurements was completed, the samples were transported back to the hot cell for storage until the next measurement set.

Each sample was treated as a radioactive sample until told otherwise from the Base Radiation Safety Office. That meant that contact was minimized. There was no direct handling of the samples, or movement as long as it was not necessary.

The table below represents the activation products and their associated energies for beta and gamma decay. These are the by-products of the irradiation that we need to minimize until they have essentially decayed to a level equal to or below that of background. There are two main isotopes of concern out of the list:  $^{76}\text{As}$  and  $^{72}\text{Ga}$ . Gallium and arsenic are the two main constituent elements for all of the semiconductor materials that were under test.  $^{14}\text{C}$ ,  $^{32}\text{P}$ ,  $^{114\text{m}}\text{In}$ , and  $^{198}\text{Au}$  have long half-lives, and might appear to be the main concern; although, these elements are present in small quantities.

Upon an initial radiation survey after irradiation, the beta-gamma spectroscopy was dominated by  $^{76}\text{As}$  and  $^{72}\text{Ga}$ . These isotopes were all that the detectors saw. After the sample had enough time to allow for most of the short and intermediate lived isotopes, the detector was able to recognize the weak signature of  $^{114\text{m}}\text{In}$ . Normally at this point the total activity of the sample was under  $0.01\ \mu\text{Ci}$ , and very close to background radiation. The main concern for the potential shelf life of the samples is due entirely to the  $^{76}\text{As}$  and  $^{72}\text{Ga}$ .

Activated Isotopes of Concern

Isotope	Parent	Half Life	$\beta$ energies (%) [KeV]	$\gamma$ energies (%) [KeV]
C-14	C-13	5736 yrs	157.0 (max)	No gammas
Al-28	Al-27	2.246 m	2850 (max)	1778.8 (100)
Si-30	Si-29	2.62 h	4420 (max)	511 (200), 1266.2 (1.1)
P-32	P-31	14.28 d	1709 (max)	No gammas
Ga-70	Ga-69	21.1 m	1650 (max)	1039.3 (0.5), 176.2 (0.16)
Ga-72	Ga-71	14.1 h	3150 (max) 3150 (8), 2520 (9), 1510 (10), 960 (31), 640 (42)	601(8), 630 (27), 835 (96), 894 (10), 1050 (7), 1465 (3.5), 1600 (5), 1860 (5), 2201 (26), 2500 (20)
As-76	As-76	26.3 h	2970 (50), 2410 (31), 1760 (16), 360 (3)	559 (43), 657 (6), 1220 (5), 1789 (0.3), 2100 (0.9)
In-114	In-113	71.9 s	1984 $\beta^-$ , 400 (0.039) $\beta^+$	1299.9 (0.20)
In-114m	In-113	49.51 d	164, 188 via $e^-$	192 (17), 558 (3.5), 724 (3.5)
In-116	In-115	14.2 s	3300 (max)	434 (0.12), 950 (0.10), 1293 (1.2)
In-116m	In-116	54.2 m	1000 (51), 870 (28), 600 (21) 138, 160 via $e^-$	164, 138 (3), 417 (36), 819 (17), 1090 (53), 1293 (80), 1508 (11), 2111 (20)
Au-198	Au-197	2.695 d	962(max)	411.8(95.5)

## Appendix E: Mathcad Program to Determine the Reflectivity Damage Constant

I. The purpose of this program is to take a data file composed of the equivalent neutron fluence and the change in the reflectivity ( $\Delta 1/R$ ) to mathematically determine the damage constant.

Data file containing fluence  
and change in reflectance.

Data := READPRN(rvcse1)

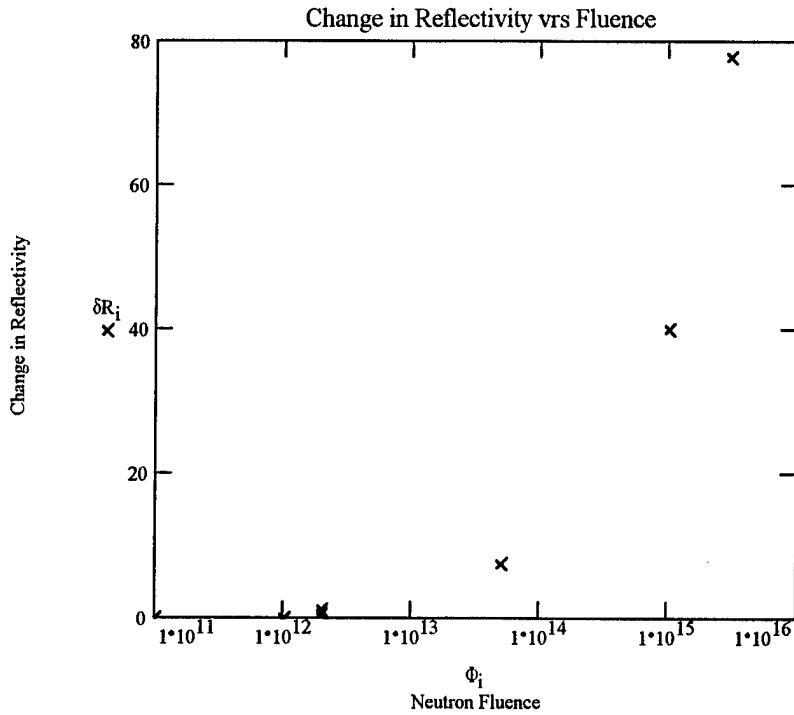
Notation:  $\Delta R$  implies  $\Delta$  one over  $R$

$i := 0..rows(Data) - 1$

$\Delta R_i := Data_{i,1}$

$\Phi_i := Data_{i,0}$

	Change in Absolute Reflectivity	Neutron Fluence
$Data = \begin{bmatrix} 1.0115396086 \cdot 10^{11} & 0.017327 \\ 1.01153961 \cdot 10^{12} & 0.075949 \\ 2.02307922 \cdot 10^{12} & 1.088389 \\ 2.02307922 \cdot 10^{12} & 0.603635 \\ 5.057698043 \cdot 10^{13} & 7.501225 \\ 1.01153961 \cdot 10^{15} & 40.05183 \\ 3.03461883 \cdot 10^{15} & 77.72884 \end{bmatrix}$	$\Delta R = \begin{bmatrix} 0.017327 \\ 0.075949 \\ 1.088389 \\ 0.603635 \\ 7.501225 \\ 40.05183 \\ 77.72884 \end{bmatrix}$	$\Phi = \begin{bmatrix} 1.0115396086 \cdot 10^{11} \\ 1.01153961 \cdot 10^{12} \\ 2.02307922 \cdot 10^{12} \\ 2.02307922 \cdot 10^{12} \\ 5.057698043 \cdot 10^{13} \\ 1.01153961 \cdot 10^{15} \\ 3.03461883 \cdot 10^{15} \end{bmatrix}$



Equation for the Neutron Damage:

$$R(\Phi, K) := \left( \frac{1}{R_0} + \frac{\Phi}{K} \right)^{-1}$$

Average initial reflectivity

$$R_0 := 0.421953$$

Sum of Squares to be minimized

$$SSE(K) := \sum_i \left( \delta R_i - \frac{1}{R(\Phi_i, K)} \right)^2$$

Guess

$$K := 1.15 \cdot 10^{12}$$

Given

$$SSE(K) = 0$$

$$K_{fit} := \text{minerr}(K)$$

$$K_{fit} = 3.831416687 \cdot 10^{13}$$

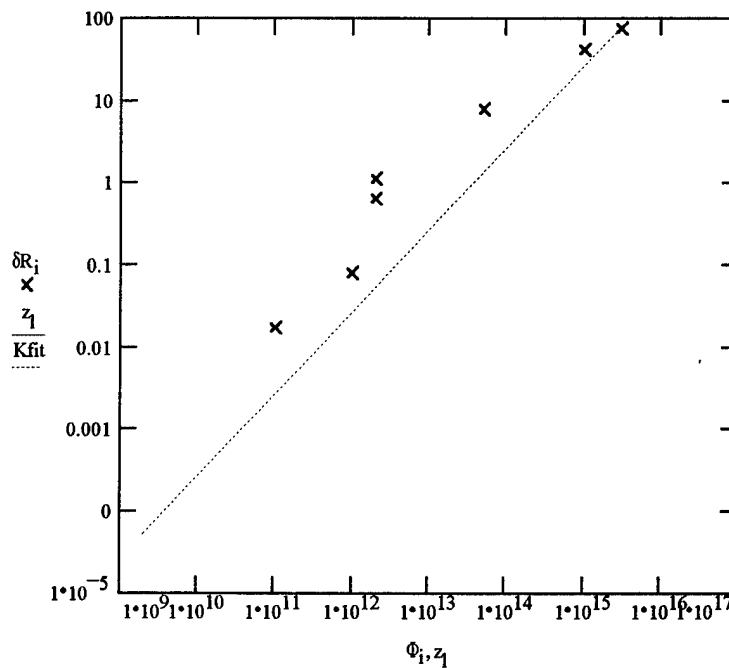
$$SSE(K_{fit}) = 172.5822608869$$

Creation of a continuous fluence for graphing

$$j := 0..4 \quad x_j := (j+1) \cdot 2 \cdot 10^9 \quad zzz := \text{stack}(x, 10 \cdot x) \quad zz := \text{stack}(zzz, 100 \cdot zzz) \quad z := \text{stack}(zz, 10000 \cdot zz)$$

$$l := 0.. \text{rows}(z) - 1$$

Log-Log graph  
for plotting the fit  
in finding K





Data file containing the average reflectance versus fluence

data := READPRN(test)

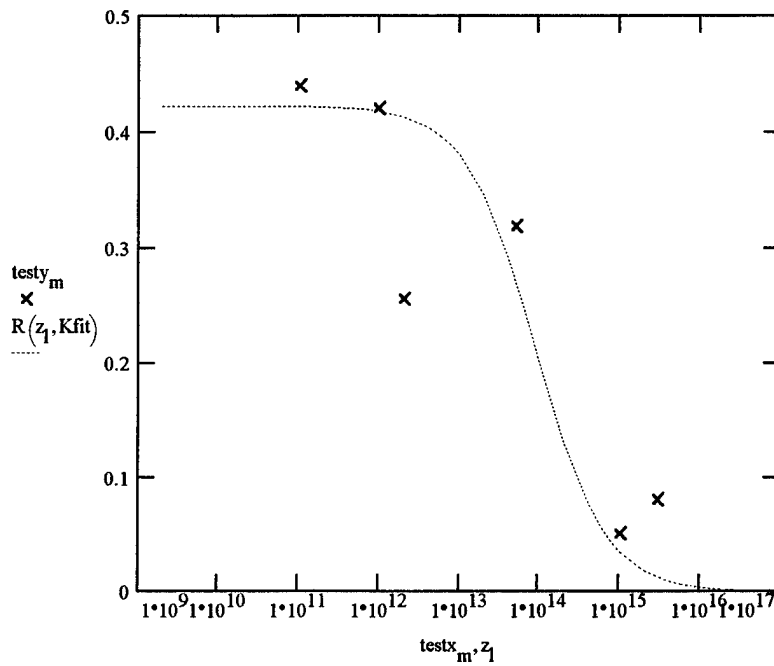
Verifies Messenger-Spratt form

data =  $\begin{bmatrix} 1.01 \cdot 10^{11} & 0.43891 \\ 1.01 \cdot 10^{12} & 0.420124 \\ 2.02 \cdot 10^{12} & 0.255014 \\ 5.06 \cdot 10^{13} & 0.316984 \\ 1.01 \cdot 10^{15} & 0.050494 \\ 3.03 \cdot 10^{15} & 0.079516 \end{bmatrix}$

m := 0..rows(data) - 1

testx<sub>m</sub> := data<sub>m,0</sub> Fluence data

testy<sub>m</sub> := data<sub>m,1</sub> Reflectivity data



II. The second part of this appendix is to include the changes that were done to Tom Fitzgerald's Mathcad model (AFIT MS Thesis, 1992). All of the changes that are included

A. Constant addition or step addition to the extinction coefficient.

A new function DeltaK was created to increase the extinction coefficient. The DeltaK will only be additive when the wavelength is below the threshold, which is the argument of DeltaK.

$$\text{DeltaK}(\lambda) := \text{if}(\lambda \geq 860, 0, 0.01)$$

Interpolated complex refractive index

$$n_{\text{AlGaAs}}(x, \lambda) := \text{real}\left(\frac{E(\lambda)}{\text{eV}}, x\right) - i \cdot \left| \text{imag}\left(\frac{E(\lambda)}{\text{eV}}, x\right) + \text{DeltaK}\left(\frac{\lambda}{\text{nm}}\right) \right|$$

To dump the reflectance data to a data file, the following command is implemented once the reflectivity is calculated.

$$\text{WRITEPRN}(\text{datafile}) := R_{\text{ct}, 1}$$

B. Constant factor multiplied by the extinction coefficient.

$$\text{MultiK} := \text{User\_Defined}$$

$$n_{\text{AlGaAs}}(x, \lambda) := \text{real}\left(\frac{E(\lambda)}{\text{eV}}, x\right) - i \cdot \left| \text{imag}\left(\frac{E(\lambda)}{\text{eV}}, x\right) \cdot \text{MultiK} \right|$$

MultiK can be any factor that you wish to apply over the wavelength range

## VITA

Captain Mark A. Suriano was born on 28 March, 1969 in Miami, FL. He graduated from Destrehan High School, Destrehan, LA in 1987. He received a Bachelors Degree in Nuclear Engineering from the Georgia Institute of Technology, Atlanta, GA in 1991 on a Reserve Officers Training Corps scholarship. After commissioning, he spent three months at Arkansas Nuclear One, Russellville, AR as a junior engineer working neutronicly coupled thermo-hydraulic codes. Upon activation to active duty, he was assigned to the Phillips Lab working in the Space Nuclear Power Branch. He was a project officer assigned to getting the TOPAZ-II Space Nuclear Power System up and running. He qualified as a shift supervisor on the only operational Space Nuclear Power System in the world. As part of the engineering team, he helped to create test plans designed to fully explore the Soviet design. After working with the TOPAZ-II for over a year, he was moved to head up the development of single thermal to electrical test article stands until being assigned to AFIT. Captain Suriano entered AFIT in May of 1995.

Permanent address: 1121 Beaverbrook Ln  
DeSoto, TX 75115

# REPORT DOCUMENTATION PAGE

Form Approved  
OMB No. 0704-0188

Public reporting burden for this collection of information is estimated to average 1 hour per response, including the time for reviewing instructions, searching existing data sources, gathering and maintaining the data needed, and completing and reviewing the collection of information. Send comments regarding this burden estimate or any other aspect of this collection of information, including suggestions for reducing this burden, to Washington Headquarters Services, Directorate for Information Operations and Reports, 1215 Jefferson Davis Highway, Suite 1204, Arlington, VA 22202-4302, and to the Office of Management and Budget, Paperwork Reduction Project (0704-0188), Washington, DC 20503.

1. AGENCY USE ONLY (Leave blank)	2. REPORT DATE December 1995	3. REPORT TYPE AND DATES COVERED Master's Thesis
----------------------------------	---------------------------------	---

4. TITLE AND SUBTITLE Neutron Damage in Distributed Bragg Reflectors and Microcavity Lasers	5. FUNDING NUMBERS
--	--------------------

6. AUTHOR(S) Mark A. Suriano Capt, USAF	
---	--

7. PERFORMING ORGANIZATION NAME(S) AND ADDRESS(ES) Air Force Institute of Technology 2750 P Street Wright-Patterson AFB, OH 45433-6583	8. PERFORMING ORGANIZATION REPORT NUMBER  AFIT/GAP/ENP/95D-15
---	---

9. SPONSORING/MONITORING AGENCY NAME(S) AND ADDRESS(ES) Capt Charles P. Brothers, Jr. PL/VTET 3550 Aberdeen Ave Kirtland AFB, NM 87116-5776	10. SPONSORING/MONITORING AGENCY REPORT NUMBER
---	--

11. SUPPLEMENTARY NOTES

12a. DISTRIBUTION/AVAILABILITY STATEMENT Approved for Public Release; Distribution Unlimited	12b. DISTRIBUTION CODE
---	------------------------

13. ABSTRACT (Maximum 200 words)  
Distributed Bragg Reflectors (DBRs) grown on a gallium-arsenide substrate for a solid state mirror and a vertical cavity surface emitting laser (VCSEL) were subjected to a neutron fluence to determine the sensitivity of the DBRs. The samples were irradiated at Ohio State University's 500 kW research reactor. Relative and absolute reflectance measurements were taken before and after each irradiation over a spectral band of 530-880 nm. Relative reflectance measurements showed that the irradiation did not cause any spectral shift over seven decades of neutron fluences. The reflectivity of the DBRs decreased from their initial measurements after being irradiated. The reflectance decrease was correlated to the incident neutron fluence to determine a Messenger-Spratt type of equation to predict the DBRs response. A radiation damage constant for the VCSEL and DBR mirror were determined to be  $3.83 \times 10^{13}$  [neutrons/cm<sup>2</sup>] and  $2.19 \times 10^{13}$  [neutrons/cm<sup>2</sup>] respectively utilizing a 1 MeV equivalent (Si) neutron fluence.

14. SUBJECT TERMS Radiation Damage; Radiation Effects; Neutron Radiation; Semiconductor Lasers; Reflectance; Laser Components; Bragg Scattering	15. NUMBER OF PAGES 106
	16. PRICE CODE

17. SECURITY CLASSIFICATION OF REPORT UNCLASSIFIED	18. SECURITY CLASSIFICATION OF THIS PAGE UNCLASSIFIED	19. SECURITY CLASSIFICATION OF ABSTRACT UNCLASSIFIED	20. LIMITATION OF ABSTRACT UL
---	--	---	----------------------------------

## GENERAL INSTRUCTIONS FOR COMPLETING SF 298

The Report Documentation Page (RDP) is used in announcing and cataloging reports. It is important that this information be consistent with the rest of the report, particularly the cover and title page. Instructions for filling in each block of the form follow. It is important to *stay within the lines* to meet *optical scanning requirements*.

### Block 1. Agency Use Only (Leave blank).

**Block 2. Report Date.** Full publication date including day, month, and year, if available (e.g. 1 Jan 88). Must cite at least the year.

**Block 3. Type of Report and Dates Covered.** State whether report is interim, final, etc. If applicable, enter inclusive report dates (e.g. 10 Jun 87 - 30 Jun 88).

**Block 4. Title and Subtitle.** A title is taken from the part of the report that provides the most meaningful and complete information. When a report is prepared in more than one volume, repeat the primary title, add volume number, and include subtitle for the specific volume. On classified documents enter the title classification in parentheses.

**Block 5. Funding Numbers.** To include contract and grant numbers; may include program element number(s), project number(s), task number(s), and work unit number(s). Use the following labels:

C - Contract	PR - Project
G - Grant	TA - Task
PE - Program Element	WU - Work Unit Accession No.

**Block 6. Author(s).** Name(s) of person(s) responsible for writing the report, performing the research, or credited with the content of the report. If editor or compiler, this should follow the name(s).

**Block 7. Performing Organization Name(s) and Address(es).** Self-explanatory.

**Block 8. Performing Organization Report Number.** Enter the unique alphanumeric report number(s) assigned by the organization performing the report.

**Block 9. Sponsoring/Monitoring Agency Name(s) and Address(es).** Self-explanatory.

**Block 10. Sponsoring/Monitoring Agency Report Number.** (If known)

**Block 11. Supplementary Notes.** Enter information not included elsewhere such as: Prepared in cooperation with...; Trans. of...; To be published in.... When a report is revised, include a statement whether the new report supersedes or supplements the older report.

**Block 12a. Distribution/Availability Statement.** Denotes public availability or limitations. Cite any availability to the public. Enter additional limitations or special markings in all capitals (e.g. NOFORN, REL, ITAR).

**DOD** - See DoDD 5230.24, "Distribution Statements on Technical Documents."

**DOE** - See authorities.

**NASA** - See Handbook NHB 2200.2.

**NTIS** - Leave blank.

**Block 12b. Distribution Code.**

**DOD** - Leave blank.

**DOE** - Enter DOE distribution categories from the Standard Distribution for Unclassified Scientific and Technical Reports.

**NASA** - Leave blank.

**NTIS** - Leave blank.

**Block 13. Abstract.** Include a brief (*Maximum 200 words*) factual summary of the most significant information contained in the report.

**Block 14. Subject Terms.** Keywords or phrases identifying major subjects in the report.

**Block 15. Number of Pages.** Enter the total number of pages.

**Block 16. Price Code.** Enter appropriate price code (*NTIS only*).

**Blocks 17. - 19. Security Classifications.** Self-explanatory. Enter U.S. Security Classification in accordance with U.S. Security Regulations (i.e., UNCLASSIFIED). If form contains classified information, stamp classification on the top and bottom of the page.

**Block 20. Limitation of Abstract.** This block must be completed to assign a limitation to the abstract. Enter either UL (unlimited) or SAR (same as report). An entry in this block is necessary if the abstract is to be limited. If blank, the abstract is assumed to be unlimited.